

# Numerical study of mild combustion : from laminar flames to Large Eddy Simulation of turbulent flames with Flamelet Generated Manifolds

**Citation for published version (APA):**

Abtahizadeh, S. E. (2014). *Numerical study of mild combustion : from laminar flames to Large Eddy Simulation of turbulent flames with Flamelet Generated Manifolds*. [Phd Thesis 1 (Research TU/e / Graduation TU/e), Mechanical Engineering]. Technische Universiteit Eindhoven. <https://doi.org/10.6100/IR766361>

**DOI:**

[10.6100/IR766361](https://doi.org/10.6100/IR766361)

**Document status and date:**

Published: 01/01/2014

**Document Version:**

Publisher's PDF, also known as Version of Record (includes final page, issue and volume numbers)

**Please check the document version of this publication:**

- A submitted manuscript is the version of the article upon submission and before peer-review. There can be important differences between the submitted version and the official published version of record. People interested in the research are advised to contact the author for the final version of the publication, or visit the DOI to the publisher's website.
- The final author version and the galley proof are versions of the publication after peer review.
- The final published version features the final layout of the paper including the volume, issue and page numbers.

[Link to publication](#)

**General rights**

Copyright and moral rights for the publications made accessible in the public portal are retained by the authors and/or other copyright owners and it is a condition of accessing publications that users recognise and abide by the legal requirements associated with these rights.

- Users may download and print one copy of any publication from the public portal for the purpose of private study or research.
- You may not further distribute the material or use it for any profit-making activity or commercial gain
- You may freely distribute the URL identifying the publication in the public portal.

If the publication is distributed under the terms of Article 25fa of the Dutch Copyright Act, indicated by the "Taverne" license above, please follow below link for the End User Agreement:

[www.tue.nl/taverne](http://www.tue.nl/taverne)

**Take down policy**

If you believe that this document breaches copyright please contact us at:

[openaccess@tue.nl](mailto:openaccess@tue.nl)

providing details and we will investigate your claim.

**Numerical study of Mild combustion  
from laminar flames to Large Eddy Simulation of turbulent flames  
with Flamelet Generated Manifolds**

PROEFSCHRIFT

ter verkrijging van de graad van doctor aan de  
Technische Universiteit Eindhoven, op gezag van de  
rector magnificus, prof.dr.ir. C.J. van Duijn, voor een  
commissie aangewezen door het College voor  
Promoties in het openbaar te verdedigen  
op maandag 27 januari 2014 om 16.00 uur

door

Seyed Ebrahim Abtahizadeh

geboren te Tabriz, Iran

Dit proefschrift is goedgekeurd door de promotoren en de samenstelling van de promotiecommissie is als volgt:

voorzitter: prof.dr.ir. M.G.D. Geers

promotor: prof.dr. L.P.H. de Goey

copromotor: dr.ir. J.A. van Oijen

leden: prof.dr. D.J.E.M. Roekaerts (Delft University of Technology)

prof.dr. A. Cavaliere (Università Federico II)

prof.dr.ir. J.A.M. Kuipers

prof.dr. H.B. Levinsky (Rijk Universiteit Groningen)

*To my wife*

Copyright © 2014 by S.E. Abtahizadeh

All rights reserved. No part of this publication may be reproduced, stored in a retrieval system, or transmitted, in any form, or by any means, electronic, mechanical, photocopying, recording, or otherwise, without the prior permission of the author.

This research is supported by the Dutch Technology Foundation STW, which is part of the Netherlands Organisation for Scientific Research (NWO) and partly funded by the Ministry of Economic Affairs (project number: 10414).



A catalogue record is available from the Eindhoven University of Technology Library

ISBN: 978-90-6464-738-3

Printed by GVO printers & designers B.V., Ede, the Netherlands

Cover design by Ferdinand van Nispen, [citroenvlinder-dtp.nl](http://citroenvlinder-dtp.nl), the Netherlands

# Contents

Summary	vii
<b>1 Introduction</b>	<b>1</b>
1.1 Background	1
1.2 Outline of thesis	7
<b>2 Computations of igniting counterflow diffusion flames</b>	<b>9</b>
2.1 Introduction	10
2.2 Numerical methodology and governing equations	11
2.3 Stationary flame structure	14
2.3.1 Influence of dilution ratio $\Theta$	14
2.3.2 Analysis of NO formation	18
2.4 Autoigniting flames	20
2.4.1 Effect of dilution ratio $\Theta$	21
2.4.2 Effect of strain rate $a$	22
2.5 Evaluation of chemical scheme and transport model	24
2.6 Discussions	24
2.7 Conclusions	26
<b>3 Detailed computations of coflow diffusion flames</b>	<b>29</b>
3.1 Introduction	30
3.2 Experimental setup	32
3.3 Mathematical model and numerical methodology	33
3.4 Domain and boundary conditions	35
3.5 Structure and stabilization mechanism of coflow flames	37
3.5.1 Radial profiles	38
3.5.2 General structure of flames	45
3.5.3 Analysis of flame structure in mixture fraction space	49
3.6 Analysis of NO formation	52
3.6.1 Rate-of-production analysis	52
3.6.2 Vertical profiles	53
3.6.3 Radial profiles	55
3.6.4 NO formation and consumption	59
3.7 Addition of Hydrogen	62

---

3.7.1	General structure of flames . . . . .	62
3.7.2	Radial and centerline profiles . . . . .	66
3.7.3	NO formation and consumption . . . . .	70
3.8	Conclusions . . . . .	72
<b>4</b>	<b>LES of turbulent lifted flames with hydrogen addition using FGM-PDF model</b>	<b>75</b>
4.1	Introduction . . . . .	76
4.2	Development of FGM to preferential diffusion and autoignition . . .	78
4.2.1	IML-flamelets . . . . .	78
4.2.2	Analysis of preferential diffusion effects . . . . .	80
4.2.3	Tabulation of IML-flamelets . . . . .	82
4.2.4	Derivation of transport equations for the controlling variables	84
4.2.5	Validation of the FGM model . . . . .	86
4.3	LES of the hydrogen enriched turbulent lifted flames . . . . .	89
4.3.1	LES formulation and numerical details . . . . .	89
4.3.2	Flow field statistics . . . . .	91
4.3.3	Influence of preferential diffusion on the lift-off height . . . .	92
4.3.4	Stabilization mechanism of lifted flames . . . . .	97
4.4	Conclusions . . . . .	98
<b>5</b>	<b>Conclusions and outlook</b>	<b>101</b>
5.1	Conclusions . . . . .	101
5.2	Discussions and future recommendations . . . . .	103
	<b>References</b>	<b>105</b>
	<b>Acknowledgements</b>	<b>113</b>
	<b>Curriculum Vitae</b>	<b>115</b>

# Summary

Combustion devices are often optimized in order to increase thermal efficiency and reduce pollutant emissions such as carbon monoxide (CO) and nitrogen oxides (NO<sub>x</sub>). In the recent decades, a new combustion technology has been introduced that deploys entrainment of burned gas into fuel and/or oxidizer stream(s) which is known as Mild combustion which usually yields a flameless oxidation. This entrainment process in Mild combustion is usually performed by recirculation of flue gas which couples an intense dilution with a substantial preheating of reactants. Due to such an intense dilution, a reduction in peak temperature levels is obtained which results in a significant decrease of NO<sub>x</sub> emissions and a homogeneous temperature field. Use of the recuperated heat in this process results in an increased thermal efficiency and an improved flame's stability. Although this combustion regime has been successfully applied in some industrial furnaces, its broad commercial application requires improved fundamental insight into its flame's structure and stabilization mechanism.

In chapter 2, flame structure and autoignition of Mild combustion is investigated for different cases in which burned gas is entrained into fuel and/or oxidizer stream(s). For this purpose, one-dimensional counterflow diffusion flames are studied because of their relatively simple configuration which allows us to perform a large number of computations using detailed chemical schemes with a reasonable computational cost. Steady-state computations reveal a number of attractive characteristics of Mild combustion for all cases, for instance, low peak temperatures and low NO<sub>x</sub> emissions. A kinetic study of NO formation indicates that the Fenimore mechanism is the dominant reaction pathway of NO formation. Transient solutions of the counterflow flames demonstrate a different autoignition time scale for each studied case and a strong dependence of autoignition to the amount of entrained burned gas and strain rate. At sufficiently high degree of preheating and dilution, the shortest ignition delay belongs to the case in which burned gas is entrained into both fuel and oxidizer streams. Ignition delay is decreased with increasing burned gas entrainment for all cases. Increasing strain rate delays autoignition for all cases.

In chapter 3, investigations are carried out to a more practical configuration, 2D axisymmetric laminar coflow diffusion flames. These flames permit detailed and accurate computations and experiments due to their relatively simple geometry, steadiness and optical accessibility. Several cases are studied in their transition from a "standard" condition to the Mild combustion regime with a systematic dilution and



preheating of the fuel and coflow streams. Computations are performed with detailed chemistry GRI-Mech 3.0, mixture-averaged transport model and taking into account radiative heat losses. Predictions reproduce experiments perfectly for temperature and major species which reveals that GRI-Mech 3.0 is capable to handle chemistry of Mild combustion. The effect of simplified transport models are studied by assuming constant Schmidt numbers which results in poor predictions on the centerline of coflow flames. Influence of radiative heat losses on the predictions appears to be increasingly important by increasing axial distance from the jet exit.

Analysis of the detailed computations indicates that the stabilization mechanism of “standard” laminar coflow flames occurs by an edge flame while a Mild flame stabilizes by autoignition. The stabilization of edge flame is governed by flame propagation yielding an attached flame to the burner exit. However, the autoigniting flame is stabilized at a certain axial distance from the burner exit. NO formation in the coflow flames is computed and validated with experiments using NO chemistry of GRI-Mech 3.0 mechanism with some modifications to include newly found NCN species. It appears that in Mild combustion, the Fenimore mechanism is the major kinetic route of NO formation. These observations correspond very well with the conclusions of chapter 2. Results show a reduction of the seeded NO at some axial distances of the Mild flame. It turns out that such a reduction is due to the conversion of the NO molecules to the N-containing intermediates. These intermediates are converted back to NO at downstream distances. Fuel flexibility of the Mild flame is investigated by addition of hydrogen to the fuel stream which is the main component of alternative fuels such as syn-gas. It appears that for the studied condition, addition of hydrogen appreciably decreases the flame’s lift-off height, however modestly affects peak temperature, NO formation and stabilization mechanism of the reaction zone.

In turbulent situations, predictions of flame’s lift-off height and stabilization mechanism of Mild combustion require complicated models that are able to predict ignition events. These predictions are particularly sensitive to variations in the fuel and oxidizer compositions and operating conditions. These variations affect the value of most reactive mixture fraction which mainly determines impact of turbulent structures on ignition events. Under intense dilution of reactants, especially oxidizer stream, most reactive mixture fraction shifts towards the oxidizer stream at regions of low scalar dissipation rates. At these locations, the influence of molecular diffusion on ignition events might become as important as turbulence transport. The conditions of low peak temperatures and oxygen concentrations lead to slower reaction rates and enhance the influence of molecular diffusion on the flame structure. The molecular diffusion becomes even more important by application of hydrogen containing fuels which introduces a considerable preferential diffusion.

In chapter 4, the main focus is on the development and application of a numerical model in order to predict turbulent lifted flames of  $\text{CH}_4/\text{H}_2$  mixtures in a hot and diluted environment. The Delft Jet-in-Hot coflow (DJHC) burner is chosen as a test case in which methane base fuel has been enriched with 0%, 5%, 10% and 25% of  $\text{H}_2$ . First, a novel combustion model is developed based on the Flamelet Generated Manifolds (FGM) technique to handle detailed chemistry in these computations. Such a development of the FGM methodology is inevitable since investigations with

detailed chemistry indicate that preferential diffusion strongly affects autoignition of these mixtures.

One-dimensional Igniting Mixing Layer flamelets (IML-flamelets) is proposed to accommodate preferential diffusion in a flamelet database. Solutions of these flamelets are tabulated using mixture fraction and reaction progress as controlling variables. Transport equations for these controlling variables are derived with additional terms to account for preferential diffusion effects. Comparison of predictions using this extended FGM model with those of detailed chemistry reveals that the model is able to predict autoignition time scales accurately for all considered cases. The importance of including preferential diffusion in various stages of the modeling is evaluated by comparing various simplified models. It is found that for accurate predictions, preferential diffusion effects have to be included in the computation of the flamelet table. At hydrogen levels above 5%, it is also necessary to include additional preferential diffusion terms in the transport equation for the progress variable.

Afterwards, a combined LES and FGM-PDF model is developed to simulate the turbulent lifted flames of  $\text{CH}_4/\text{H}_2$  mixtures. LES of these hydrogen enriched cases is conducted using the developed FGM models based on IML-flamelets. The main goal is to understand complex interactions of molecular diffusion and turbulence transport. The turbulence/chemistry interaction is modeled based on a gradient approximation for variances of controlling variables. These variances are computed using presumed  $\beta$ -PDF approximation which are stored in the flamelet database and retrieved during LES computations. Inflow turbulence is reproduced using a random noise generator to impose velocity fluctuations at the inflow. Predictions of the flow field are compared quantitatively with measurements which indicate a perfect agreement.

Computations of the reacting case are compared with the measured lift-off height of turbulent flames. It is revealed that the enrichment of fuel with hydrogen leads to a significant change in the lift-off height and stabilization mechanism of the turbulent lifted flames. Predictions of the 0% $\text{H}_2$  case indicate that inclusion of preferential diffusion in the combustion model modestly affects lift-off heights yielding a good agreement with measurements. However, for 5% $\text{H}_2$ , 10% $\text{H}_2$  and 25% $\text{H}_2$  cases, inclusion of preferential diffusion in the model affects strongly lift-off heights yielding much improved predictions compared to the unity Lewis number model. Main features of these turbulent lifted flames such as the formation of ignition kernels and stabilization mechanisms are thoroughly analyzed and compared with the measured instantaneous snapshots of OH chemiluminescence.



# Introduction

## 1.1 Background

Modern lifestyle requires a steady, available and reliable source of energy which lies at the heart of our mobility, our prosperity and our daily comfort. Energy resources that are available for us can be divided into three broad categories. The first is energy from fossil fuels that relies on energy from chemical bonds of a substance, usually a hydrocarbon. The second involves nuclear reactions that release energy either by splitting heavy nuclei or by fusing light nuclei. The third is thermo-mechanical in the form of wind, water, geological sources of steam and hot water. Although non-fossil energy resources sound more attractive than fossil fuels, they have some undesirable characteristics. Nuclear plants produce radioactive fission products. Hydrostatic plants require dams and barriers that may cause environmental damages. Solar energy and wind energy require large areas and are limited geographically. Geothermal sources are limited to very few locations. Schemes using small temperature gradients in the earth or oceans have low thermal efficiencies and hence require very large heat exchanger areas.

Fossil fuels currently supply most of the world's energy needs and they provide about two-thirds of the world's total electric power. Although supplies of fossil fuels are finite, currently there is no shortage of fossil fuels. World proven resources of oil is about  $1.6 \times 10^{14}$  liters [EIA, 2013] which might be increased significantly in the close future with discovery of new oil resources. There are also vast reserves of unconventional fossil fuels, such as tar sands, oil shale and gas hydrates. Considering world oil consumption approximately  $1.2 \times 10^{10}$  liters per day, fossil fuels will be a dominant energy source for the upcoming decades and will continue to be important in providing energy for the next generations. Figure 1.1 shows the world energy consumption from all type of fuels within the last decades and anticipation of its trend up to 2040 [EIA, 2013]. It is indicated that fossil fuels are expected to continue supplying much of the energy used worldwide. Although the fastest growth belongs to renewables and nuclear power, fossil fuels continue to have the highest share of total energy use for the upcoming decades.

Although fossil fuels provide a steady and reliable source of energy, mankind has to increasingly face its environmental related issues. From this prospective, the major goal of combustion researchers is to develop efficient and low pollutant combustion devices. Among different pollutants, nitrogen oxides could be ranked

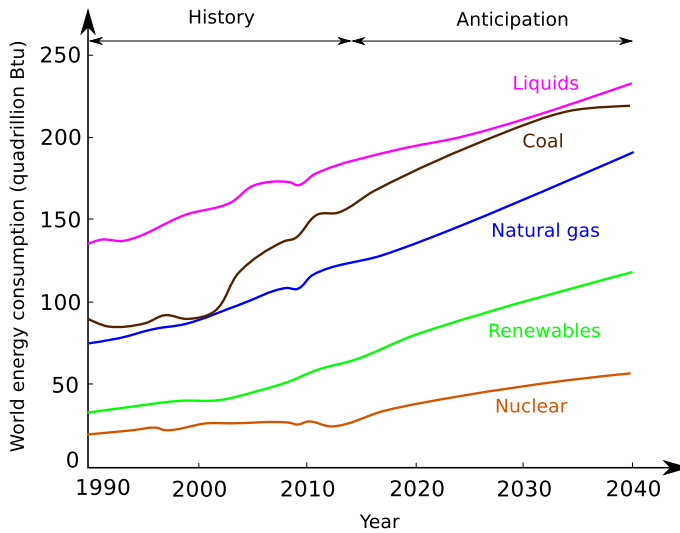


**Figure 1.1:** World energy consumption by fuel type, 1990-2040 (quadrillion Btu). Source: [EIA, 2013].

to the most common pollutants, which is emitted even with clean fuels such as natural gas or pure hydrogen. This pollutant is mainly produced through oxidation of nitrogen molecules of air at high temperatures, leading to severe consequences. Nitrogen oxides when dissolved in atmospheric moisture form nitric acids and a number of particles. These particles are such small that they can penetrate deeply into lung tissue and damage it, causing death in extreme cases. Nitrogen oxides also react with volatile organic compounds in the presence of sun light to form ozone which has adverse effects on lung tissue and lung function. Another harmful aspect of nitrogen oxides originates in its capability to destroy ozone at high altitudes leading to damage to life on earth through ultraviolet light.

Within last years, great effort has been performed to reduce nitrogen oxide, or more general  $\text{NO}_x$  emission, from combustion devices. This effort involves flame cooling, staging, lean premixed combustion, reburning, oxy-fuel combustion, exhaust gas recirculation and use of catalytic converters [Wünning and Wünning, 1997]. Among these approaches, exhaust gas recirculation has gained a lot of attention due to its relatively simple configuration and its capability to reduce  $\text{NO}_x$  and increase efficiency simultaneously. Such recirculation of exhaust gas is usually done externally or internally. At external recirculation, exhaust gas is taken from the stack of combustion device and is added to combustion air or the fuel stream. A blower or a jet pump is usually used to bring the exhaust gas to the required pressure. This configuration is suitable for the existing combustion devices as a low  $\text{NO}_x$  expansion. Internal exhaust gas recirculation is achieved by a special design of combustors that allow recirculation zones. By application of internal flue gas recirculation no additional equipment is required which has a positive influence on the efficiency.

Mild combustion or Flameless oxidation is based on recirculation of flue gas

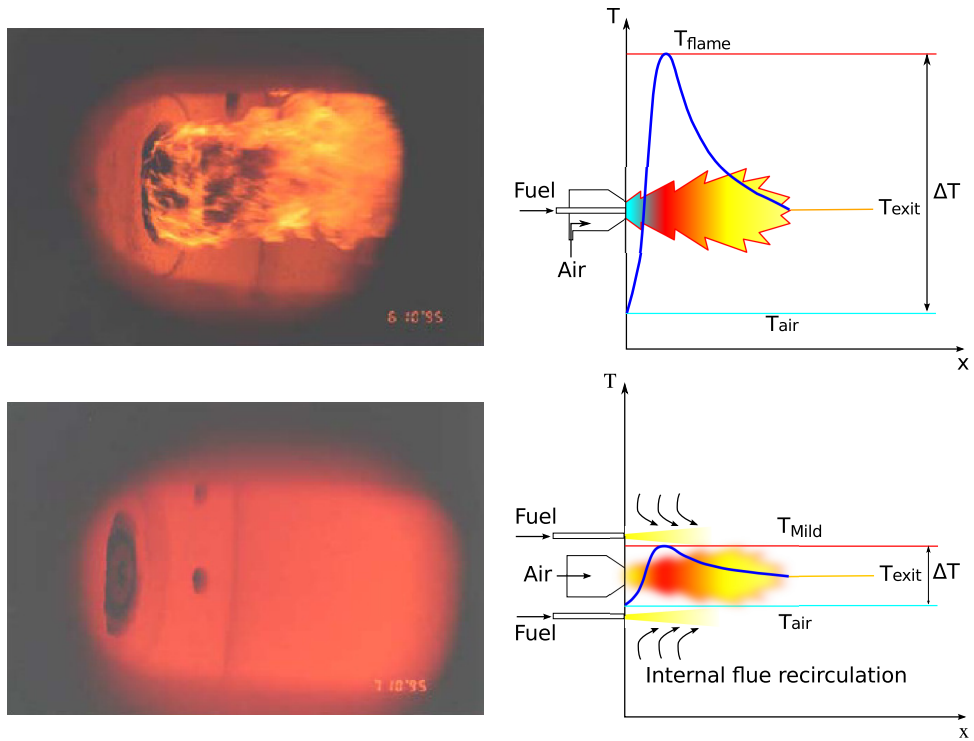


**Figure 1.2:** Comparison of (top figures) conventional combustion with (bottom figures) Mild combustion. Source: (left figures) IFRF (right figures) after [Wünning and Wünning \[1997\]](#).

(either internally or externally) which couples a high degree of preheating with a high degree of dilution of reactants [[Cavaliere and Joannon, 2004](#)]. Dilution causes a reduction in peak temperature levels which leads to a significant reduction of  $\text{NO}_x$  emissions and offer the possibility to obtain a homogeneous temperature field in furnaces. Due to the use of recuperated heat in this process, thermal efficiency of the system is increased and flame stabilization is improved considerably. These features make Mild combustion a unique process to decrease  $\text{NO}_x$  emissions and increase thermal efficiency simultaneously, since most other abatement techniques result in a reduced thermal efficiency.

Figure 1.2 shows some features of Mild combustion compared to conventional combustion. Mild combustion is mainly described as a mode in which reactants have intensely entrained into inert combustion products, so much that the peak reaction temperature is well below the adiabatic flame temperature. At these temperature levels, reaction rates become slower leading to a condition that a flame front cannot be stabilized. To prevent flame quenching, usually an intense preheating of reactants is performed by the entrainment of hot products. The preheating is conducted to raise temperature of reactants above the self-ignition temperature in order to stabi-

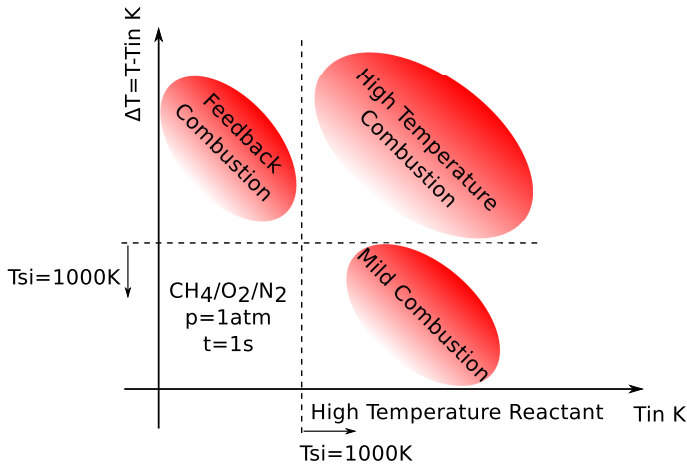


**Figure 1.3:** Comparison of different combustion modes in a  $T_{in} - \Delta T$  diagram. Source: [Cavaliere and Joannon, 2004].

lize the reaction zone by autoignition. Due to a small temperature increase from the high temperature reactants to the products, a more homogeneous temperature field is obtained which eventually leads to a substantial decrease of  $NO_x$  emissions. Recovery of waste heat during the recirculation process leads to an increased efficiency of the whole combustion process.

The description of Mild combustion is further clarified by comparison of different combustion modes in Fig. 1.3. In this diagram, a chemical system of  $CH_4/O_2/N_2$  mixture with 0.1/0.05/0.85 molar fractions is considered for a residence time of 1s at atmospheric pressure. The diagram is divided in three regions based on the self-ignition temperature ( $T_{si}$ ) of the  $CH_4/O_2/N_2$  mixture. Realization of Mild combustion, compared to the Feedback and High Temperature combustion, is quite straightforward. Mild Combustion cannot be sustained without preheating of reactants. In other words, in Mild combustion, as it will be shown in chapter 3, peak temperature levels are not high enough to stabilize the reaction zone by a propagating flame mechanism. However, Feedback and High Temperature Combustion, similar to traditional combustion processes, occur due to the sufficient heat release which can sustain the combustion process.

Between several methods of application of Mild combustion, two of them seem to be widely used which are schematically shown in Fig. 1.4. The first method is characterized by a central jet of fuel and a number of air jets located circumferentially around the central jet supplying combustion air. In this configuration, the air jets entrain large quantities of the recirculated combustion products before mixing with the fuel jet [Wünning and Wünning, 1997]. In the second method, the combustion air is provided by a central, high-momentum air jet which is surrounded by a number of low-momentum fuel jets. These weak fuel jets are injected into recirculated combustion products and consequently the fuel is diluted before it mixes with the combustion air [Weber et al., 1999; Tsuji et al., 2003].

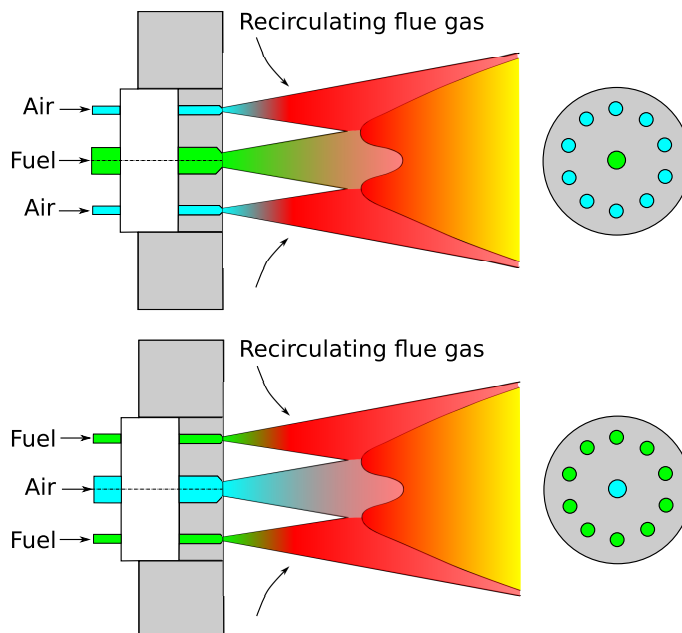


**Figure 1.4:** Schematic of a Mild combustion burner based on internal flue gas recirculation into the (top figure) air stream and (bottom figure) fuel stream.

Although these methods have been successfully applied in some industrial furnaces, the broad implementation is hampered by a lack of fundamental insight into this combustion regime. Regarding the different cases in which the burned gas is entrained into fuel and/or oxidizer stream(s), there are several issues that have to be fundamentally understood. For instance, the influence of preheating and dilution on peak temperatures and NO formation, effect of preheating and dilution on autoignition and the influence of inflow momentum and mixing on autoignition. 1D counterflow diffusion flames are a suitable configuration for such investigations. Their relatively simple configuration allows us to perform a large number of investigations with detailed numerical schemes at a reduced computational cost and avoid uncertainties related to flow and chemistry modeling.

Moving toward to a more practical side, it is necessary to understand local flame characteristics and stabilization mechanisms of Mild combustion in a multi-dimensional flame. Although Mild combustion occurs nearly always under turbulent conditions, laminar coflow diffusion flames make it possible to carry out accurate numerical and experimental research. This is due to their relatively simple geometry, steadiness and optical accessibility. Such accurate numerical information helps us to obtain a deep understanding of underlying processes in flame stabilization, reaction pathways of NO formation and the effect of using different fuels under Mild condition. In addition, it enables us to evaluate the performance of chemical schemes and numerical models for simulations of Mild combustion.



Numerical modeling of Mild combustion in turbulent situations requires sophisticated models which are able to adequately predict complex autoignition events at slow reaction rates. The slow reaction rates lead to a reduction in the characteristic Damköhler number. In this condition, unlike conventional diffusion flames which are primarily mixing-controlled, the reaction kinetics become important. This induces that molecular diffusion might become as important as turbulence transport in the stabilization of the reaction zone. The influence of molecular diffusion might become even more important by enrichment of fuel with  $H_2$  due to its preferential diffusion effects. The developed models for simulations of Mild burners have to carefully consider these effects. Experimental investigations in this field are mainly performed in the Jet-in-Hot Coflow (JHC) burners [Dally et al., 2002; Cabra et al., 2005; Arteaga et al., 2013] to mimic conditions of Mild combustion in turbulent situations. In these burners, a lifted reaction zone is mainly observed which is stabilized, in most cases, by autoignition.

The first step towards computations of these turbulent lifted flames is the development and validation of a simplified combustion model. The Flamelet Generated Manifolds (FGM) technique [van Oijen and de Goey, 2000] is one of the successful approaches in many applications which combines classical flamelet theory and the manifold methodology. In the manifold methods, such as Intrinsic Low Dimensional Manifolds (ILDM) [Maas and Pope, 1992], chemical processes that have a much smaller time scales than flow time scales are categorized as fast processes while others are called slow processes. It is believed that the fast chemical processes follow the rate-limiting slow processes. In a  $N_{sp}$ -dimensional composition space, with  $N_{sp}$  the number of species, rate-limiting processes form a lower dimensional subspace which is called “manifold”. Eventually, the full composition space can be described only by a few number of variables which controls all the processes. The ILDM method ignores convection and diffusion which results in weak predictions in low temperature regions where reaction rates are slow and chemical time scales become comparable to transport time scales. However, the FGM technique overcomes this issue by combining the manifold technique with the flamelet theory to include convection and diffusion processes yielding more accurate predictions at slow reaction rates. This is very important in Mild combustion because reaction rates are slow and flame stabilization might occur with significant ignition and extinction.

In the FGM technique, a database of thermo-chemical variables is created by conducting simulations of one-dimensional flames, so called “flamelets”, for a specific condition. These variables are stored in a database as a function of a few controlling variables which have to represent chemistry of a multidimensional flame adequately. During simulation of the multidimensional flame, usual fluid dynamics conservation equations are solved together with transport equations only for the controlling variables instead of all thermo-chemical variables. Quantities of the thermo-chemical variables are looked-up from the flamelet database using computed values for the controlling variables. This methodology leads to a significant reduction of computational cost while retaining information of the detailed chemistry.

The FGM technique has been successfully applied to premixed flames [van Oijen and de Goey, 2002], partially premixed flames [van Oijen and de Goey, 2004; Bongers, 2005] and non-premixed flames [Vreman et al., 2008]. Development of this

technique has been performed to incorporate unsteady effects (sinusoidally varying strain-rate) [Delhaye et al., 2009], Lewis number effects in premixed flames [de Swart et al., 2010] and autoignition with unity Lewis number transport [Bekdemir et al., 2013]. Extension of this technique to autoignition with non-unity Lewis number transport has not been performed yet. In this study, the FGM technique is extended to account for preferential diffusion effects during autoignition in order to simulate turbulent lifted flames with hydrogen containing fuels.

An important issue in these turbulent lifted flames of  $\text{CH}_4/\text{H}_2$  mixtures is flame stabilization. This issue is particularly important in practical implementations of Mild combustion where a robust understanding of the flame stabilization is required to design Mild burners with flexible fuels such as syn-gas. Although there are many Reynolds-Averaged Navier-Stokes (RANS) studies in this field [Coelho and Peters, 2001; Kim et al., 2005; Christo and Dally, 2005], the unsteady ignition events depend strongly on mixing in which Large Eddy Simulation (LES) is capable to provide more adequate results. In this study, LES of these turbulent lifted flame is conducted using the developed FGM methodology. Analysis of the computational results reveals a number of attractive features of these lifted flames which are discussed in detail.

## 1.2 Outline of thesis

In this thesis, the flame structure and stabilization mechanism of Mild combustion is investigated starting from a fundamental view (one-dimensional flames) and ending with a more practical view (three-dimensional flames). In chapter 2, flame structure and autoignition of Mild combustion is investigated considering different cases in which burned gas is entrained into fuel and/or oxidizer stream(s). For this purpose, a series of computations are conducted in the 1D counterflow diffusion flame configuration. Steady-state computations are carried out to reveal main characteristics of Mild combustion, for instance, low peak temperatures and low  $\text{NO}_x$  emissions. NO formation is analyzed to determine reaction pathways of NO formation. Transient computations are conducted to analyze autoignition of Mild combustion for each studied case and under different levels of burned gas entrainment and mixing.

In chapter 3, 2D axisymmetric laminar coflow diffusion flames are investigated in their transition from the “standard” condition to Mild combustion regime with a systematic preheating and dilution of fuel and coflow streams. Detailed computations of these flames are performed using detailed chemistry GRI-Mech 3.0, mixture-averaged transport model and inclusion of radiative heat losses. In the first stage, three cases is considered, namely Non-preheated flame (Case NP), Preheated flame (Case P) and Mild flame (Case M). Results are validated quantitatively with experiments for temperature and major species. Flame structure, stabilization mechanism and NO formation of these cases are analyzed and the distinction between the Mild flame and other flames is clarified. In the next stage, a new case is studied to investigate fuel flexibility of the Mild flame to hydrogen containing fuels. Computations of this case are validated with experiments and its structure and stabilization is analyzed and compared with the Mild flame.

In Chapter 4, the investigations are extended to turbulent lifted flames of

$\text{CH}_4/\text{H}_2$  mixtures in a hot and diluted environment. The Delft Jet-in-Hot coflow (DJHC) burner is chosen as a test case which is a laboratory scale burner to mimic conditions of Mild combustion. In this chapter, a novel numerical model is proposed to handle detailed chemistry in 3D computations of these flames. The model is developed based on the FGM technique which is extended to include preferential diffusion effects in autoigniting situations. In the next step, the developed FGM model is implemented in LES of the turbulent lifted flames. A range of hydrogen enriched cases is studied for 0%, 5%, 10% and 25% of  $\text{H}_2$  in the methane base fuel. Turbulent/chemistry interaction is modeled using a gradient model for the variances of controlling variables in conjunction with presumed  $\beta$ -PDF approximation. Inflow velocity fluctuations are reproduced using a random noise generator. Predictions of the mixing field and reaction zone are compared with measurements of velocity and OH chemiluminescence, respectively. Analysis of computational results is performed to reveal a number of interesting features of these lifted flames related to stabilization mechanism. The influence of hydrogen addition and preferential diffusion on the lift-off height and stabilization mechanism of these flames are clarified. Finally, main conclusions and summarizing remarks are presented in chapter 5.

# Computations of igniting counterflow diffusion flames

To achieve an efficient  $\text{NO}_x$  control in the application of Mild combustion in industrial furnaces, an intense dilution of reactants is generally required. In such a case, flame instabilities such as flame quenching may happen due to lower availability of oxidizer or fuel. Such instabilities are mainly avoided by addition of heat to reactants in order to provide sufficient enthalpy for autoignition. The dilution and preheating process is very often performed in industrial furnaces via internal recirculation of the burned gas. Such recirculation results in entrainment of burned gas into fuel and/or oxidizer stream(s).

In this chapter, a numerical study is performed to understand the influence of entrainment of burned gas into fuel and/or oxidizer stream(s) in Mild combustion. For this purpose, a numerical model is employed which consists of a network of plug flow reactors, a counterflow diffusion flame solver and an equilibrium solver for generation of the burned gas. Detailed chemistry and a multi-component transport model including Soret and Dufour effects are used for the computations. First, steady-state computations are performed to reveal main characteristics of Mild combustion regarding temperature levels and NO formation. Afterwards, transient behavior and autoignition of different cases are studied in which fuel and/or oxidizer are diluted and preheated with various amounts of burned gas. Dilution ratio and strain rate are adopted to vary chemical kinetic and mixing effects, respectively.

---

The content of this chapter has been extracted from the following paper:

S.E. Abtahizadeh, J.A. van Oijen, L.P.H. de Goey, *Numerical study of mild combustion with entrainment of burned gas into oxidizer and/or fuel streams*, Combustion and Flame 159 (2012) 2155-2165.

Minor adaptations have been performed to streamline the layout of the thesis.

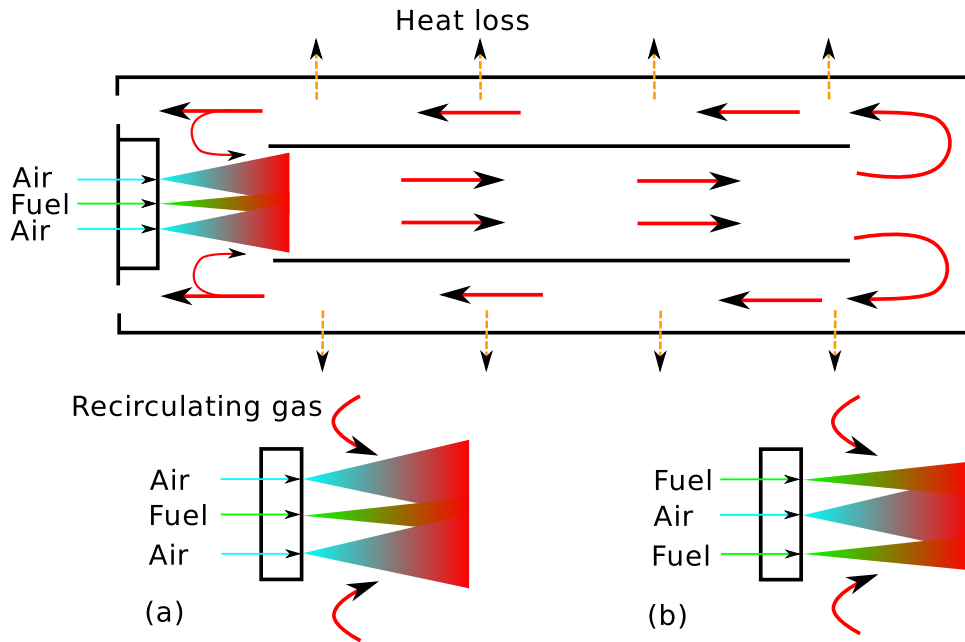


**Figure 2.1:** A schematic figure to represent application of Mild combustion in furnaces with recirculation of products. Entrainment of burned gas into the (a) air stream and (b) fuel stream.

## 2.1 Introduction

There are several methods for establishment of Mild combustion in industrial furnaces via internal recirculation of burned gas. These methods, which are schematically shown in Fig. 2.1, are based on entrainment of burned gas into fuel or oxidizer streams. Depending on the position of air and fuel injectors, different dilution cases can be investigated in which the burned gas might entrain into fuel, air or both streams. During this process, dilution and preheating are occurred simultaneously at various levels depending on the amount of entrained burned gas. Here, a numerical study is performed to understand the structure of reaction zone and autoignition of these cases.

In literature, there are several experimental studies about Mild combustion, mainly focused on the dilution and preheating of air stream. Earlier studies by [Wünning and Wünning \[1997\]](#) reported the main features of Mild combustion in a practical burner. It was shown that when combustion air is mixed with recirculated exhaust gas, thermal NO is suppressed. Moreover, no large gradients of temperature and species concentration were observed during the combustion process. Later studies are mainly concentrated on situations with a fuel jet issuing into a hot and diluted coflow stream. [Dally et al. \[2002\]](#) reported a Jet-in-Hot Coflow (JHC) burner which consists of an insulated and cooled central fuel jet inside an annulus with a

secondary burner. The secondary burner provides hot combustion products which are mixed with air using two side inlets upstream of the annulus exit, to control the oxygen level in the coflow. The cold mixture of air and nitrogen also assists in cooling of the secondary burner. Oldenhof et al. [2010] reported on the Delft Jet-in-Hot Coflow (DJHC) burner which is very similar to the burner of Dally. The main difference is that the latter uses addition of  $N_2$  to cool down the coflow whereas the DJHC burner uses cooling of the coflow through radiative and convective heat losses along the burner pipe.

Although numerical studies in this field are mainly focused on the air dilution case as well, a few studies have considered other cases. Dally et al. [2004] reported on the effect of mixing of the fuel stream with recirculated exhaust gas. It was shown that dilution of fuel with  $CO_2$  and  $N_2$  reduces  $NO_x$  emission. On the more fundamental side, Choi and Katsuki [2002] considered stationary laminar counterflow diffusion flames to compare different dilution cases. In a flamelet regime [Peters, 1984; van Oijen and de Goey, 2000], counterflow diffusion flames can be used to study local combustion characteristics of non-premixed flames. Choi and Katsuki [2002] showed that  $NO$  emission is decreased by an intense recirculation of flue gas into fuel or air stream. A clear view of autoignition of these cases is however not yet available, although it is essential for practical applications.

In this study, a numerical model is employed to study Mild combustion in a CounterFlow Diffusion Flame (CFDF) configuration where fuel and/or oxidizer stream(s) are preheated and diluted with various amounts of the burned gas. Steady-state and transient solutions of this numerical model are studied in order to answer several research questions in this field; For instance, the influence of preheating and dilution on peak temperatures and  $NO$  formation, effect of preheating and dilution on autoignition and the influence of inflow momentum and mixing on autoignition. These issues have to be fundamentally understood considering several cases in which the burned gas is entrained into fuel and/or oxidizer stream(s). In section 2.2, the numerical model is introduced and the theoretical background is explained. Solutions of the model for different dilution cases are presented in stationary and time-dependent situations in sections 2.3 and 2.4, respectively. In the section 2.4, the effect of dilution level and strain rate on autoignition is also discussed. Section 2.5 represents evaluation of the reaction mechanism and transport model which are used in the computations. In section 2.6, importance of ignition delay is discussed in the choice of a dilution case to design a practical Mild burner. Conclusions are summarized in section 2.7.

## 2.2 Numerical methodology and governing equations

The numerical model, used in this study, consists of a network of the CFDF solver, two Plug-Flow Reactors (PFRs) and an equilibrium solver as it is shown in Fig. 2.2. In this model, fuel and oxidizer streams are mixed with the burned gas forming a preheated and diluted mixture. The burned gas is computed as a chemical equilibrium of a stoichiometric fuel and oxidizer mixture at a constant temperature below the adiabatic flame temperature. This heat loss effect is considered to account for

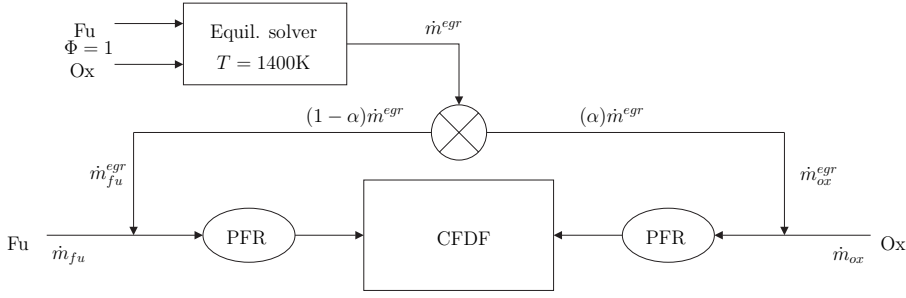


**Figure 2.2:** The numerical model that consists of a combination of plug flow reactors (PFRs), a counterflow diffusion flame (CFDF) solver, an equilibrium solver for generation of the burned gas and heat loss effects.

convective and radiative losses from the reaction zone in a practical Mild combustor. Due to such effects, the burned gas is assumed to be cooled down to 1400K.

The presence of small amounts of radicals in the burned gas cause chemical decomposition of species immediately after mixing of the reactants and the burned gas. To alleviate such decomposition at the inlet of the CFDF solver, PFRs are used to give a short residence time (less than 0.01 s) to the mixture of reactants and burned gas. After such a short residence time, composition of the mixture does not change significantly and it is used as a boundary condition for the CFDF solver. Without PFRs, the mixture reacts immediately at the inflow boundary, resulting in unwanted gradients and fluxes which cannot be avoided by moving the boundary further away from the flame. Furthermore, NO-reburn occurs at the boundary for nitrogen-containing species of the burned gas. Since a particular interest of this research is to study thermal and prompt NO formation rather than NO-reburning, the nitrogen-containing species (except  $N_2$ ) are neglected from the composition of the burned gas.

The dilution ratio  $\Theta$  is defined as the ratio of mass flow rate of the burned gas to that of the total of the reactants entering the CFDF:

$$\Theta = \frac{\dot{m}^{egr}}{\dot{m}_{ox} + \dot{m}_{fu} + \dot{m}^{egr}} \quad (2.1)$$

In the model, the mass flow rate of the burned gas  $\dot{m}^{egr}$  is split into:

$$\dot{m}_{fu}^{egr} = (1 - \alpha)\dot{m}_{egr} \quad (2.2)$$

$$\dot{m}_{ox}^{egr} = \alpha\dot{m}_{egr} \quad (2.3)$$

in which  $\dot{m}_{fu}^{egr}$  and  $\dot{m}_{ox}^{egr}$  refer to the mass flow rate of the burned gas entrained into the fuel and the oxidizer stream, respectively.

In this study, three cases are considered in which fuel and/or oxidizer stream(s) are preheated and diluted with burned gas of stoichiometric methane and air:

1. Dilution of the oxidizer stream (Case O,  $\alpha = 1$ )

2. Dilution of both streams (Case B,  $\alpha = 0.5$ )
3. Dilution of the fuel stream (Case F,  $\alpha = 0$ )

The one-dimensional counterflow diffusion flame (CFDF) in a planar stagnation flow is described by the following set of transport equations:

$$\frac{\partial \rho}{\partial t} + \frac{\partial \rho u}{\partial x} = -\rho G \quad (2.4)$$

$$\frac{\partial(\rho Y_i)}{\partial t} + \frac{\partial(\rho u Y_i)}{\partial x} - \frac{\partial}{\partial x}(\rho V_i Y_i) - \dot{\omega}_i = -\rho G Y_i \quad (2.5)$$

$$\frac{\partial(\rho h)}{\partial t} + \frac{\partial(\rho u h)}{\partial x} - \frac{\partial}{\partial x} \left( \frac{\lambda}{c_p} \frac{\partial h}{\partial x} \right) = \frac{\partial}{\partial x} \left( \sum_{i=1}^{N_{sp}} h_i \left( \rho V_i Y_i - \frac{\lambda}{c_p} \frac{\partial Y_i}{\partial x} \right) \right) - \rho G h \quad (2.6)$$

where  $\rho$ ,  $\lambda$  and  $c_p$  denote mixture density, thermal conductivity and specific heat at constant pressure, respectively.  $V_i$ ,  $\mu$  and  $t$  refer to diffusion velocity, dynamic viscosity and time, respectively.  $Y_i$ ,  $\dot{\omega}_i$  and  $N_{sp}$  are mass fraction of the  $i$ -th species, chemical production rate and total number of species present in the used chemical scheme, respectively. To obtain the stretch rate ( $G$ ), an additional transport equation has to be solved:

$$\frac{\partial(\rho G)}{\partial t} + \frac{\partial(\rho u G)}{\partial x} - \frac{\partial}{\partial x} \left( \mu \frac{\partial G}{\partial x} \right) = J - 2\rho G^2, \quad J = \rho_{ox} a^2 \quad (2.7)$$

where  $\rho_{ox}$  and  $a$  denote to density and applied strain rate at the oxidizer side, respectively. This transport equation has been derived from the momentum equation in  $y$ -direction by [Dixon-Lewis \[1968\]](#). The boundary conditions for a strained counterflow diffusion flame are:

$$\begin{aligned} Y_i(x \rightarrow -\infty) &= Y_{i,1}, & h(x \rightarrow -\infty) &= h_1, & G(x \rightarrow +\infty) &= a, \\ Y_i(x \rightarrow +\infty) &= Y_{i,2}, & h(x \rightarrow +\infty) &= h_2, & \frac{\partial G}{\partial x}(x \rightarrow -\infty) &= 0 \end{aligned} \quad (2.8)$$

the subscripts 1 and 2 refer to the composition in, respectively, the fuel and oxidizer stream. The initial conditions correspond to frozen mixing of oxidizer and fuel stream, that is, the steady solution of Eqs. (2.4-2.7) with  $\dot{\omega} = 0$ . The set of Eqs. (2.4-2.7) with the provided boundary and initial conditions is solved by the one-dimensional reacting flow solver CHEM1D [[Somers, 1994](#)] developed at the Eindhoven University of Technology.

In this study, methane is considered as a base fuel and air as a base oxidizer, both at ambient temperature (300K). The mixture fraction  $\zeta$  is used as a parameter to quantify mixing of the streams following the definition of [Bilger \[1988\]](#):

$$\zeta = \frac{\frac{1}{2} M_H^{-1} [z_H - z_{H,2}] + 2 M_C^{-1} [z_C - z_{C,2}] - M_O^{-1} [z_O - z_{O,2}]}{\frac{1}{2} M_H^{-1} [z_{H,1} - z_{H,2}] + 2 M_C^{-1} [z_{C,1} - z_{C,2}] - M_O^{-1} [z_{O,1} - z_{O,2}]} \quad (2.9)$$

where  $z_H$ ,  $z_C$ , and  $z_O$  are the elemental mass fractions of hydrogen, carbon and oxygen respectively.  $M_H$ ,  $M_C$ , and  $M_O$  are the corresponding atomic masses. The



mixture fraction according to this definition is a passive scalar normalized between  $\zeta = 0$  and  $\zeta = 1$  in the possibly diluted fuel and oxidizer at the CFDF inlet, respectively. GRI-Mech 3.0 [Smith et al., 2000] is used to compute the formation and destruction rates of chemical species and to obtain the required thermodynamic and transport data involved in methane-air combustion. In this study, results of this chemical scheme have been compared with results obtained by GRI-Mech 2.11 [Bowman et al., 1995] and the reaction mechanism by Konnov and Dyakov [2009].

Autoignition of Mild combustion based on the intense mixing of reactants leads to slower reaction rates in which molecular diffusion plays an important role in the flame structure. Furthermore, the availability of some diffusive species such as H and H<sub>2</sub> in the composition of the burned gas can make the diffusion model even more important. In this study, a multicomponent transport model including Soret and Dufour effects is used. In the following section, performance of more simplified transport models such as mixture-averaged, constant Lewis number and unity Lewis number assumption are evaluated as well.

Following sections present numerical results, first for the stationary behavior of the model and afterwards, for autoignition. In section 2.3 different dilution cases having the same dilution ratio are compared. Autoignition of various dilution cases is discussed in section 2.4. This section also comprises the influence of dilution ratio and strain rate on autoignition. Finally, in section 2.5, the effect of using different reaction mechanisms and transport models is investigated.

## 2.3 Stationary flame structure

### 2.3.1 Influence of dilution ratio $\Theta$

In this subsection, investigations are performed to study influence of dilution ratio on flame structure of the counterflow diffusion flames. As an example, values at boundaries of the counterflow flame is shown in Table 2.1 which is obtained from mixing of burned gas and reactants with  $\Theta = 0.9$  after passing through PFRs. It is indicated that the dilution ratio  $\Theta$  has a considerable influence on boundary conditions of the CFDF. For example, a very small amount of O<sub>2</sub> at the oxidizer side of Case O and CH<sub>4</sub> at the fuel side of Case F is remained as a result of application of  $\Theta = 0.9$ . Such a change in compositions leads to various flame temperatures and NO formations for different dilution cases as shown in Fig. 2.3. In spatial domain ( $x$ ), temperature rise and its peak value decrease with increasing dilution ratio for cases with diluted fuel as well as diluted oxidizer. In mixture fraction space ( $\zeta$ ), the same trend can be observed. Peak values of temperature profiles are located at different mixture fractions for various dilution ratios. These mixture fractions are closer to the oxidizer side in Case O ( $\alpha = 1$ ) and closer to the fuel side in Case B ( $\alpha = 0.5$ ) and F ( $\alpha = 0$ ) and their value are approximately equal to the stoichiometric value. Between the different dilution cases, Case B shows a more uniform distribution of temperature than the other cases. This is caused by elevated temperatures of reactants at both sides as a result of preheating of both streams. This characteristic of Case B causes a specific behavior of its autoignition, which is

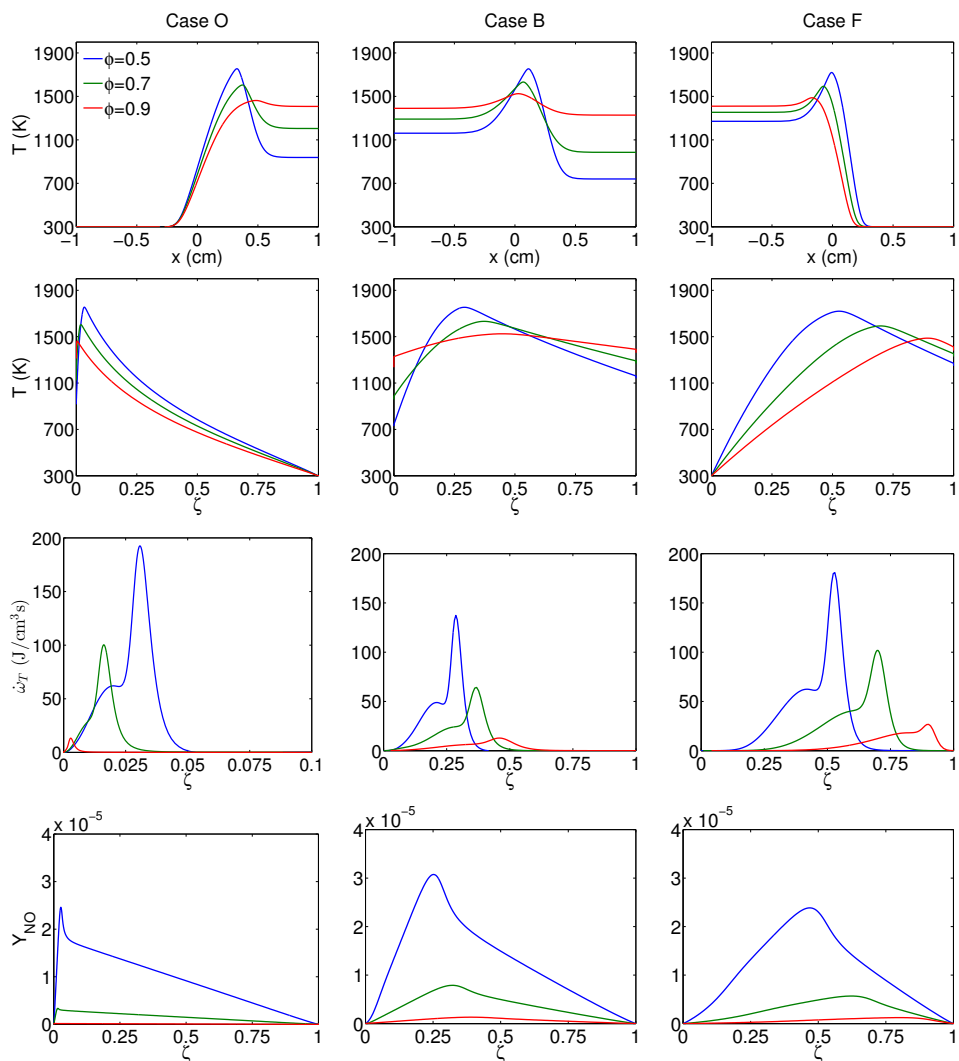


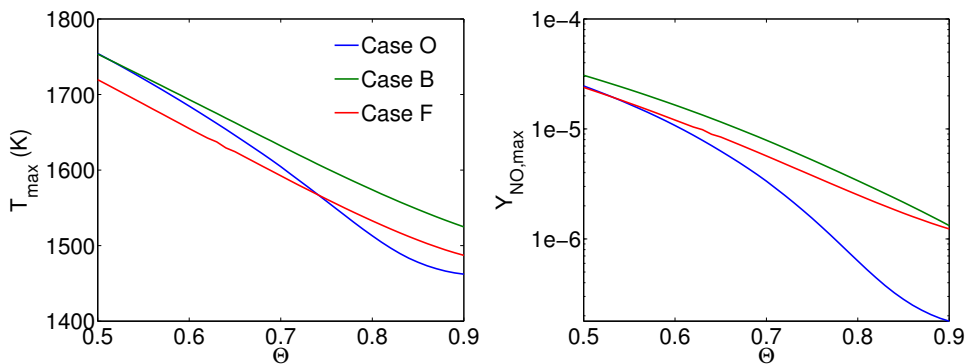
**Figure 2.3:** Profiles of temperature, heat release and mass fraction of NO for various dilution ratios  $\Theta$  and dilution cases O, B and F at a strain rate of  $a = 75 \text{ s}^{-1}$ . Stoichiometric mixture fractions at  $\Theta = 0.9$  are (Case O)  $\zeta_{st} = 0.0056$ , (Case B)  $\zeta_{st} = 0.4455$  and (Case F)  $\zeta_{st} = 0.9017$ .

discussed in the following section.

Heat release  $\dot{\omega}_T$  profiles show the correspondence of the mixture fraction where the maximum heat release occurs to that of the maximum temperature. Both occur approximately at stoichiometric mixture fractions. Joannon et al. [2009, 2007] observed similar profiles in the Mild regime. In their study, they show that in Mild regime, the pyrolytic region, characterized by a negative heat release, does not occur

**Table 2.1:** Temperature and mole fraction of major species at the oxidizer and fuel boundary of the CFDF for dilution cases O, B and F,  $\Theta=0.9$ .

	Case O <sub>ox</sub>	Case O <sub>fe</sub>	Case B <sub>ox</sub>	Case B <sub>fe</sub>	Case F <sub>ox</sub>	Case F <sub>fe</sub>
T	1415	300	1337	1396	300	1413
$X_{O_2}$	$1.953 \times 10^{-2}$	0	$3.602 \times 10^{-2}$	$4.534 \times 10^{-3}$	0.210	$4.5648 \times 10^{-3}$
$X_{N_2}$	0.7212	0	0.7272	0.6935	0.790	0.70137
$X_{H_2O}$	0.1731	0	$1.583 \times 10^{-2}$	0.1834	0	0.18513
$X_{CH_4}$	0	1	0	$1.694 \times 10^{-2}$	0	$7.4197 \times 10^{-3}$
$X_{OH}$	$1.742 \times 10^{-4}$	0	$1.170 \times 10^{-4}$	$5.576 \times 10^{-7}$	0	$1.4881 \times 10^{-6}$
$X_{H_2}$	$4.182 \times 10^{-5}$	0	$1.743 \times 10^{-5}$	$6.136 \times 10^{-3}$	0	$5.6724 \times 10^{-3}$
$X_{CH_2O}$	0	0	0	$6.006 \times 10^{-5}$	0	$4.8756 \times 10^{-5}$

**Figure 2.4:** Peak values of (left) temperature and (right) NO mass fraction against dilution ratio  $\Theta$  for dilution cases O, B and F,  $a=75 \text{ s}^{-1}$ .

and the heat release profiles have one major peak. Their observation corresponds very well the heat release profiles in Fig. 2.3. NO formation follows the trend of the temperature considering that for sufficiently low temperature levels ( $< 1600\text{K}$ ) NO formation approaches zero. This happens because of a negligible formation of thermal and prompt NO at these temperature levels.

Figure 2.4 shows how peak values of temperature  $T_{max}$  and NO mass fraction decrease with increasing dilution ratio for each dilution case. It is indicated that at a certain dilution ratio  $\Theta$ , the maximum temperature is slightly different for each dilution case. Since dilution cases are preheated and diluted with the same amount of burned gas for a particular dilution ratio, equilibrium temperature should be the same. To find out how these differences arise, initial values of species mass fraction and enthalpy in the frozen mixing state at the stoichiometric mixture fraction  $\zeta_{st}$  are computed as follows:

$$Y_{i,st} = \zeta_{st} Y_{i,1} + (1 - \zeta_{st}) Y_{i,2} \quad (2.10)$$

$$h_{i,st} = \zeta_{st} h_{i,1} + (1 - \zeta_{st}) h_{i,2} \quad (2.11)$$

At the stoichiometric mixture fraction, equilibrium temperatures are then calculated for the different dilution cases (see Table 2.2). The equilibrium temperatures are

**Table 2.2:** Comparison of peak temperatures between dilution cases O, B and F.  $a=75 \text{ s}^{-1}$ ,  $J = 2.10(\text{gr}/\text{cm}^3\text{s}^2)$ ,  $\Theta=0.5$ .

	Peak temperatures (K)		
	$a = \text{const.}$	$J = \text{const.}$	Equilibrium
Case O	1754.3	1754.3	1915.3
Case B	1753.5	1758.6	1915.3
Case F	1719.5	1753.2	1915.3
Maximum difference	34.8	5.4	0

exactly the same for the different dilution cases. This means that the net enthalpy content of different dilution cases at the stoichiometric mixture fraction is the same. The peak temperatures are lower than the equilibrium temperature because of conductive heat loss which is proportional to the scalar dissipation rate  $\chi$ . The scalar dissipation rate is a key quantity in the description of diffusion flames [Peters, 2000]:

$$\chi = 2 \frac{\lambda}{\rho c_p} \left( \frac{\partial \zeta}{\partial x} \right)^2 \quad (2.12)$$

The value of  $\chi$  at the stoichiometric plane is approximately proportional to the applied strain rate and the square root of the density of the oxidizer side:

$$\chi_{st} \propto a \sqrt{\rho_{ox}} = \sqrt{J} \quad (2.13)$$

Based on Eq. (2.13), the differences between peak temperatures of different dilution cases may be related to the applied strain rate which is kept constant for various dilution cases. Different oxidizer temperatures of different dilution cases result in a different  $J$  leading to a change in scalar dissipation rate and hence a change in heat loss.  $J$  can be kept constant by adjusting the strain rate to account for the density changes at the oxidizer side. With this approach, the difference between peak temperatures becomes significantly smaller as shown in Table 2.2. The small remaining difference can be related to the influence of diffusion on the distribution of temperature and mass fraction of species in the domain.

Figure 2.4 also shows that Case F has the lowest peak temperature of the three cases until  $\Theta = 0.75$ . This happens because Case F has the lowest oxidizer temperature and consequently the lowest  $J$  for a certain  $\Theta$ . However at higher  $\Theta$ 's, Case O has the lowest peak temperature. This is caused by the movement of the peak temperature location to the oxidizer side with increasing  $\Theta$ , eventually leading to an intense conductive heat loss to the colder oxidizer stream ( $\zeta = 0$ ). Among the dilution cases, Case B has the highest peak temperature and NO formation for the whole range of  $\Theta$ . This happens due to the low conductive heat loss to the reactant streams ( $\zeta=0,1$ ) as a result of the elevated temperature of both streams. In the next section, NO formation of this case is investigated in detail to study various kinetic routes of NO formations.

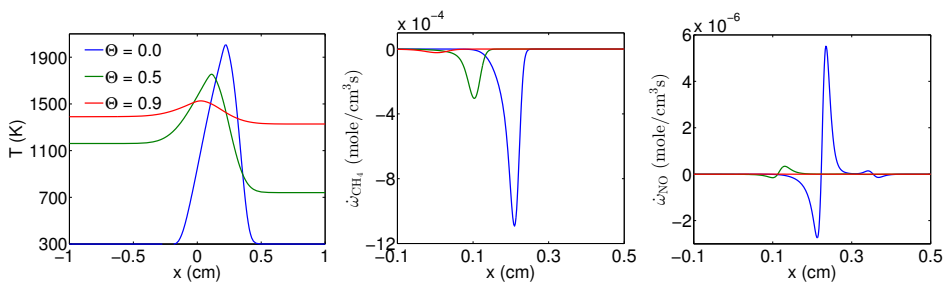


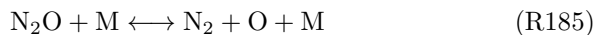
**Figure 2.5:** Temperature and chemical source terms of  $\text{CH}_4$  and  $\text{NO}$  for different dilution ratios, Case B,  $a = 75 \text{ s}^{-1}$ .

### 2.3.2 Analysis of NO formation

To examine the effect of dilution and preheating on the  $\text{NO}$  formation in detail, temperature and chemical source terms of  $\text{CH}_4$  and  $\text{NO}$  are shown in Fig. 2.5 for a range of  $\Theta$ . At lower  $\Theta$ s where there is a high concentration of  $\text{CH}_4$  and  $\text{O}_2$  in the reactants, temperature reach to high values as a result of high chemical enthalpy content of the reactants. Consequently, the rate of production and consumption of  $\text{CH}_4$  and  $\text{NO}$  is high at these temperature levels according to the Arrhenius law. It is worth to consider that at low dilution ratios the required residence time to ignite the mixture increases tremendously which eventually increases autoignition time. This point is discussed in detail in the next section. Although very low values of  $\Theta$  cannot be called Mild because of the very high autoignition times (and also because of the higher peak temperature values), it is studied here to have a better understanding of the  $\text{NO}$  formation processes. It is believed that decreasing flame temperature reduces the  $\text{NO}$  formation mainly because of suppressing the thermal  $\text{NO}$  formation. The formation of thermal  $\text{NO}$  is determined by a set of highly temperature dependent chemical reactions following Zeldovich mechanism:



These reactions and their numbering follow the GRI-Mech 3.0 mechanism. The  $\text{N}_2\text{O}$  mechanism becomes important in fuel lean and low temperature conditions.  $\text{N}_2\text{O}$  is mainly formed by (R185) and is converted to  $\text{NO}$  by reactions (R182) and (R199):



The Fenimore mechanism (prompt  $\text{NO}$ ) in hydrocarbon flames is initiated by the rapid reaction of hydrocarbon radicals with molecular nitrogen:



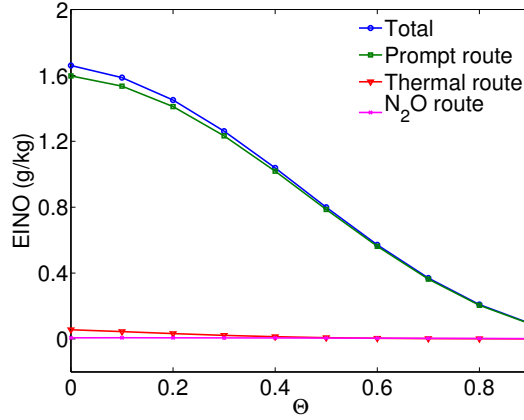


**Figure 2.6:** Emission index obtained from various kinetic routes of NO formation as a function of dilution ratio, Case B,  $a = 75 \text{ s}^{-1}$ .

For a quantitative comparison of different NO formation route at different dilution ratios, the emission index of NO (EINO) is defined as the amount of pollutants produced per unit of mass of fuel consumed by the combustion process:

$$\text{EINO}(\text{g/kg}) = \frac{W_{\text{NO}} * \int_V \dot{\omega}_{\text{NO}} dV}{-W_{\text{CH}_4} * \int_V \dot{\omega}_{\text{CH}_4} dV} * 10^3 \quad (2.14)$$

where  $W_{\text{NO}}$  and  $W_{\text{CH}_4}$  denote the molecular weights of NO and  $\text{CH}_4$  while  $\dot{\omega}_{\text{NO}}$  and  $\dot{\omega}_{\text{CH}_4}$  are the molar source terms of NO and  $\text{CH}_4$ , respectively. The contributions of the thermal, prompt and  $\text{N}_2\text{O}$  routes to the total NO formation for various  $\Theta$  are shown in Fig. 2.6. These contributions are computed based on simulations using each of these routes while setting reaction rate of other routes to zero. It is interesting to note that the prompt route has the major contribution to the total NO formation at different dilution ratios. Thermal NO increases with decreasing dilution ratios as a result of increased peak temperatures. However, the quantity of thermal NO is not considerable in the total amount because of a short residence time between the intermediates in the reaction zone at a strain rate of  $75 \text{ s}^{-1}$ . The thermal NO is produced mainly by  $\text{N} + \text{NO} \leftrightarrow \text{N}_2 + \text{O}$  (R178) while the prompt NO is mainly formed by the production of HCN through the reaction  $\text{CH} + \text{N}_2 \leftrightarrow \text{HCN} + \text{N}$  (R240). The reaction rates of (R178) and (R240) are shown in Fig. 2.7 for different dilution ratios. It can be observed that the rates of these reactions drop significantly with increasing dilution ratio. Another interesting point is the ratio between the reaction rates of these reactions for each dilution ratio. The rate of (R240), which at low  $\Theta$  is almost 10 times bigger than (R178), becomes more than 200 times bigger at high dilution ratio. This confirms the dominant role of prompt NO formation in the total NO formation.

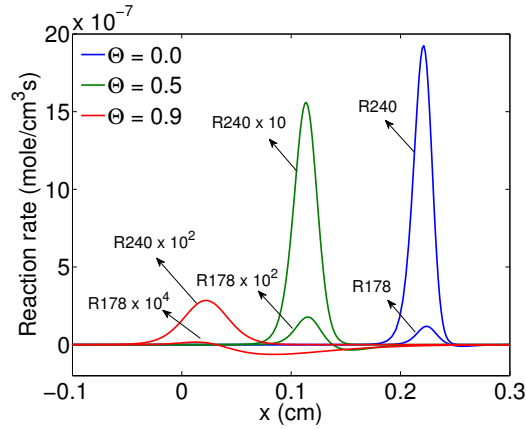


**Figure 2.7:** Reaction rates of (R178) and (R240) for different dilution ratios, Case B,  $a = 75 \text{ s}^{-1}$ .

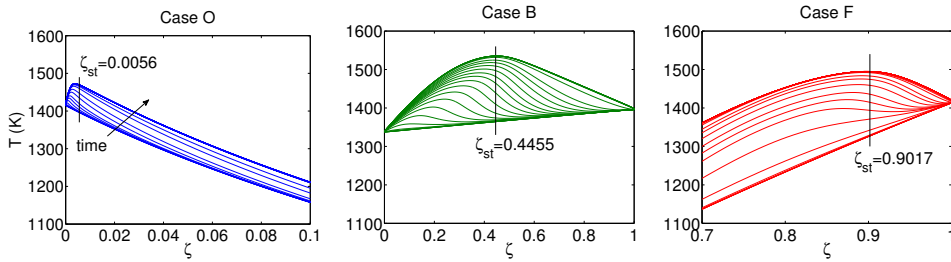


**Figure 2.8:** Evolution of temperature in mixture fraction space for dilution cases O, B and F,  $\Theta=0.9$ ,  $a = 75 \text{ s}^{-1}$ .

## 2.4 Autoigniting flames

In the previous section, attention is given only to the steady-state situations in order to evaluate dilution cases based on temperature levels and NO emission. However, Mild combustion also requires a fundamental knowledge on the transition to this state. Autoignition deals with the transition from a slowly reacting state to a fully burning state in a combustion process [Glassman, 1987]. In order to obtain a better understanding of the autoignition process, a simplified form of Eqs. (2.4-2.6) with unity Lewis number assumption can be written as [Peters, 2000]:

$$\rho \frac{\partial T}{\partial t} = \dot{\omega}_T + \frac{1}{2} \rho \chi \frac{\partial^2 T}{\partial \zeta^2} \quad (2.15)$$

This equation shows that the evolution of temperature can be decomposed into a reaction part, the 1st term in the RHS and a mixing part, the 2nd term in the RHS. In the mixing part, the scalar dissipation rate  $\chi$  determines the mixing rate and consequently diffusion effects.

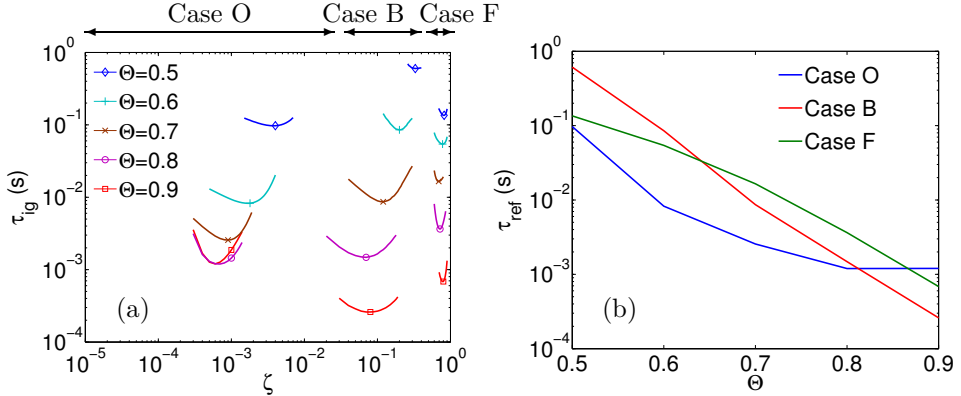


**Figure 2.9:** Comparison of dilution cases O, B and F according to (a)  $\tau_{ign}$  against mixture fraction  $\zeta$  and (b)  $\tau_{ref}$  against dilution ratio  $\Theta$ .

Figure 2.8 shows the evolution of temperature in mixture fraction space for all dilution cases. A comparison between the results shows that the temperature rise starts at a different mixture fraction for each dilution case. This rise starts at the leaner side of the stoichiometric mixture fraction where there is sufficient oxidizer available for ignition. The temperature rise reaches the highest value at a mixture fraction close to  $\zeta_{st}$  for all dilution cases. To have a comprehensive comparison of autoignition of different dilution cases, the role of chemical and diffusion effects on autoignition are studied separately. In subsection 2.4.1, the chemical aspects of autoignition is investigated using dilution ratio as a key parameter. A homogeneous reactor model is employed to study autoignition considering pure chemical effects regardless of any diffusion effects. In subsection 2.4.2, the influence of diffusion effects on autoignition is investigated using strain rate as a controlling parameter.

### 2.4.1 Effect of dilution ratio $\Theta$

Dilution ratio plays a major role on the species mass fractions and temperature. To investigate the influence of dilution ratio on autoignition, a constant-pressure homogeneous reactor is used to compute autoignition time scales. The initial ( $t = 0$  s) distributions of species mass fraction and temperature, which are fully parameterized by the mixture fraction  $\zeta$ , are used as an input for the homogeneous reactor.  $\tau_{ign}$  is calculated based on the required time for 10K of temperature increase compared to the initial condition.

Figure 2.9a shows  $\tau_{ign}$  versus mixture fraction for different dilution cases and dilution ratios. Apparently, temperature increase occurs faster at a certain mixture fraction. The most reactive mixture fraction  $\zeta_{MR}$  is the mixture fraction that has the shortest  $\tau_{ign}$  and it is not necessarily the stoichiometric one [Mastorakos, 2009].  $\zeta_{MR}$  of Case O and B are very close to the oxidizer side; however in Case F, it is closer to the fuel side but still lower than  $\zeta_{st}$ . The minimum autoignition time, which is referred to as the reference autoignition time  $\tau_{ref}$ , mainly decreases with increasing dilution ratio as shown in Fig. 2.9b. This is caused by higher temperature



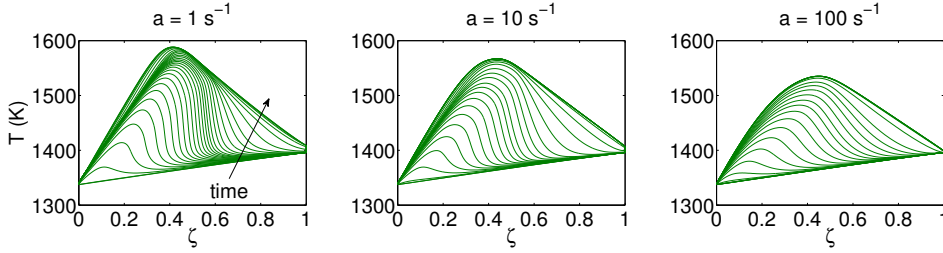


**Figure 2.10:** Evolution of temperature profile in mixture fraction space at different strain rates, Case B,  $\Theta=0.9$ .

levels at higher dilution ratios. At high dilution ratios, Case B ignites faster than the two other cases. However, at low dilution ratios, Case B is the slowest one. This complex chemical behavior might depend on the difference between the temperature and amount of  $\text{H}_2$  and  $\text{CH}_2\text{O}$  in the reactants (cf. Table 2.1) for various dilution cases. A small amount of  $\text{H}_2$  in the reactants and its conversion to  $\text{H}$  radical at high temperatures of the reactants can trigger autoignition via the chain branching reaction. More information about this behavior can be obtained by a detailed kinetic analysis of autoignition.

### 2.4.2 Effect of strain rate $a$

Diffusion effects may change  $\zeta_{\text{MR}}$  and autoignition by transport of mass and heat in the domain. Here, the strain rate is used as a parameter to control diffusion effects. Figure 2.10 presents temperature profiles of Case B at  $a = 1 \text{ s}^{-1}$ ,  $a = 10 \text{ s}^{-1}$  and  $a = 100 \text{ s}^{-1}$ . Some noticeable points can be observed: First,  $\zeta_{\text{MR}}$  is almost the same for different strain rates and is located on the lean side of the stoichiometric mixture fraction ( $\zeta_{st} = 0.4455$ ). It seems that  $\zeta_{\text{MR}}$  is not affected significantly by diffusion effects for a range of strain rates. It has to be mentioned the location of  $\zeta_{\text{MR}}$  is not always on the lean side. Depending on the boundary conditions, it can be located at the reach side, for instance, if temperature of the fuel is much higher than that of the oxidizer [Joannon et al., 2012]. Second, the temperature rise evolves from  $\zeta_{\text{MR}}$  to the highest value at a mixture fraction close to  $\zeta_{st}$  for all strain rates. It is obvious that at higher strain rates, the final temperature is lower. This is caused by the enhanced conduction of heat due to larger gradients at higher strain rates. Third, at lower strain rates, the temperature profile rises with a local increase initially and it tends to a more uniform distribution in the domain afterwards. However, at higher strain rates, it rises more uniformly from the beginning. This is caused by the enhanced heat transport due to the larger gradients at high strain rates. To have a detailed comparison of the temporal evolution of the temperature rise at different strain rates,  $\Delta T$  is introduced as a new parameter.  $\Delta T$  represents the highest temperature rise across mixture fraction space at each time:

$$\Delta T(t) = \max_{\zeta} (T(\zeta, t) - T(\zeta, 0)) \quad (2.16)$$

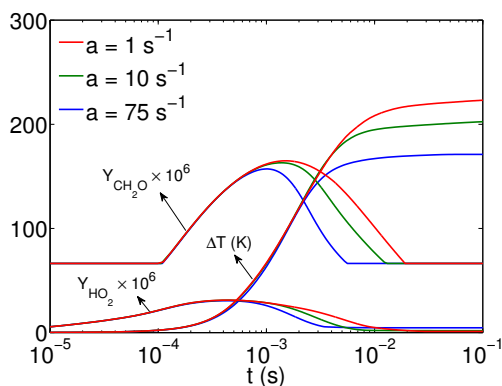


**Figure 2.11:** Evolution of  $\Delta T$  and peak mass fractions of  $\text{CH}_2\text{O}$  and  $\text{HO}_2$  at different strain rates, Case B,  $\Theta=0.9$ .

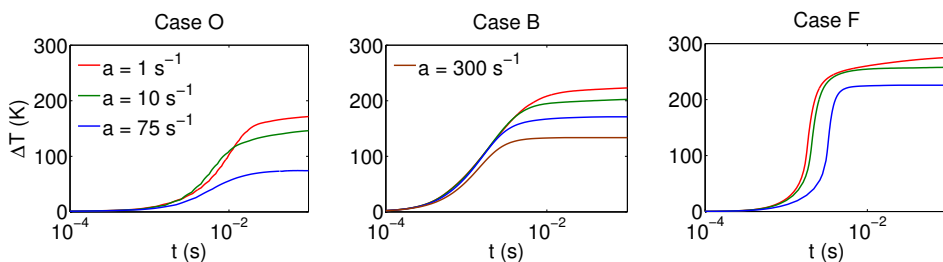


**Figure 2.12:** Evolution of  $\Delta T$  for dilution cases O, B and F at different strain rates,  $\Theta=0.9$ .

Figure 2.11 shows the time evolution of  $\Delta T$  compared to the evolution of the maximum concentration of pre-ignition intermediates  $\text{CH}_2\text{O}$  and  $\text{HO}_2$  during autoignition. It is observed that the trend of  $\Delta T$  complies very well with that of the species at all strain rates. It should be noted that the maximum concentrations are not zero at the beginning and end of the process because of the presence of these species in the reactants (cf. Table 2.1).

Figure 2.12 shows the evolution of  $\Delta T$  for all dilution cases and for a wide range of strain rates. At the very beginning of autoignition, there is almost no influence of scalar dissipation rate on the transport of heat inside the domain since it is assumed that ignition starts from the steady-state, frozen and mixed reactants. However, after the very first local temperature increase, heat loss due to conduction may start to play a role. This leads to a delayed ignition at sufficiently high scalar dissipation rate enforced by the strain rate. It also appears that except for the final values of  $\Delta T$ , the sensitivity of autoignition time scales to diffusion effects is the highest for Case F and it is the lowest for Case B. Autoignition of Case F and Case O is delayed due to heat transport from the hot domain to a cold boundary in  $\zeta$ -space by conduction. This results in a relatively large influence of conduction effects on

autoignition of these cases. Autoignition of Case B starts at nearly the same time for a range of  $a = 1 - 75 \text{ s}^{-1}$ , because the effect of heat transport from the domain to the boundaries is small due to the elevated temperatures of both boundaries (see Fig. 2.3). However, if we increase the strain rate to a very high value of  $300 \text{ s}^{-1}$  for this case, a small delay can be seen for autoignition. Therefore, molecular diffusion affects autoignition of case B as well as other cases but at much higher strain rates.

It can also be seen that at the strain rate of  $300 \text{ s}^{-1}$ , there is not a considerable amount of temperature increase at the end of the autoignition process. We have observed less than 1 K temperature increase at strain rate of  $500 \text{ s}^{-1}$  (not shown here). This indicates that the strain rates considered here are not small.

A comparison between autoignition of different dilution cases reveals that the order of ignition delays does not change due to diffusion effects. It can be seen that Case B ignites faster and Case O ignites slower than other dilution cases for the whole range of strain rates. This complies with the results that were seen in the previous subsection (Fig. 2.9). Consequently, it can be concluded that diffusion effects delay autoignition but the order of autoignition is determined mainly by chemical effects. It can also be seen that the evolution of  $\Delta T$  for Case F has a higher gradient than the other cases. This might be caused by the non-diluted oxidizer stream, which provides more oxygen at  $\zeta_{\text{MR}}$  for this case. It is worth to mention that a higher final value of  $\Delta T$  for one case does not necessarily mean a higher peak temperature in the steady-burning state compared to other cases. This is due to the different initial temperature distribution for different cases.

## 2.5 Evaluation of chemical scheme and transport model

In this section, the influence of using different chemical and transport models on autoignition is evaluated. Figure 2.13a shows the evolution of  $\Delta T$  obtained with various reaction mechanisms. It appears that autoignition is predicted approximately the same by the different mechanisms. Except for Konnov's mechanism which predicts a slightly larger ignition delay.

Considering that the multicomponent transport model used in this study is a computationally expensive model, simplified transports are evaluated as well. These simplified transports are used for time-dependent computations of our model. Figure 2.13b shows a comparison between different transport models used for prediction of autoignition. It evidences that simplified transport models except than unity Lewis number assumption show similar autoignition time scales. The presence of highly diffusive species such as  $\text{H}_2$  in the composition of the burned gas results in the poor prediction by the unity Lewis assumption.

## 2.6 Discussions

In this research, Mild combustion has been investigated in situations relevant to furnaces with internal recirculation of products under the stoichiometric feeding condition. In addition to this application, there are also other possibilities related

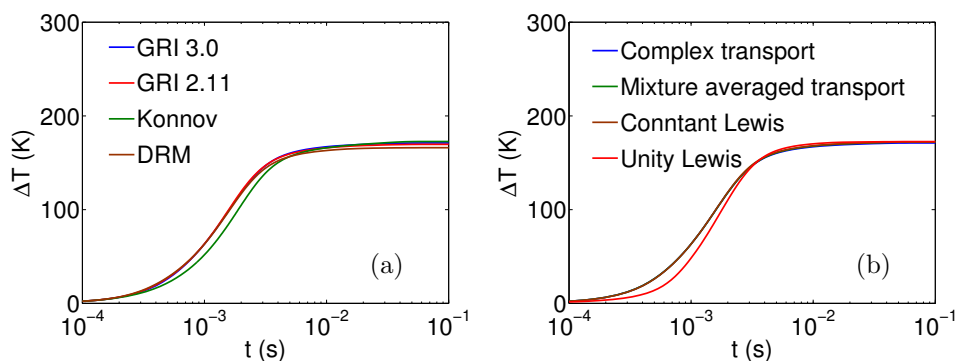


**Figure 2.13:** Evolution of  $\Delta T$  with different chemical schemes and transport models, Case B,  $\Theta=0.9$ ,  $a = 75 \text{ s}^{-1}$ .

to gas turbines and engines. The recent studies about these applications have been done by [Joannon et al. \[2009\]](#). They studied Hot Diluted Diffusion Ignition (HDDI) using counter flow diffusion flames by injection of diluted fuel into high-temperature oxidant. They also investigated another situation in which a stratified undiluted medium entrains into a high temperature dilutant which is relevant to Homogeneous Charge Diffusion Ignition (HCDI) [[Joannon et al., 2007](#)]. In both situations, they showed clearly how different types of combustion regimes such as Mild or High Temperature Combustion can be realized in different configurations by applying various conditions.

The observations in this research should be translated into practical situations with caution, since in practical situations streams needs to mix with burned gas. In this study, the effect of molecular diffusion has been investigated by considering the starting of autoignition from frozen and mixed reactants. This means that the fuel and oxidizer stream are assumed to be mixed on a molecular level before chemical reactions start. Simultaneous evolution of chemistry and diffusion processes occurs if the oxidizer and fuel streams are initially unmixed:  $\zeta = 1$  for  $x < 0$  and  $\zeta = 0$  for  $x > 0$ . This leads to (infinitely) large gradients of mixture fraction at the beginning of the process. Because of the intense scalar dissipation, the effect of diffusion processes becomes significant. While in this case the scalar dissipation rate is caused by the initial condition, its effect is similar to high gradients enforced by a high strain rate. Such an unmixed initial condition is more realistic which is investigated in chapter 4 where combustion models are developed to simulate practical Mild burners.

The turbulence transport may affect autoignition by retardation and providing conditions where the reaction zone is not characterized by flamelets. Furthermore, entrainment of the burned gas into reactants might not be accomplished before autoignition, or the burned gas might distribute unequally in the fuel and oxidizer streams. However, in simple laboratory configurations of furnaces working under flamelet regime conditions, above observations can be translated into practical situations. According to the stationary results, Case O seems to be an appropriate

case due to the lowest NO concentration among other dilution cases. However, in the design process of furnaces, autoignition of these cases should also be taken into account with the following considerations:

- A short autoignition time scale provides a reaction zone with a small lift-off height. Consequently, mixing of the burned gas with the reactants might not be accomplished.
- At a longer autoignition time scale, the reaction zone occurs far from the inlets. Although this situation satisfies the mixing time, design considerations of reactors, for instance, low material cost and space considerations have to be regarded.
- Faster rise of  $\Delta T$  results in a shorter thickness of the reaction zone. The length of the reaction zone mainly impacts convective and radiative transport of heat inside a reactor.

At high dilution ratios, Case B has the most interesting autoignition according to the shortest ignition delay and the least sensitive autoignition to the strain rate. However at low dilution ratios, Case O has the shortest ignition delay among the dilution cases. In addition, autoignition of Case O is less sensitive to dilution ratio which still autoignites within a few milliseconds when it is diluted for only  $\Theta = 0.7$ . For all dilution cases, NO formation strongly depends on the peak temperature and hence on the strain rate. A suitable dilution case should satisfy technological and environmental demands based on stationary and autoignition characteristics.

## 2.7 Conclusions

A numerical study has been carried out to investigate application of Mild combustion in furnaces in which burned gas might entrain into fuel and/or oxidizer stream(s) via internal recirculation. The main conclusions can be summarized as follows:

- Maximum temperature during the combustion process decreases with increasing dilution ratio for cases with diluted fuel as well as diluted air. This results in a similar behavior of the NO concentration for these dilution cases. Similar observations for different dilution cases have been reported by [Choi and Katsuki \[2002\]](#).
- A kinetic study of NO formation reveals that the Fenimore mechanism (prompt NO) is the dominant reaction pathway for all conditions studied here.
- The temperature rise of the dilution cases studied here starts at the leaner side of  $\zeta_{st}$  to the highest value at a mixture fraction close to  $\zeta_{st}$ . This behavior is in a qualitative agreement with the observations by [Cabra et al. \[2002, 2005\]](#) and the discussions in the review paper by [Mastorakos \[2009\]](#).
- Strain rate does not play a dominant role in the position of  $\zeta_{MR}$  in mixture fraction space.

- 
- The order of autoignition between different dilution cases changes at different dilution ratios.  $\tau_{ref}$  mainly decreases with increasing dilution ratio. The chemical processes behind such autoignition behaviors remain to be investigated.
  - Ignition delay of dilution cases is increased with increasing scalar dissipation rate. For Case B with hot boundaries this effect is much smaller than the other two cases.
  - Autoignition time scales of studied cases does not strongly depend on the applied chemical scheme and transport model. Small discrepancies are observed for different mechanisms and unity Lewis number assumption.



# Detailed computations of coflow diffusion flames

Realization of Mild combustion in large scale flows is a challenging field due to the stabilization of reaction zone by autoignition. Although Mild combustion occurs very often under turbulent conditions, laminar coflow diffusion flames make it possible to carry out detailed and precise numerical and experimental research. This is because of their relatively simple geometry, steadiness and optical accessibility. Accurate numerical information helps us to obtain a deep understanding of underlying processes in flame stabilization, reaction pathways of NO formation and effect of using different fuels under Mild condition. In addition to physical aspects, such numerical information can be used to assess chemical schemes and numerical models for simulations of Mild combustion.

In this chapter, first a numerical study is performed to analyze structure and stabilization mechanism of coflow flames in their transition from the “standard” condition to the Mild combustion regime. For this purpose, three CH<sub>4</sub>/N<sub>2</sub>/oxidizer coflow flames are studied with a systematic dilution and preheating of the fuel and coflow streams. Detailed computations are performed by steady-state simulations of these cases using detailed chemistry GRI-Mech 3.0, a multi-component mixture-

---

The content of this chapter has been extracted from the following papers:

S.E. Abtahizadeh, A. Sepman, J.A. van Oijen, A. Mokhov, L.P.H. de Goey, H. Levinsky, *Numerical and experimental investigations on the influence of preheating and dilution on transition of laminar coflow diffusion flames to Mild combustion regime*, Combustion and Flame, 160 (2013) 2359-2374.

A. Sepman, S.E. Abtahizadeh, A. Mokhov, J.A. van Oijen, H. Levinsky, L.P.H. de Goey, *Numerical and experimental studies of the NO formation in laminar coflow diffusion flames on their transition to Mild combustion regime*, Combustion and Flame 160 (2013) 1364-1372.

A. Sepman, S.E. Abtahizadeh, A. Mokhov, J.A. van Oijen, H. Levinsky, L.P.H. de Goey, *Experimental and numerical studies of the effects of hydrogen addition on the structure of a laminar methane-nitrogen Jet in Hot Coflow under Mild Conditions*, International Journal of Hydrogen Energy, 38 (2013), 13802-13811.

Minor adaptations have been performed to streamline the layout of the thesis. The contribution of the author is related to the computational part of the study. The experiments, which are used for the validation purposes, are performed by A. Sepman at RuG.



averaged transport and an optically thin approximation for radiative heat losses. Afterwards, a detailed analysis of NO formation is performed to clarify the ultimate low-NO<sub>x</sub> potential of Mild combustion. Finally, flexibility of Mild combustion to alternative fuels such as syn-gas is investigated by addition of hydrogen to the fuel stream.

## 3.1 Introduction

To understand the structure of Mild combustion, several experimental and numerical studies have been performed. On the experimental side, [Dally et al. \[2002\]](#) reported on a hydrocarbon jet issuing into a hot and diluted coflow (JHC) in the turbulent combustion regime. They performed single-point Raman-Rayleigh-LIF diagnostic techniques to measure temperature and species concentrations. This work was extended by [Medwell and Dally \[2012\]](#) by providing detailed measurements of temperature, OH and formaldehyde for a turbulent jet of a CH<sub>4</sub>/H<sub>2</sub> mixture in a hot and diluted coflow emulating Mild combustion conditions. [Oldenhof et al. \[2010\]](#) reported on LDA measurements of velocity field and CARS measurements for temperature and qualitative OH-PLIF data on a jet in hot coflow (JHC) burner developed at Delft (DJHC). Very recently, [Sepman et al. \[2013\]](#) performed spontaneous Raman scattering and LIF measurements of temperature and species concentrations in a laminar jet in hot coflow burner under Mild condition.

On the numerical side, most studies have been focused on the modeling of the JHC burner of [Dally et al. \[2002\]](#). [Christo and Dally \[2005\]](#) performed a detailed numerical study on the JHC flame to investigate the performance of various turbulent combustion models and chemical kinetic schemes. [Frassoldati et al. \[2010\]](#) numerically investigated the same burner to study the effect of inlet turbulence. Very recently, [Ihme and See \[2011\]](#) employed a three-stream flamelet/progress variable (FPV) model in Large Eddy Simulation (LES) of a JHC flame.

Although Mild combustion nearly always takes place under turbulent conditions, a deep understanding of the laminar flame structure is a basic ingredient of the modeling of turbulent flames. On the more fundamental side, one-dimensional counterflow diffusion flames have been studied to get insight into local combustion characteristics of non-premixed flames of Mild combustion [[Choi and Katsuki, 2002](#); [Joannon et al., 2012](#); [Abtahizadeh et al., 2012](#)]. On the more practical side, laminar coflow diffusion flames have been a standard object for the investigation of non-premixed combustion systems due to their relatively simple geometry, steadiness and optical accessibility. Most of the numerical and experimental studies of these flames have been reported for a cold oxidizer stream [[Smooke et al., 1996](#); [Bennett et al., 2000](#); [McEnally et al., 2000](#); [Toro et al., 2005](#); [Claramunt et al., 2006](#); [Consul et al., 2008](#); [Carbonell et al., 2009](#)]. To date, although substantial research has been performed on Mild combustion, little attention has been paid to the structure and stabilization of the reaction zone for this combustion regime in laminar situations. Novelty of the present work is the combined detailed computational and experimental study of laminar coflow flames with vitiated coflow and/or fuel stream(s).

Since a major driving force for implementing this technology is the reduction of

$\text{NO}_x$  emissions, understanding the mechanisms of  $\text{NO}_x$  formation under Mild conditions, and how the  $\text{NO}_x$  formation is affected by burner/furnace design and process conditions, is essential for further design efforts. The combined use of quantitative experimental methods and accurate numerical models in this situation is indispensable for analyzing the operative mechanism(s) of NO formation. Computations can provide this insight, also yielding parameters that are at best difficult to measure. One numerical study [Mancini et al., 2003] simulating a semi-industrial scale furnace under flameless oxidation conditions using a global chemical scheme concluded that the Zeldovich mechanism is responsible for NO formation. This conclusion is rather surprising since the intrinsically low oxygen content, leading to low instantaneous gas temperatures (generally below 1750 K) would seem to deemphasize Zeldovich in favor of the Fenimore mechanism. Quite oppositely to [Mancini et al., 2003], in the numerical works [Lee and Choi, 2009; Abtahizadeh et al., 2012] it was demonstrated that the Fenimore mechanism is a dominant source of the NO formation under Mild conditions. In [Sepman et al., 2013], measurements of NO mole fraction in an axisymmetric laminar-jet-in-hot-coflow (LJHC) burner showed that the NO formation in Mild flame is less than 2 ppm, in agreement with other experimental studies on Mild combustion in turbulent flows (cf. [Dally et al., 2002]). Many of these studies in turbulent situations address the NO formation under Mild combustion, however, there is a lack of a detailed numerical study on this subject for laminar situations.

Numerical and experimental investigations of burners operating in the Mild combustion regime and fed with methane and methane-hydrogen mixtures showed the need of a detailed chemistry approach [Parente et al., 2008] and the need of a proper turbulence/chemistry interaction treatment [Galletti et al., 2009] to capture the volumetric features of Mild combustion. The effect of the composition of methane/hydrogen mixture on Mild combustion was studied in [Ayoub et al., 2012] on a laboratory-scale facility. In [Sabia et al., 2007] it was shown that hydrogen oxidation kinetics significantly interacts with methane Mild Combustion. See also [Verissimo et al., 2011] for more references on the flameless oxidation of various fuels. We note that all above mentioned work was done in turbulent flames and, as mentioned earlier, it is worthwhile to be investigated using detailed numerical computations in laminar situations.

In this chapter, first we follow changes of the flame structure and stabilization mechanism in coflow flames upon their transition from the traditional coflow flames at normal flame conditions to the Mild regime. For this purpose, investigations are carried out for coflow flames that are burning with a varying degree of preheating and dilution of the coflow and fuel streams. Methane is chosen as the base fuel and it is diluted with various amounts of  $\text{N}_2$ . The predictive power of detailed computations using the GRI-Mech 3.0 [Smith et al., 2000] kinetic scheme, mixture-averaged multi-component transport and inclusion of radiative heat losses (except for Case M) are evaluated by comparison of profiles of temperature and species concentrations with measurements. In addition to detailed computations, extra computations have been performed to evaluate application of simplified transport models by assuming constant Schmidt numbers but different for all species. Afterwards, NO formation in these flames is analyzed to provide a deep insight into the ultimate low- $\text{NO}_x$  potential of Mild combustion. Finally, we expand our previous knowledge with

**Table 3.1:** Boundary conditions.

Case	$V(\text{m/s})^a$	$T(\text{K})^b$	Coflow				Fuel			$\zeta_{st}$	
			$X_{\text{O}_2}$	$X_{\text{N}_2}$	$X_{\text{H}_2\text{O}}$	$X_{\text{CO}_2}$	$V(\text{m/s})^a$	$T(\text{K})^b$	$X_{\text{CH}_4}$		$X_{\text{N}_2}$
Case NP	0.155	298	0.210	0.790	0	0	0.065	298	0.490	0.510	0.1412
Case P	0.347	780	0.210	0.790	0	0	0.123	780	0.200	0.800	0.3179
Case M	0.155	1530	0.036	0.732	0.145	0.087	0.058	1150	0.170	0.830	0.08917

<sup>a</sup> Mean exit velocities at standard condition ( $T = 273 \text{ K}$ ,  $P = 1013255 \text{ Pa}$ ).

<sup>b</sup> Mean temperatures at 3 mm above the exit plane.

investigations of flexibility of Mild combustion to alternative fuels such as syn-gas. To this end, hydrogen is added to the fuel and its influence on spatial structure and NO formation is studied.

## 3.2 Experimental setup

The experimental test cases are summarized in Table 3.1. The non-preheated and preheated flames, Case NP and P, respectively, are studied using a diffusion burner with electrical preheating of gases (Electrically Preheated Diffusion Burner) (EPDB), see Fig. 3.1a, while Case M is investigated using a Laminar Jet-in-Hot Coflow (LJHC) burner, see Fig. 3.1b. Both of these burners are developed at RuG. The coflow is supplied through this preheater to the settling compartment of the diffusion burner. The compartment (height 20 cm) is equipped with entrance and exit perforated planes and filled with glass beads to homogenate the velocity profile in the coflow. The fuel is supplied through the inlet at the side of the settling compartment. Diffusion flames burn above an upright tube carrying the  $\text{CH}_4/\text{N}_2$  fuel mixtures at different ratios (see Table 3.1 for details) surrounded by a coflow annulus with an outer diameter of 68 mm. The flame temperature and major species ( $\text{CO}$ ,  $\text{CO}_2$ ,  $\text{N}_2$ ,  $\text{H}_2$ ,  $\text{H}_2\text{O}$ ,  $\text{CH}_4$  and  $\text{O}_2$ ) were measured using spontaneous Raman scattering. More details can be found in [Sepman et al., 2013; Abtahizadeh et al., 2013]

The maximum temperature of the EPDB burner at the exit plane does not approach temperatures required for Mild combustion (approximately 1200 K). To reach these temperatures, the LJHC burner is used which is schematically shown in Fig. 3.1b. In this burner, the oxidizer can be considered as burnt products of one-dimensional premixed flames stabilized above the ceramic tile. These premixed flames are fed from underneath by lean  $\text{CH}_4$ /oxidizer mixtures with an equivalence ratio of approximately  $\phi = 0.8$ . The compartment located upstream of the ceramic burner is filled with glass beads to homogenize the velocity profile in the coflow. The quartz tube was used to improve the stability of the investigated flames and to prevent mixing of the oxidizer with ambient air. The coflow temperature was chosen to ensure self-ignition of the fuel/oxidizer mixture which needs to be higher than approximately 1200 K. A more detailed description of the burner is given in [Sepman et al., 2013].

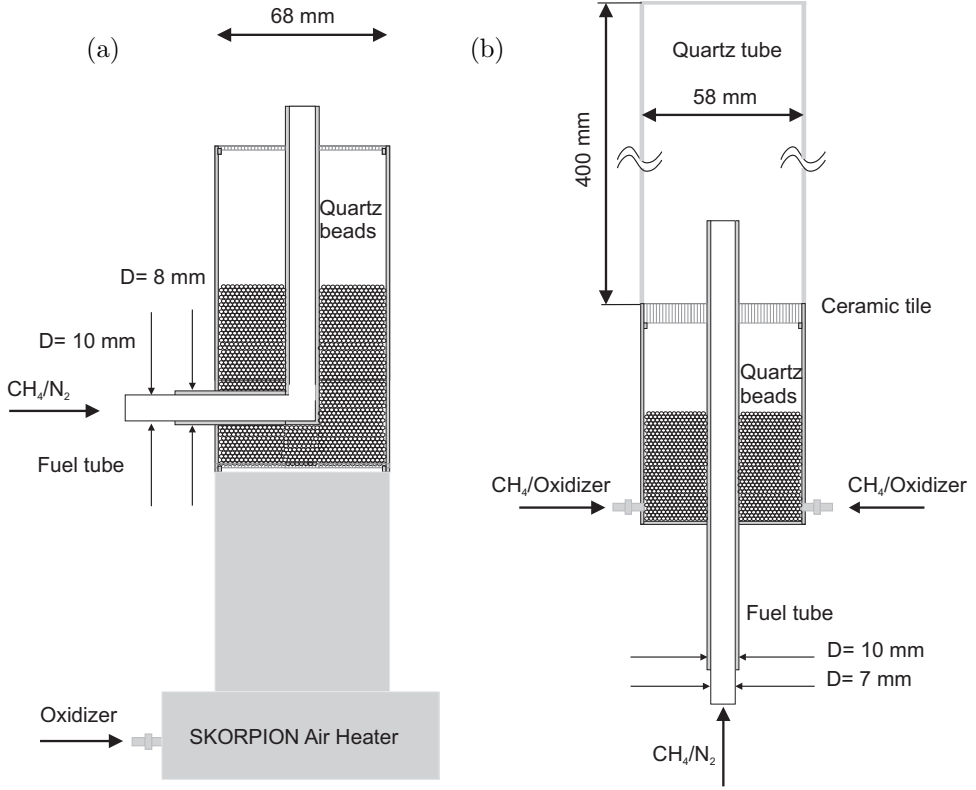


**Figure 3.1:** Schematic of the (a) electrically preheated diffusion burner and (b) laminar-jet-in-hot-coflow burner.

### 3.3 Mathematical model and numerical methodology

The laminar coflow flames are numerically computed by a set of conservation equations for mass, momentum, energy and species in a cylindrical coordinate system. The flow is considered as a continuous, multi-component, compressible, and thermally-perfect mixture of gases. A Newtonian flow is assumed and Soret and Dufour effects are neglected. The conservation equations using vector notation read:

$$\frac{\partial \rho}{\partial t} + \nabla \cdot (\rho \mathbf{U}) = 0 \quad (3.1)$$

$$\frac{\partial (\rho \mathbf{U})}{\partial t} + \nabla \cdot (\rho \mathbf{U} \mathbf{U} + p \mathbf{I}) = \nabla \cdot \boldsymbol{\tau} + \rho \mathbf{g} \quad (3.2)$$

$$\frac{\partial (\rho e)}{\partial t} + \nabla \cdot \left[ \rho \mathbf{U} \left( e + \frac{p}{\rho} \right) \right] = \nabla \cdot (\mathbf{U} \cdot \boldsymbol{\tau}) - \nabla \cdot \mathbf{q} + \rho \mathbf{g} \cdot \mathbf{U} \quad (3.3)$$

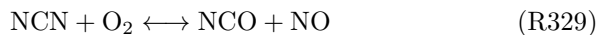
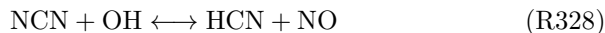
$$\frac{\partial \rho Y_i}{\partial t} + \nabla \cdot [\rho Y_i (\mathbf{U} + \mathbf{V}_i)] = \rho \dot{\omega}_i \quad (3.4)$$

where  $\rho$  is the mixture density,  $p$  is the total mixture pressure,  $\mathbf{U}$  is the mixture velocity vector,  $e$  is the total mixture energy,  $Y_i$  is the mass fraction of species  $i$ ,  $\dot{\omega}_i$  is the net rate of change of mass of the species  $i$ ,  $V_i$  is the diffusion velocity of gas species  $i$ ,  $\kappa$  is the thermal conductivity of the mixture,  $\tau$  is the fluid stress tensor,  $g$  is the acceleration vector due to the gravity and  $\mathbf{q}$  is the heat flux vector. The set of governing equations is solved using a finite-volume, adaptive mesh refinement (AMR), density-based computational framework that has been originally developed by Groth and co-researchers [Groth and Northrup, 2005; Northrup and Groth, 2005; Gao and Groth, 2010; Charest and Groth, 2010; Gao et al., 2011; Hernández-Pérez et al., 2011] at the University of Toronto. This framework has been applied to combusting flows including laminar atmospheric [Northrup and Groth, 2005; Gao and Groth, 2010] and high-pressure sooting flames [Charest and Groth, 2010], as well as turbulent premixed [Hernández-Pérez et al., 2011] and non-premixed [Gao and Groth, 2010; Gao et al., 2011] flames. This solver has been modified here to accommodate the configurations under consideration.

The GRI-Mech 3.0 [Smith et al., 2000] chemical mechanism is used to obtain the formation and destruction rates of chemical species. Some modification is done to the GRI-Mech 3.0 mechanism in order to incorporate updated NO chemistry with the NCN species (see [Sepman et al., 2011]). Namely, the reaction  $\text{CH} + \text{N}_2 \longleftrightarrow \text{HCN} + \text{N}$  in GRI-Mech 3.0 mechanism, is changed to



while keeping the same rate constant, and 4 reactions describing the reactions of NCN with O, H, OH, O<sub>2</sub> are added:



The computations are performed using rate coefficients for these four reactions taken from Lin and co-workers [Moskaleva and Lin, 2000; Zhu and Lin, 2005, 2007; Zhu et al., 2009]; the values used are summarized in [Sepman et al., 2011]. Transport is described by a mixture-averaged model in which the diffusion velocity of each individual species is computed assuming Fick-like diffusion. Thermodynamic properties, transport properties and species net production/destruction rates are all computed using the open-source package Cantera [Goodwin, 2003], which makes use of Wilke's formula to evaluate viscosity [Wilke, 1950] and a combination-averaging formula for thermal conductivity [Mathur et al., 1967].

The transport equations were solved on multi-block quadrilateral meshes employing a second-order spatial discretization. The inviscid flux at each cell face was evaluated using limited linear reconstruction. In particular, the Roe's flux function [Roe, 1981] with the Venkatakrisshnan's limiter [Venkatakrisshnan, 1993] were utilized. The viscous fluxes were evaluated utilizing a diamond-path reconstruction [Coirier, 1994]. The low-Mach number preconditioner described by Weiss and

Smith [1995] and the explicit multi-stage optimally-smoothing time marching scheme of van Leer et al. [1989] were employed to achieve steady-state numerical solutions.

The heat flux vector includes transport of energy through Fourier conduction, species diffusion with different heat content and radiation. Radiation is computed using an optically thin approximation. By assuming that the surrounding is cold, the radiative heat loss can be expressed as

$$Q_{rad} = -4\sigma K_p T^4, \quad (3.5)$$

where  $\sigma$  is the Stefan-Boltzmann constant and  $K_p$  denotes the Plank mean absorption coefficient of the mixture. This coefficient is evaluated from the major radiating species  $\text{CO}_2$ ,  $\text{H}_2\text{O}$  and  $\text{CO}$  and is given by

$$K_p = P_{\text{CO}_2} K_{\text{CO}_2} + P_{\text{H}_2\text{O}} K_{\text{H}_2\text{O}} + P_{\text{CO}} K_{\text{CO}}, \quad (3.6)$$

where  $P_i$  and  $K_i$  are the partial pressures and Plank mean absorption coefficients of species  $i$ , respectively. These coefficients are computed using a statistical narrow-band model and the dataset of Soufiani and Taine [1997].

Based on the previous experimental observations [Sepman et al.2, 2013], the temperature of the reaction zone in Case M is considerably lower than that of the Case NP and P. Therefore, for Case M there is a slight change of temperature between the coflow and reaction zone. In this condition, the optically thin approximation does not yield satisfactory results and it over-predicts radiative heat losses. Moreover, as it is shown in section 3.5, radiation losses do not play an important role especially at lower axial heights. Therefore, the radiative losses are neglected in computations of Case M. In summary, the radiation model based on the optically thin approximation has been incorporated in computations of Case NP and P and it is ignored in the computations of Case M.

### 3.4 Domain and boundary conditions

The schematic two-dimensional computational domain and boundary conditions used for the simulations are shown in Fig. 3.2. The necessary modifications have been incorporated in computational domain to account for differences between the two experimental burners. The velocity profile  $V(r)$  at the fuel inlet boundary follows a fully developed laminar pipe flow which has a parabolic profile, having zero values at the no-slip wall:

$$V(r) = V_{\text{fu}} \left[ 1 - \left( \frac{r}{r_{\text{fu}}} \right)^2 \right] \quad 0 < r < r_{\text{fu}} \quad (3.7)$$

The coflow has a uniform velocity  $V_{\text{co}}$  with the exception of a small boundary layer close to the fuel tube. In this boundary layer, the velocity profile is assumed to be parabolic to satisfy the no-slip boundary condition at the tube wall:

$$V(r) = \begin{cases} V_{\text{co}} \left[ 1 - \left( \frac{r-r_{\text{pa}}}{r_{\text{co}}-r_{\text{pa}}} \right)^2 \right] & \text{if } r_{\text{co}} < r < r_{\text{pa}} \\ V_{\text{co}} & \text{if } r_{\text{pa}} < r < r_{\text{o}} \end{cases} \quad (3.8)$$

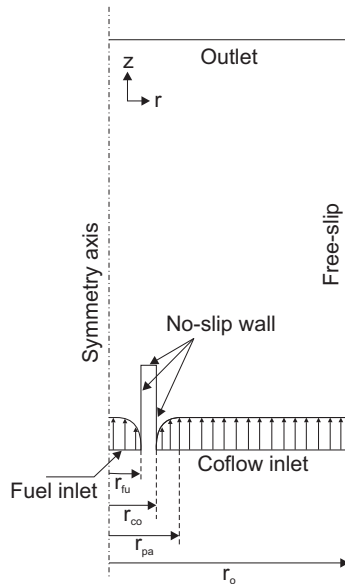


**Figure 3.2:** The computational domain and the boundary conditions.

$V_{fu}$  and  $V_{co}$  are peak values of velocity for fuel and coflow which are obtained from mean values in Table 3.1.  $r_{fu}$ ,  $r_{co}$  and  $r_o$  are the inner radius of the fuel tube, the outer radius of the fuel tube and the radius of the computational domain, respectively.  $r_{pa}$  is the radius at which the coflow velocity profile changes from a parabola to a uniform profile. The size of the computational domain is 30 mm width  $\times$  100 mm height, in which the length of the fuel tube is 10 mm. For Case NP and P,  $r_{fu}$ ,  $r_{co}$  are 4 mm and 5 mm, respectively, while for Case M,  $r_{fu}$  is slightly different and it is 3.5 mm. The thickness of the boundary layer  $r_{pa} - r_{co}$  is assumed to be 1 mm. Since the length of the fuel tube is sufficiently long (10 mm), allowing the flow to develop downstream, the results are not very sensitive to this choice.

The inlet temperature profiles have a uniform value for Case NP and P since there is no temperature difference between the fuel and oxidizer streams. However, in Case M, there is a temperature difference of approximately 500 K between the fuel and coflow that needs to be accounted for. The fuel tube is assumed to be an iso-thermal wall, having the same temperature as the fuel stream. To account for the temperature difference between the fuel tube and the coflow, a parabolic temperature profile is considered at the inlet of the coflow that changes from the fuel temperature to the coflow temperature. The thickness of this thermal boundary layer is taken the same as that of the velocity one, corresponding to a Prandtl number close to unity.

The inlet temperature profile of the coflow is therefore similar to the velocity

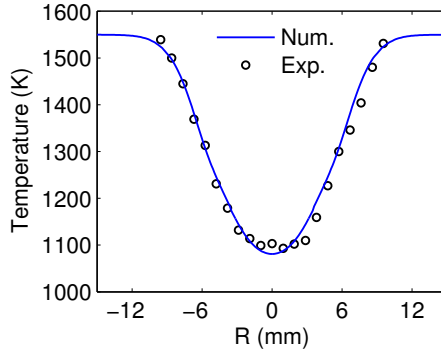


**Figure 3.3:** Comparison of computed temperature against measurements for the non-reacting case (Case A2 [Sepman et al.2, 2013]) at 3 mm above the burner.

one:

$$T(r) = \begin{cases} T_{fu} & \text{if } r < r_{fu} \\ (T_{co} - T_{fu}) \left[ 1 - \left( \frac{r - r_{pa}}{r_{co} - r_{pa}} \right)^2 \right] + T_{fu} & \text{if } r_{co} < r < r_{pa} \\ T_{co} & \text{if } r_{pa} < r < r_o \end{cases} \quad (3.9)$$

where  $T_{co}$  is the peak inlet temperature value which is obtained from mean values provided in Table 3.1. The outer boundary of the domain is considered adiabatic. This set of boundary conditions has been validated with the measured values of temperature for the non-reacting case of Case M (see Case A2 in [Sepman et al.2, 2013]) in Fig. 3.3. In this case,  $\text{CH}_4$  has been completely removed from the composition of the fuel stream of Case M and it has been replaced by  $\text{N}_2$  to avoid any possible reaction. Figure 3.3 indicates that the computed temperature according to the chosen initial profiles corresponds very well with the measured values at a height of 3 mm above the fuel tube exit. The computational mesh has been resolved up to three levels of refinement based on gradients of temperature and species. This yields a converged solution with an approximately 20000 cells with the minimum cell width  $\Delta x = 0.04$  mm.

### 3.5 Structure and stabilization mechanism of coflow flames

This section comprises numerical and experimental results and a discussion about the structure of the investigated flames. In subsection 3.5.1, radial profiles of temperature and species concentrations are compared against the measurements for all cases. Results of application of a simplified transport model and neglecting radiative heat losses in the computations are also represented in this subsection. Subsection 3.5.2 includes discussions about stabilization and structure of these flames by analysis of temperature and heat release profiles. Further analysis of the flame structure has



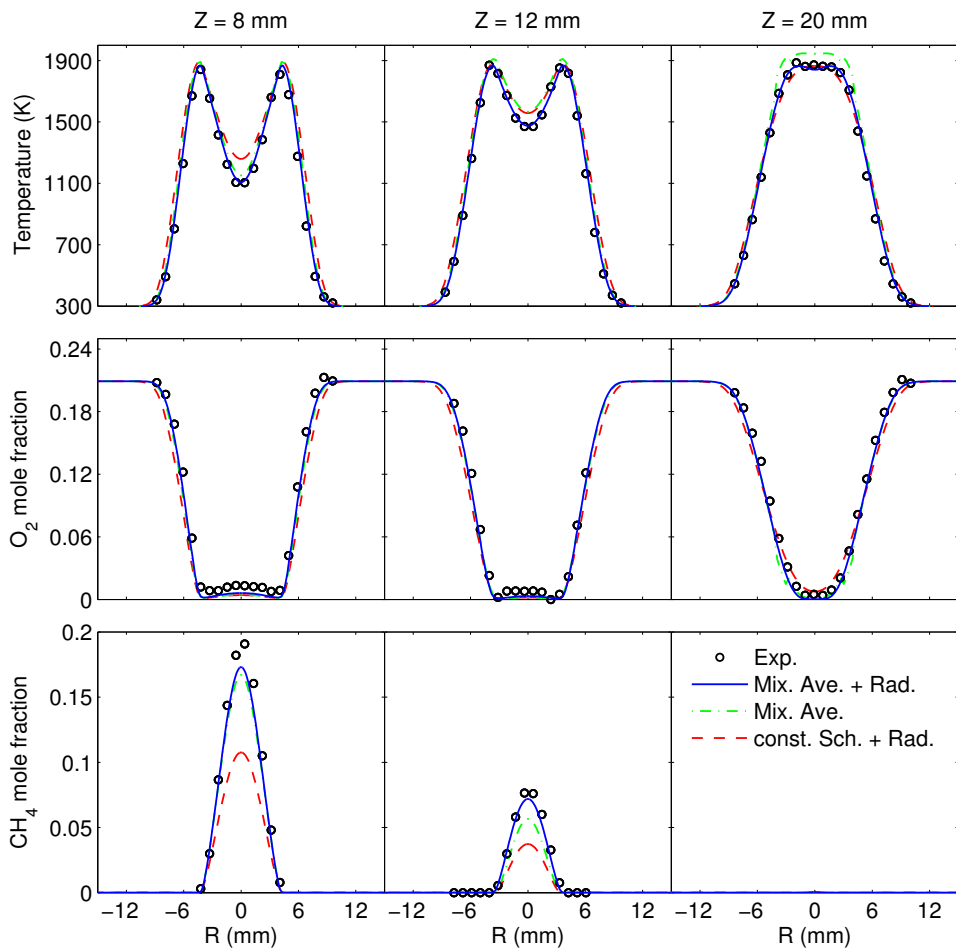


**Figure 3.4:** Comparison of (circles) measured and (lines) computed radial profiles of temperature and major species concentrations for Case NP at three different heights. Computations with (solid lines) mixture-averaged multicomponent transport and radiative heat loss, (dashed-dotted lines) mixture-averaged multicomponent transport without radiative heat loss and (dashed lines) assuming constant Schmidt numbers with radiative heat loss.

been performed in mixture fraction space and it is presented in subsection 3.5.3.

### 3.5.1 Radial profiles

The experimental radial profiles of temperature and major species mole fraction are presented in Figs. 3.4, 3.5 and 3.6 for Case NP, P and M, respectively. Three axial positions are considered that illustrate the progress of combustion for each case. The measurements are compared with the results of the computations. The experimental temperature profiles in Case NP and P demonstrate the evolution of the wishbone

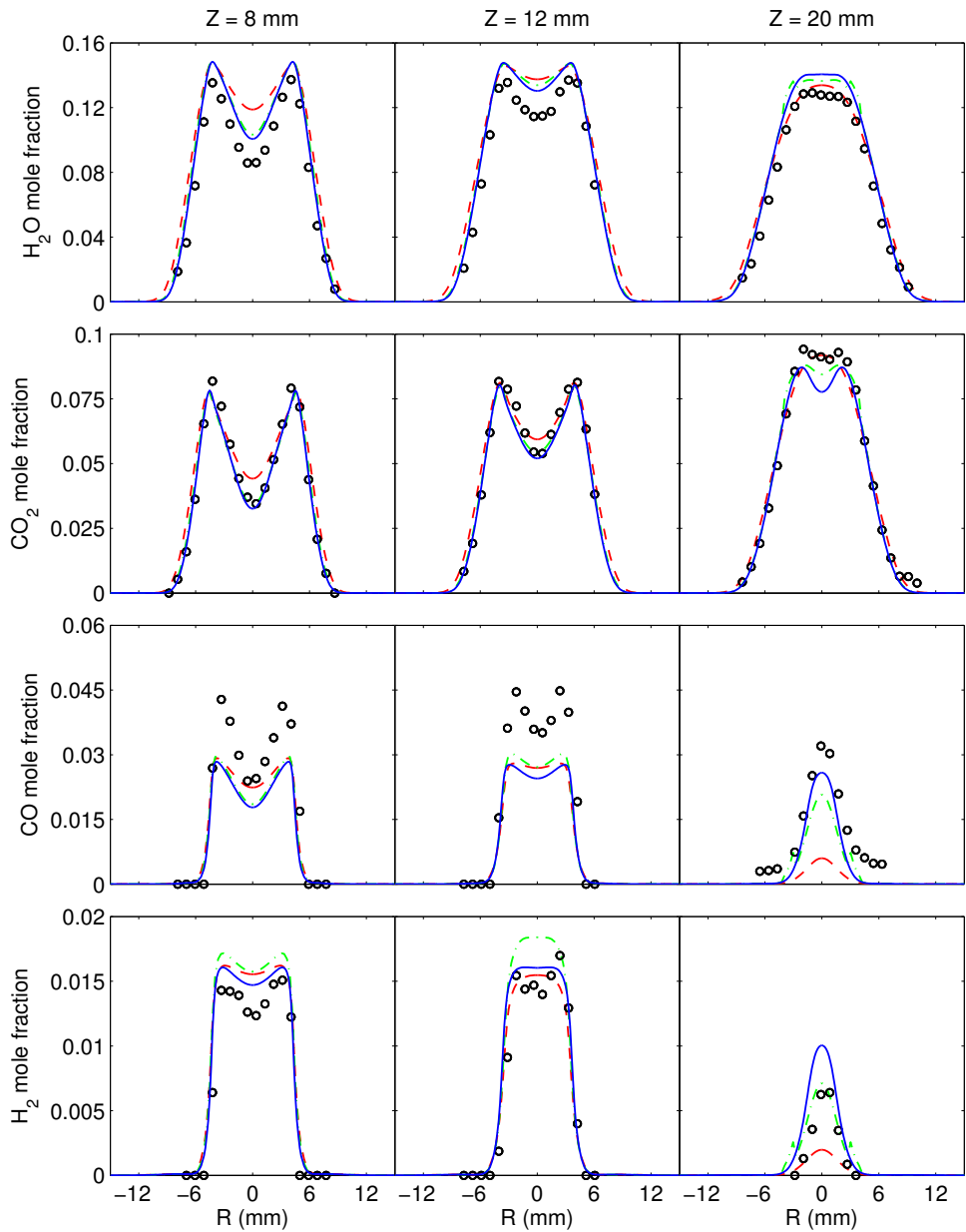


Figure 3.4: Continued from the previous page.

structure, the minimum along the axis disappears progressively downstream. The major species mirror the changes observed in the temperature profiles, indicating the expected progress of combustion in a non-premixed flame. The progress of com-

bustion in Case M is also reflected in the development of temperature. However, the details of the evolution are considerably masked by the large temperature difference between the coflow and fuel. The development of the major species profiles for this flame is consistent with the temperature changes, although their analysis is complicated since the coflow is composed of combustion products of the lean mixture.

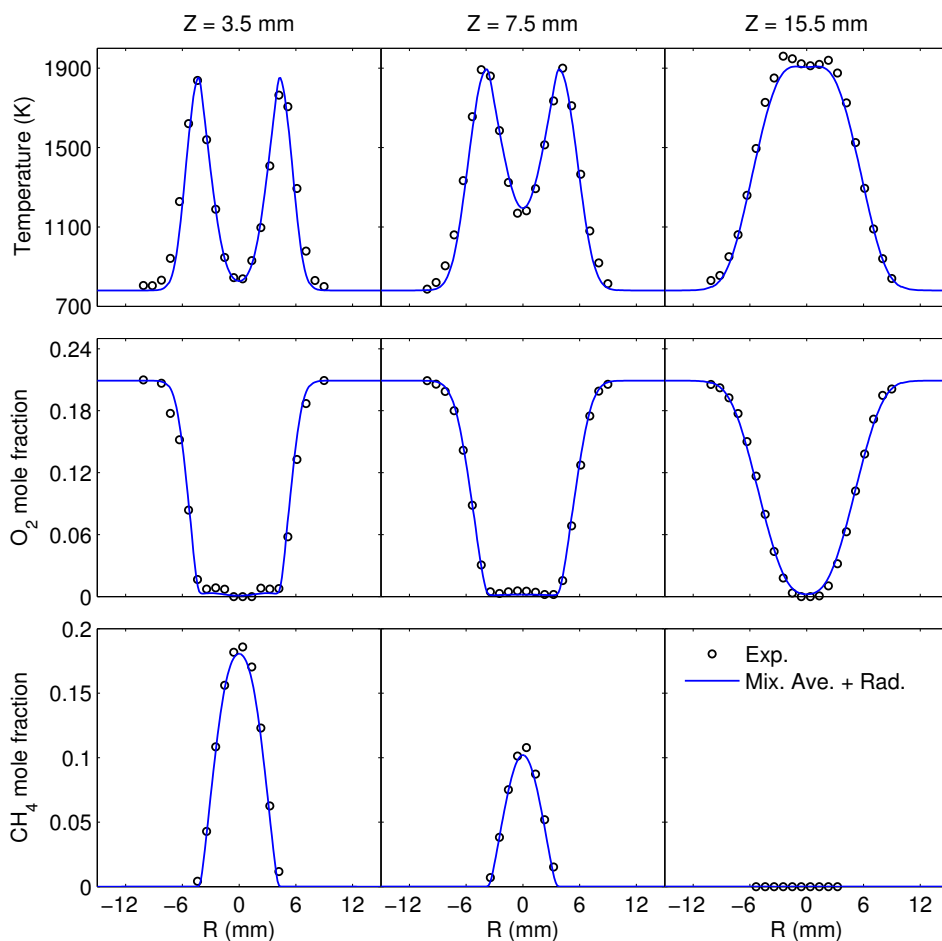
The detailed computations of Case NP reproduce the experimental results very accurately for temperature,  $O_2$ ,  $CH_4$ ,  $H_2$  (see Fig. 3.4) and  $N_2$  (not shown here). The  $H_2O$  mole fraction is generally a little over-predicted by approximately 10–20% (just outside the stated accuracy of the Raman measurements). The profiles of  $CO_2$  are in a nearly quantitative agreement, with the exception that the computations predict lower  $CO_2$  mole fractions near the centerline at 20 mm height. The  $CO$  profiles are under-predicted. We remind here that for mole fractions  $< 0.05$ , the accuracy of the measurements deteriorates. In general, the experimental and predicted results agree almost perfectly for Case NP. The small discrepancies can be attributed to an error in the vertical position where the horizontal profiles were measured.

Figure 3.4 also includes the computations assuming constant Schmidt numbers but different for each species. The Schmidt numbers are obtained from the steady-state solution of a 1D counterflow diffusion flame with a more detailed transport model. Boundary conditions of these flames are chosen according to Table 3.1 with applied strain rate  $a = 100 \text{ s}^{-1}$ . To further avoid computation of pure species transport properties for 2D simulations, the following relations are used for viscosity and thermal conductivity:

$$\frac{\mu}{c_p} = 2.1 \times 10^{-5} (T/298)^{0.7} \quad (\text{kgm}^{-1}\text{s}^{-1}) \quad (3.10)$$

$$\lambda = \frac{\mu c_p}{Pr} \quad (\text{Wm}^{-1}\text{K}^{-1}) \quad \text{with } Pr = 0.7 \quad (3.11)$$

This assumption yields worse predictions than the mixture-averaged transport mostly at the centerline for temperature and species concentrations. By assuming constant Schmidt numbers, the predicted values of temperature at the centerline for  $Z = 8$  and 12 mm are larger than those of the mixture-averaged model. This is consistent with the lower prediction of  $CH_4$  and slightly lower  $O_2$  together with larger predictions of  $H_2O$ ,  $CO_2$ ,  $CO$  and  $H_2$  by using this approach. The change of  $O_2$  at the centerline is not noticeable in Fig. 3.4 since there is a very small amount of  $O_2$  present in the centerline. At  $Z = 20$  mm, an opposite trend can be found by looking to the concentrations of  $O_2$ ,  $H_2O$ ,  $CO$  and  $H_2$ , which corresponds to earlier termination of the reaction zone predicted by this approach. Consequently, the predicted reaction zone by the mixture-averaged transport model is larger than for the constant Schmidt numbers case. The constant Schmidt number approach yields better quantitative agreement only for concentrations of  $CO_2$  and  $H_2O$  at  $Z = 20$  mm. The effect of neglecting radiation in the calculation is also included in Fig. 3.4. It is seen that radiation losses do not influence the predictions considerably, especially at lower axial distances  $Z$ . However, the effect becomes more important at higher axial distances. This occurs due to the fact that a parcel of burned gas, traveling in the axial direction emits radiative heat. Therefore, the radiative heat loss increases by increasing axial distance.



**Figure 3.5:** Comparison of (circles) measured and (lines) computed radial profiles of temperature and major species concentrations for Case P at three different heights. Computations with (solid lines) mixture-averaged multicomponent transport and radiative heat loss and for CO (see next page) at (dashed lines) 0.5 mm below the specified heights and (dotted lines) 0.5 mm above the specified heights.

The measured temperature and species for Case P agree quantitatively with the computations (see Fig. 3.5), with the exception of CO at  $Z = 15.5$  mm that is under-predicted by 20%. We can explain such a difference considering the fact that concentration of CO along the centerline indicates a very steep gradient close to the flame front position ( $Z = 15$  mm). It can be observed from Fig. 3.5 that CO mole fraction decreases almost 2 times from 15 to 16 mm. Therefore, uncertainties related to determination of the vertical position may have a large effect. Besides, for species with a mole fraction less than 0.05, the accuracy of the measurements deteriorates to at most 0.015 mole fraction which eventually leads to a relatively

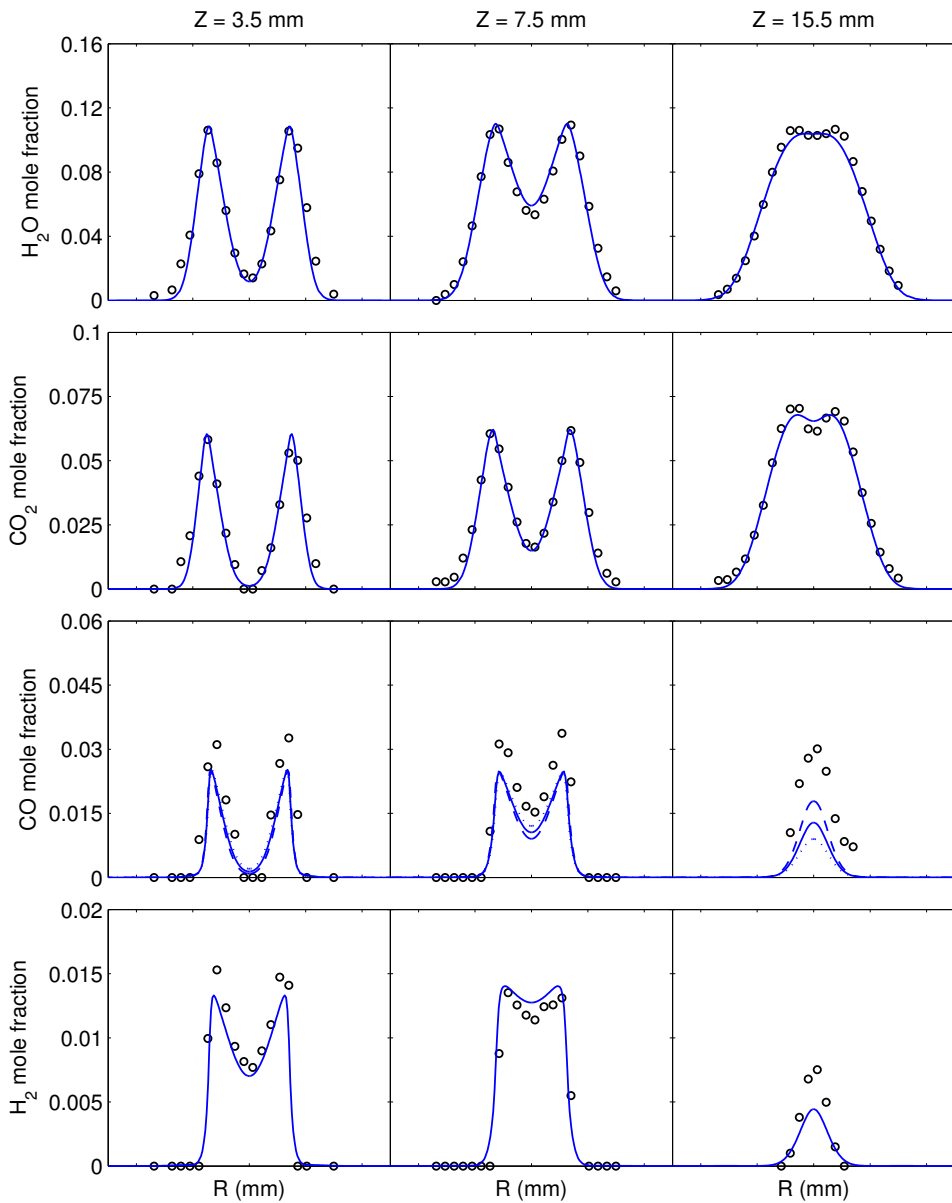


**Figure 3.5:** Continued from the previous page.

large uncertainty in the absolute measured CO mole fraction.

Turning to the measurements of Case M (Fig. 3.6), this flame is less stable than the other two flames, meaning that Raman spectra are noisier for this case than those in Case NP and P which leads to development of instabilities downstream.

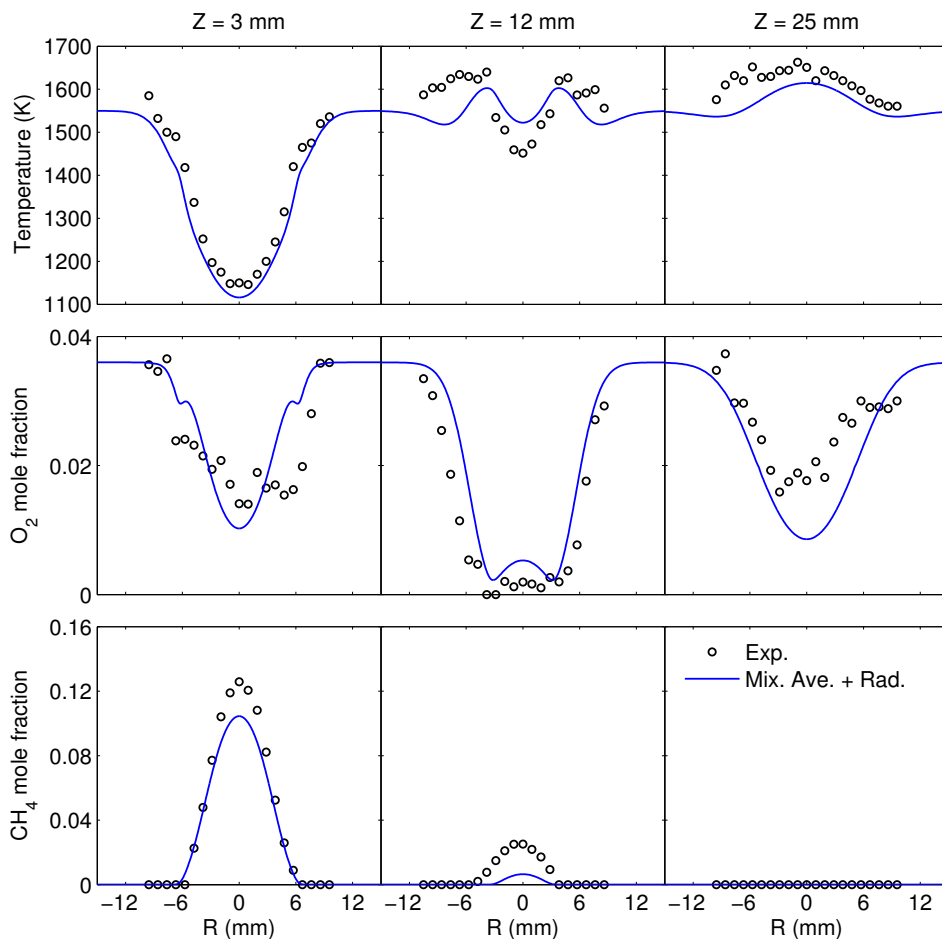


**Figure 3.6:** Comparison of (circles) measured and (lines) computed radial profiles of temperature and major species concentrations for Case M at three different heights. Computations with mixture-averaged multicomponent transport and without radiative heat loss at the specified heights.

Moreover, the temperature and species profiles at downstream distances indicate a slight non-symmetrical structure of the flow pattern. The slightly asymmetrical flow pattern of the hot coflow oxidizer (burned products of the lean  $\text{CH}_4/\text{air}$  mixture) leads to a small tilt of the flow. In the measurements, it is observed that the tip of the flame (at approximately 25 mm) is shifted by a few millimeters distance (about 1-2 mm) from the centerline. The effect of the flow pattern of the coflow on the symmetry of the radial profile diminished with decreasing the axial distance, being completely unnoticeable already at the height of 9 mm. This difference in the axial symmetry of the flow pattern of the hot coflow resulted in slightly higher temperatures on one side of the downstream radial temperature profile. Unfortunately, all efforts to make

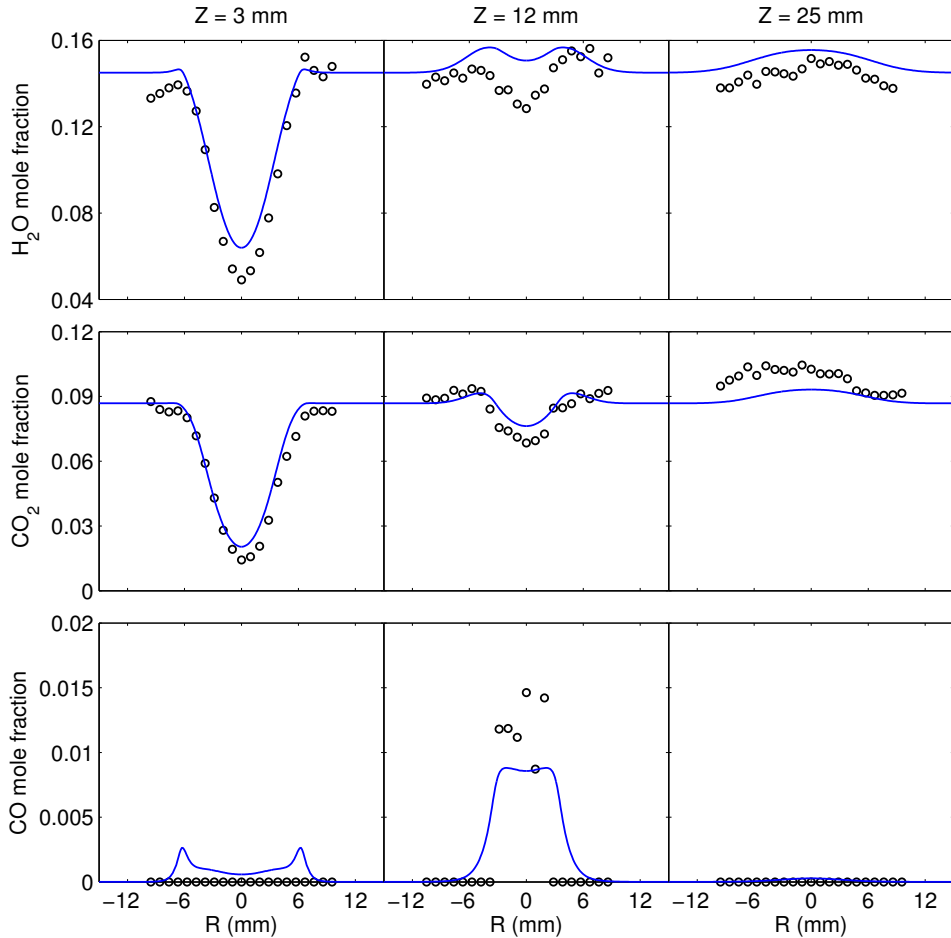
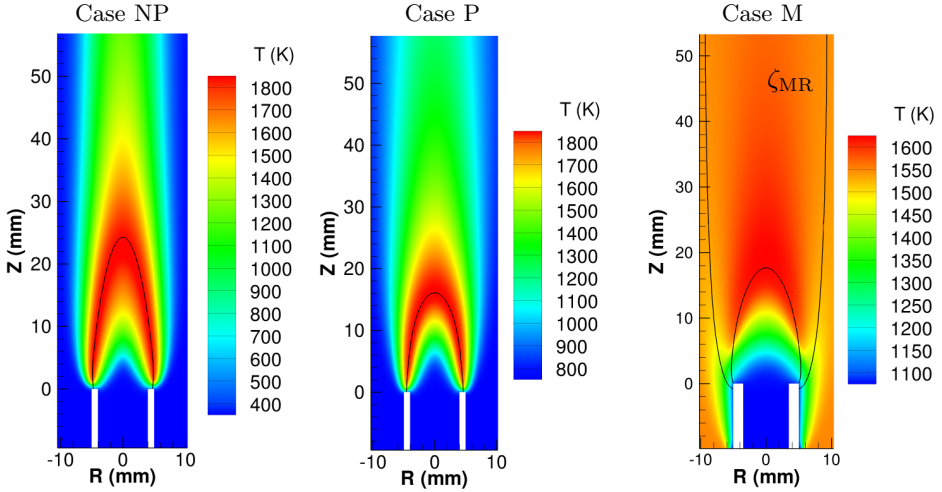


Figure 3.6: Continued from the previous page.

the flow pattern more symmetrical did not improve the situation significantly. We further note that the analysis was performed mainly at distances where deviations from radial symmetry were not significant.

The computational temperature agrees quantitatively with the experiments, with the exception of a number of points at axial distances of 12 and 25 mm, where the computations predict lower temperatures ( $< 100$  K). The  $\text{CH}_4$  consumption is over-predicted at 3 and 12 mm heights. The computational  $\text{H}_2\text{O}$  and  $\text{CO}_2$  profiles at these axial distances are located systematically above the experimental data. The difference in case of  $\text{H}_2\text{O}$  profiles is approximately 5-15% (comparable to the uncertainty of measurements), and in case of  $\text{CO}_2$  profiles, it is smaller than 10%. The under-prediction of  $\text{CH}_4$  and over-prediction of  $\text{H}_2\text{O}$ , apparently indicate that the computational flame develops faster than the real one. Such a behavior, in addi-



**Figure 3.7:** Two-dimensional false color plots of the computed temperature for Cases NP, P and M. The black line shows the stoichiometric mixture fraction  $\zeta_{st}$ . The black line showing  $\zeta_{MR}$  is labeled explicitly.

tion to asymmetrical flow pattern of experiments, might be caused by uncertainties in the reaction mechanism. The well established GRI-Mech 3.0 mechanism has not been validated under the conditions relevant to Mild combustion similar to any other mechanisms. A comparison with other kinetic mechanisms is of interest but lies outside the scope of present work. Such a comparison of various reaction mechanisms has been performed in 1D simulations of Mild combustion in chapter 2 in which small differences have been observed for predicted autoignition time scales. Such differences may affect the quantitative agreement between the computations and measurements; however, they do not affect the general structure of the computed flames and the main conclusions of this study.

### 3.5.2 General structure of flames

To illustrate the overall flame structure, two-dimensional false color plots of the computed distribution of temperature for the three flames are presented in Fig. 3.7. The stoichiometric mixture fraction contours based on Bilger’s formula [Bilger, 1988] are also shown in this figure. Here, we see, as in many earlier studies [Smooke et al., 1996; Toro et al., 2005; Liu et al., 2006], the characteristic high-temperature wish-bone structure of the coflow diffusion flames. The maximum measured temperature in Case NP and P is approximately 200 K higher than that of Case M. We further note that in all three cases, the computed temperature never approaches (by far) the adiabatic stoichiometric temperature of fuel and air mixture (Case NP:  $T_{st,ad} = 2040$  K, Case P:  $T_{st,ad} = 2114$  K and Case M:  $T_{st,ad} = 1790$  K). Main reasons include heat loss and conduction of heat in the domain. The broadening of the high temperature zone in Case M is notably larger than those in Case NP and P.

We note that the temperature rise in Case NP and P occurs very close to the



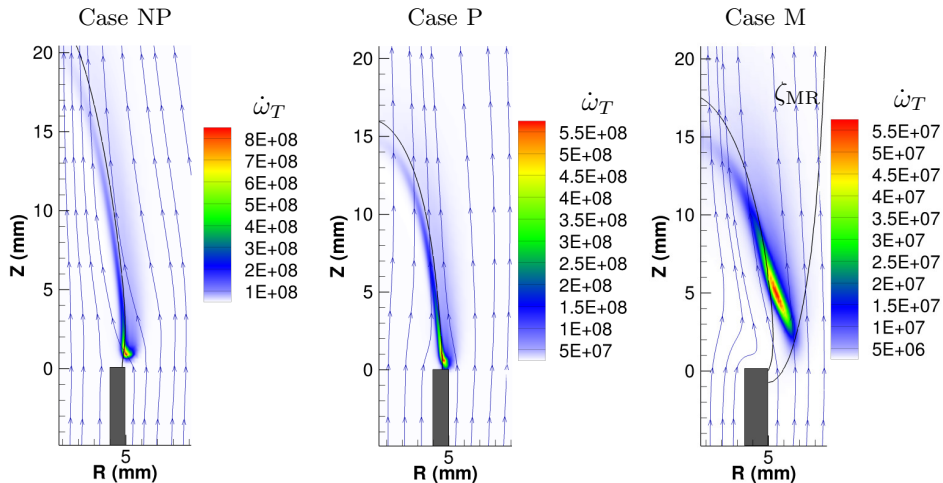


**Figure 3.8:** Two-dimensional false color plots of the computed heat release  $\dot{\omega}_T$  ( $\text{W}/\text{m}^3$ ) for Cases NP, P and M. The blue lines with arrows represent streamlines of the velocity field. The black lines show stoichiometric mixture fraction. The black line showing  $\zeta_{\text{MR}}$  is labeled explicitly.

burner outlet, just above the fuel tube, similar to the non-preheated methane/nitrogen and (hydrogen/nitrogen) laminar diffusion flames in [Smooke et al., 1996; Toro et al., 2005]. In contrast, a significant temperature rise in Case M is evident further downstream. Such a behavior apparently points to the fact that in Case NP and P the flame stabilizes close to the burner tip, while in Case M ignition occurs after mixing of the oxidizer and fuel. The flame structure of Case M visually resembles one of the autoigniting flames reported by Choi and Katsuki [2002]. In their paper, the autoignition characteristics of laminar lifted flames have been investigated experimentally for methane, ethylene, ethane, and n-butane fuels in preheated coflowing air. They observed a reaction zone in Mild combustion regime when the mole fraction of methane in the fuel (methane-nitrogen) and the temperature of the reactants were 0.045 and 1010 K, respectively.

The above comments are supported by the computed heat release rate distributions shown in Fig. 3.8. The analysis of Figs. 3.7 and 3.8 reveals that the location of maximum temperature is very close to the position of the maximum heat release. The region of the high heat release rate in Case M is considerably broader than in Case NP and P without considering the values. The location of the maximum heat release is close to the stoichiometric mixture fraction for all cases. From Fig. 3.8, it is also apparent that stabilization of Case NP and P occurs by an edge flame which is characterized by a peak in the heat release near the stoichiometric plane and forms the edge of a trailing diffusion flame [Buckmaster, 2002]. This edge flame propagates against the flow and stabilizes on the rim of the fuel tube. However, the flame temperature of Case M is too low (compared to adiabatic flame temperature of a stoichiometric mixture) to support an edge flame that can propagate upstream. This induces that Case M is most likely stabilized by autoignition.

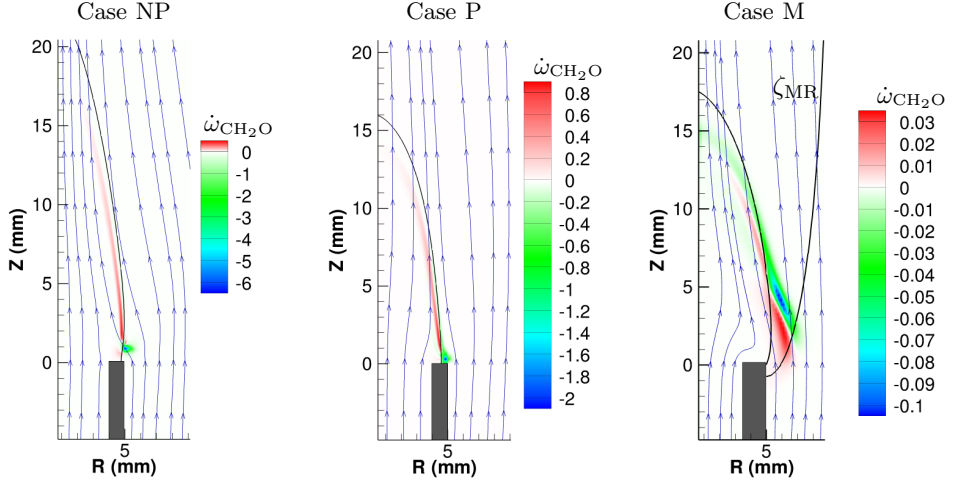


**Figure 3.9:** Two-dimensional false color plots of the computed source term of formaldehyde  $\text{CH}_2\text{O}$  ( $\text{kmol/m}^3\text{s}$ ) for Cases NP, P and M. The blue lines with arrows represent streamlines of the velocity field. The black lines show the stoichiometric mixture fraction. The black line showing  $\zeta_{\text{MR}}$  is labeled explicitly.

Such an autoignition structure is further investigated by plotting the contours of source terms of formaldehyde in Fig. 3.9. It is evident that for Case NP and P,  $\text{CH}_2\text{O}$  is formed downstream of the maximum heat release and it diffuses upstream towards the maximum heat release location where it is consumed. On the other hand, for Case M,  $\text{CH}_2\text{O}$  is produced at the upstream side of the maximum heat release close to the fuel tube and it is consumed downstream of the maximum heat release location. Such a structure, which has been reported in the literature for autoigniting flames [Gordon et al., 2008], further emphasizes the stabilization of Case M by autoignition.

The distribution of  $\dot{\omega}_T$  and  $\dot{\omega}_{\text{CH}_2\text{O}}$  can be analyzed in terms of most reactive mixture fraction  $\zeta_{\text{MR}}$ . This value has been obtained from the solutions of a homogeneous reactor for the frozen mixtures of Case M that are shown in Fig. 3.10. The ignition delay  $\tau_{\text{ig}}$  is defined based on 50 K increase of temperature in the homogeneous reactor. The most reactive mixture fraction [Mastorakos, 2009]  $\zeta_{\text{MR}}$  is the mixture fraction with the shortest ignition delay.  $\zeta_{\text{MR}}$  is found at  $\zeta = 0.0105$  and it is plotted in Figs. 3.7, 3.8 and 3.9. From these figures, it can be seen that formation of  $\text{CH}_2\text{O}$  and initiation of heat release  $\dot{\omega}_T$  occurs at the most reactive mixture fraction  $\zeta_{\text{MR}}$ . The  $\zeta_{\text{MR}}$  is positioned at the lean side due to high temperature and availability of small amount of  $\text{O}_2$  in the coflow side. This corresponds with previous studies about transient counterflow diffusion flames in Mild regime in [Mastorakos, 2009; Abtahizadeh et al., 2012; Sorrentino et al., 2013].

Influence of heat release on the flow field is investigated by plotting iso-contour of maximum density gradient in Fig. 3.11. Additional streamlines are plotted close to maximum heat release for further clarification. It is observed that streamlines expand at the density iso-contours and also around the maximum heat release for

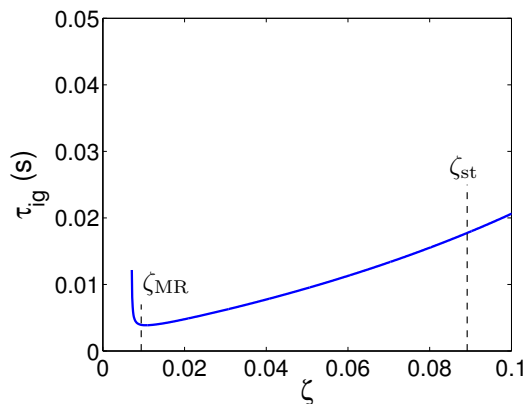


**Figure 3.10:** Ignition delay  $\tau_{ig}$  against mixture fraction obtained from simulations of a homogeneous reactor for Case M.

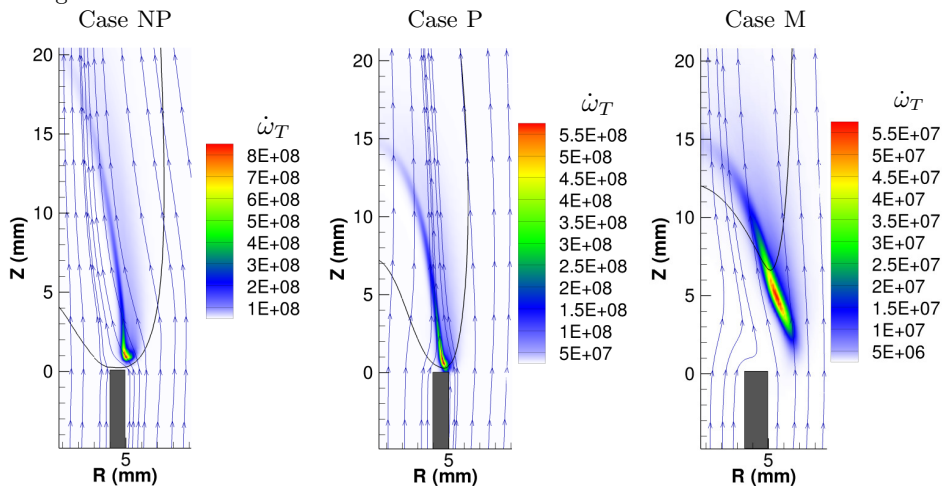


**Figure 3.11:** Two-dimensional false color plots of the computed heat release  $\dot{\omega}_T$  ( $\text{W}/\text{m}^3$ ) for Cases NP, P and M. The lines with arrows represent streamlines of the velocity field. The black lines show iso-contour of density corresponding to the maximum density gradient.

all cases. Such an expansion occurs very close to jet exit for case NP and P and further downstream for case M. It is noted that the gradients of density in the Case NP and P are much higher than in Case M which results in the stronger inward bending of streamlines crossing these iso-contours. Streamlines, in all cases, expand where the density decreases due to an increase in temperature as a result of heat release. It is observed that streamlines of fuel stream close to the tube wall are curved outward. This occurs due to shear stress of the shear layer between the coflow and fuel streams. Such an outward curvature is larger in Case M due to higher velocity difference between coflow and fuel in which velocity of coflow is almost 3 times higher than velocity of fuel (see Table 3.1). This outward curvature is weaker in

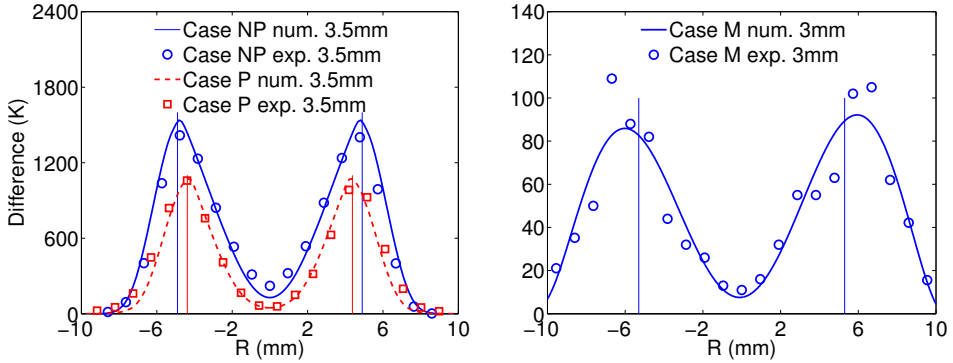


**Figure 3.12:** Measurements and computations of the temperature increase due to reaction from the frozen mixing of the fuel and coflow stream in the vicinity of the burner outlet (approximately 3 mm). The vertical lines refer to  $\zeta_{st}$  (see Table 3.1) for each case.

Case NP and P, due to the smaller differences between velocities of fuel and coflow and stronger effect of density gradients. We note that the thickness of tube wall is also higher in Case M which also enhances such an outward curvature.

The significant difference in temperatures of the coflow and fuel in Case M complicates the comparison of the combustion processes in the investigated flames. In an attempt to simplify the comparison, we plot the measured and computed differences between the radial temperature profiles in the vicinity of the burner outlet approximately 3 with the one corresponding to frozen (no chemical activity) mixing between coflow and fuel, see Fig. 3.12. In Case NP and P, the temperatures of the frozen mixing are 298 K and 780 K, respectively. In Case M, we used the temperature profile measured without  $\text{CH}_4$  in the fuel at the same axial distance as the frozen distribution, (see Case A2 in [Sepman et al.2, 2013]). The modest temperature rise in Case M reflects the very modest heat release, compared to Case NP and P, indicative of Mild combustion. The temperature difference in Case M reflects the "wishbone-shaped" similar to radial temperature distributions of the Case NP and P. The peak in the temperature difference of Case M is approximately 100 K at  $Z = 3$  mm. We observe that the combustion zone of Case M is relatively thick: the width at half maximum is approximately 4.5 mm while it is approximately 3 mm for the two other cases. The peaks in the temperature difference of Case NP and P are positioned near a radius of 5 mm. The vertical lines in Fig. 3.12, depict the radial location of the stoichiometric mixture fraction. The radial location of the stoichiometric lines corresponds well with the position of the maximum temperature differences in Case NP and P, while in Case M, it seems to be situated closer to the centerline than to the maximum temperature difference.

### 3.5.3 Analysis of flame structure in mixture fraction space

With an eye towards comparison of the combustion processes of the investigated flames, temperature and major species are plotted in mixture fraction space in

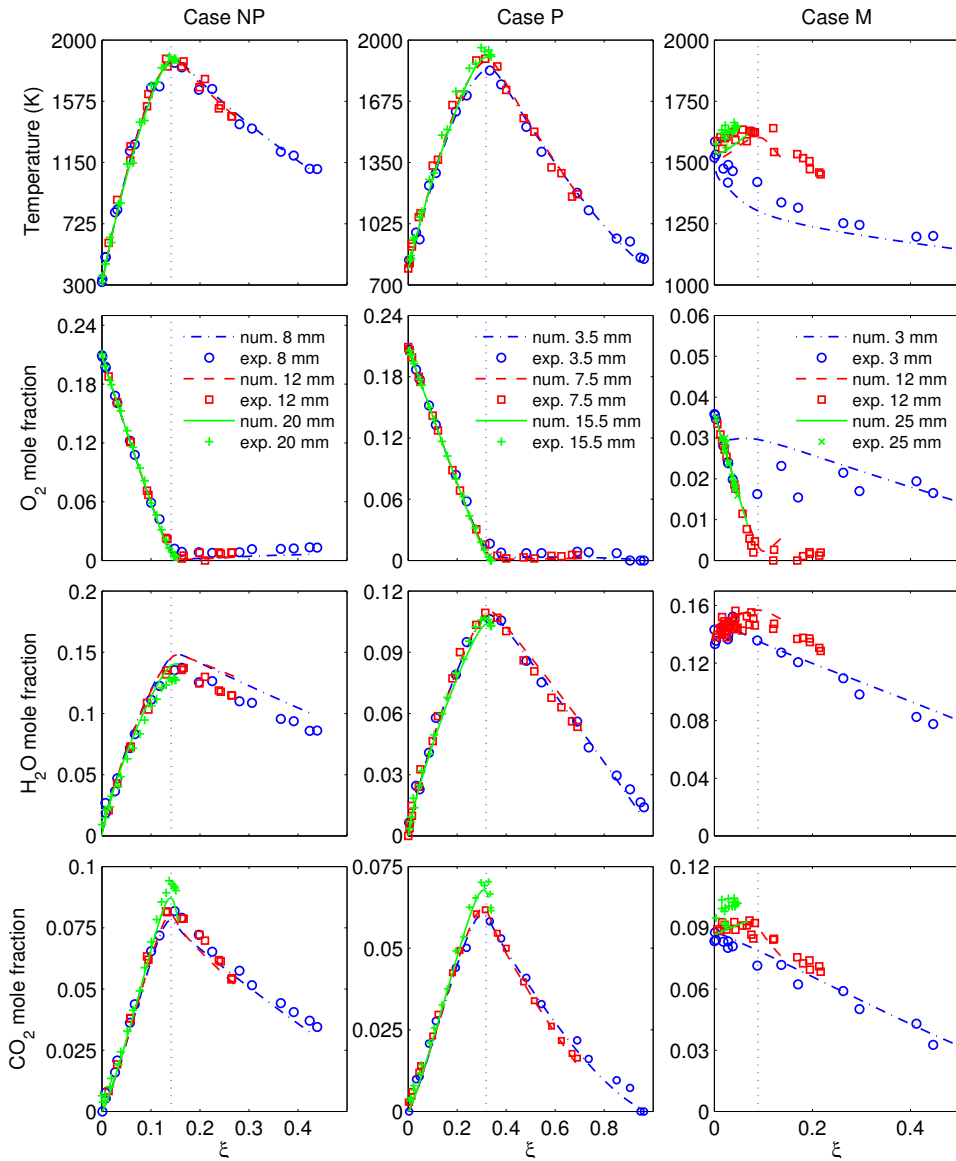


**Figure 3.13:** Comparison of (symbols) measured and (lines) computed temperatures and concentrations of  $O_2$ ,  $H_2O$  and  $CO_2$  at various heights of all three cases in mixture fraction space. Dotted lines are  $\zeta_{st}$  for each case.

Fig. 3.13. The mixture fraction was computed using Bilger's formula [Bilger, 1988]. This formula was modified to account for the presence of C and H in the oxidizer for Case M. It is seen that numerical computations in this space are also in a reasonable agreement with measurements for all studied cases. Moreover, both the computed

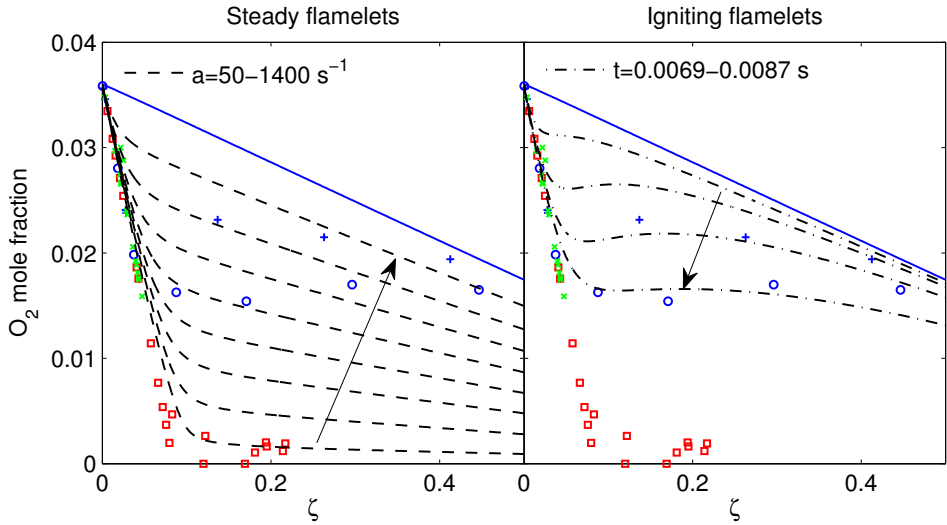


**Figure 3.14:** Comparison of (symbols) measurements and (lines) computed flamelets. Measurements (+) at  $Z = 3$  mm in left side of the centerline, (o) at  $Z = 3$  mm in right side of the centerline, (square) at  $Z = 12$  mm and ( $\times$ ) at  $Z = 25$  mm. (solid lines) Mixing solution. Left figure: (dashed lines) from bottom to top steady flamelets at strain rates  $a = 50, 200, 400, \dots, 1400 \text{ s}^{-1}$ . Right figure: (dashed dotted lines) from top to bottom unsteady igniting flamelets at times  $t = 0.0069, 0.0074, 0.0079, 0.0087 \text{ s}$  with  $a = 600 \text{ s}^{-1}$ .

and measured data at different heights are extremely well correlated and, within the uncertainty of the measurements, collapse on one line for Case NP and P. Such a correlation occurs for temperature,  $\text{O}_2$ ,  $\text{H}_2\text{O}$ ,  $\text{CO}_2$  and also for other measured species not shown in the figures. In Case M, correlation of the data is observed only at  $Z = 12$  and  $25$  mm. The temperature and  $\text{O}_2$  profiles at  $Z = 3$  mm, however, deviate significantly from those at downstream distances. It is noted that, as was discussed previously, the combustion process at this height is just initiated at the lean side of the mixture. At  $Z = 12$  mm the temperature and major species at lean and stoichiometric conditions are close to their chemical equilibrium values. The temperature difference between the distribution at  $Z = 3$  and  $12$  mm (which is larger than the reported measured temperature uncertainty) indicates incomplete combustion at  $Z = 3$  mm.

To further investigate the combustion process of Case M, we compare experiments with computations of steady and unsteady igniting counterflow diffusion flamelets. Computations of the flamelets are performed by stationary and time-dependent solution of the governing equations for 1D counterflow diffusion flames. Further details on the equations and solution procedure can be found in [Abtahizadeh et al., 2012]. These flamelets are obtained using the same temperature and composition of the 2D simulations for the fuel and oxidizer stream (according to Table. 3.1). Steady flamelets are computed with different strain rates from a relatively

low value  $a = 50 \text{ s}^{-1}$  up to the extinction limit approximately at  $a_{\text{ext}} = 1500 \text{ s}^{-1}$ . The results are shown in Fig. 3.14 for  $\text{O}_2$  because it shows the largest variations. Based on the results, distributions of Case M at  $Z = 12 \text{ mm}$  and  $Z = 25 \text{ mm}$  correspond very well with behavior of steady flamelets. However, this correspondence deteriorates at  $Z = 3 \text{ mm}$  and steady flamelets do not provide an accurate description of the experiments. In contrast, the profiles of an igniting flamelet at different times represent a much improved description of the flame structure at  $Z = 3 \text{ mm}$ . The asymmetric distribution in the experiments corresponds to a small time difference of the igniting flamelets. The igniting flamelet is obtained with  $a = 600 \text{ s}^{-1}$  which is in agreement with the scalar dissipation rate of the coflow flame at  $Z = 3 \text{ mm}$ .

Time scales of igniting flamelets in Fig. 3.14 is compared with those of the homogeneous reactor in Fig. 3.10 and the time-of-fly of a pocket of mixture in Fig. 3.8. The time-of-fly can be estimated by dividing the distance between the burner exit plane and the position of the maximum heat release at  $\zeta_{\text{MR}}$  by the velocity of the coflow. This gives a time-of-fly of 12 ms, which is almost two times the ignition delay at  $\zeta_{\text{MR}}$  for a homogeneous reactor. The longer delay in the non-premixed coflow flame can be attributed to scalar dissipation effects as described, for instance, by [Mastorakos \[2009\]](#). This effect can also be observed in the results of the igniting counterflow flamelets. It yields an ignition delay of approximately 10 ms which is in a good agreement with the time-of-fly.

The flamelet analyses indicates the autoignition structure of Mild combustion, in agreement with the previous conclusions from the heat release and  $\text{CH}_2\text{O}$  profiles in subsection 3.5.2. Such an observation also provides useful information for flamelet-based reduction techniques [[Peters, 1984](#); [van Oijen and de Goey, 2000](#)]. These techniques have been developed to decrease computational costs of reacting flow simulations by tabulation of chemistry instead of solving for all species. In this tabulation process, it is essential to adopt a suitable flamelet configuration. Based on these results, accurate predictions of Mild flames with autoignition structure can be obtained by application of igniting flamelets. Application of igniting flamelets for simulations of turbulent Mild flames is extensively discussed in Chapter 4. It is worth to emphasis that the observations in this study are one of a few combined experimental and numerical evidences about the autoignition structure of flames in the Mild combustion regime.

## 3.6 Analysis of NO formation

### 3.6.1 Rate-of-production analysis

Table 3.2 provides the data on contribution of thermal NO and prompt NO pathways to the total NO formation of studied flames. The data are represented using the integral reaction rates  $R_{\text{NO},i}$  (g/s):

$$R_{\text{NO},i} = 2\pi W_{\text{NO}} \int \int \dot{\omega}_i r dr dz \quad (3.12)$$

**Table 3.2:** Total rate of the NO formation.

	Case NP	Case P	Case M
$W_{\text{NO}} \int \omega_{\text{NO,Tot}} r dr dz$ (g/s)	$1.45 \times 10^{-6}$	$1.77 \times 10^{-6}$	$4.62 \times 10^{-8}$
$2W_{\text{NO}} \int \omega_{\text{NO,Zeld}} r dr dz$ (g/s)	$-1.28 \times 10^{-8}$	$2.48 \times 10^{-9}$	$2.70 \times 10^{-9}$
$2W_{\text{NO}} \int \omega_{\text{NO,Fen}} r dr dz$ (g/s)	$1.71 \times 10^{-6}$	$1.82 \times 10^{-6}$	$4.07 \times 10^{-8}$
EINO (g/kg)	1.25	2.17	$1.84 \times 10^{-1}$

where  $W_{\text{NO}}$  and  $\dot{\omega}_i$  are the NO's molecular weight and production rate ( $\text{kmole.m}^{-3}.\text{s}^{-1}$ ), respectively. The subscript  $i$  denotes to NO formation through the prompt path ( $i = \text{Fen}$ ) via (R240), thermal path ( $i = \text{Zeld}$ ) via the following reaction



and the total NO formation ( $i = \text{Tot}$ ). We assume that all nitrogen atoms bound in reactions (R178) and (R240) can be converted to NO. The total NO formation is also reported in the Table 3.2 in terms of emission index EINO defined as the amount of pollutant produced per unit of mass of fuel by the combustion process:

$$EINO(\text{g/kg}) = \frac{W_{\text{NO}} \int \int \dot{\omega}_{\text{NO,Tot}} r dr dz}{W_{\text{CH}_4} | \int \int \dot{\omega}_{\text{NO,Tot}} r dr dz |} \times 10^3 \quad (3.13)$$

The data presented in Table 3.2 show that the Fenimore NO formation is the dominant source of the NO production in all three flames. The data also reveal that in terms of emission index, the NO production in Case NP and P is approximately 7 and 11 times, respectively, larger than that in Case M.

It is worthwhile to note that the reaction (R240) has a substantial rate in reverse direction; approximately 35% of the forward rate for all diffusion flames studied. The same observation has been reported in [Sepman et al., 2011] where NO formation has been investigated in burner-stabilized premixed 1-D flames via the detailed chemical reaction mechanism of Qin et al. [2000]. This mechanism was extended with  $\text{N}_2$  chemistry from the GRI-Mech 3.0 mechanism with the same modifications of the NO chemistry as in this work. It was also demonstrated that the reaction reversed to reaction (R240) returns a considerable fraction of NCN back to  $\text{N}_2$ .

### 3.6.2 Vertical profiles

Computations and measurements of NO concentration have been performed for all three cases and it appeared that the NO formation of Case M is considerably lower than that of Case NP and P. Therefore, it is reasonable to discuss initially the NO formation in non-preheated and moderately preheated flames. Figure 3.15 shows computed and measured vertical profiles of (a) temperature and (b) NO mole fraction in Cases NP and P. It is observed that temperature increases to its peak value of approximately 1850 K, at distances of approximately 15 mm and 20 mm above the burner outlet for Case P and NP, respectively. The computations support the measurements quantitatively. Locations of the maximum heat release, as shown in



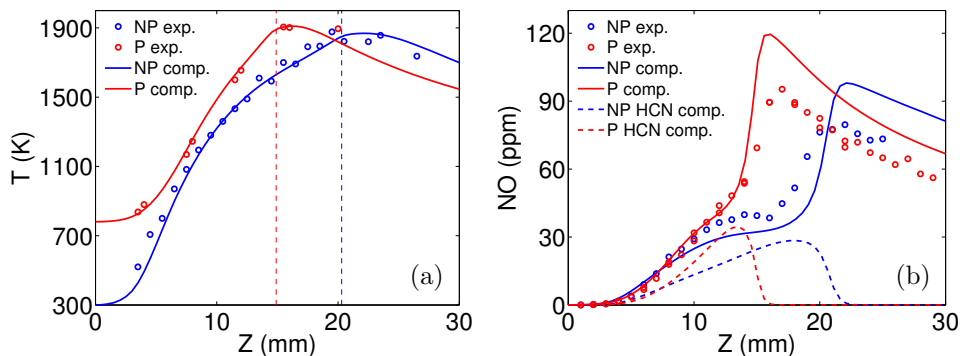


**Figure 3.15:** Comparison of (circles) measured and (lines) computed axial profiles of (a) temperature and (b) NO and HCN mole fractions for Case NP and P.

the figure with vertical lines, correspond to positions of peak temperature for each case. The mole fraction of NO for Case NP grows linearly in the range between 5 and 12 mm, up to the level of approximately 40 ppm, and then it remains almost constant over the next 4 or 5 mm. Between roughly 16 and 19 mm, the NO mole fraction rapidly grows almost doubling its concentration and further no significant variation is seen. The NO vertical profile of Case P demonstrates an identical behavior to that of Case NP up to a height of approximately 11-12 mm, after this height it continues to grow for a few millimeter distance more, up to the concentration level of approximately 55 ppm. The NO mole fraction increases then rapidly, in a way similar to that of Case NP, over the next 2 - 3 mm, up to the NO level of approximately 95 ppm. In the range between 17 and 29 mm, the NO mole fraction decreases gradually to approximately 55 ppm. We note that the position of the rapid increase in the NO concentration corresponds approximately to the location of flame front for both cases. The predicted NO mole fractions are in a very good agreement with the experimental results. This agreement is quantitative for Case P. While the computational profile matches the measured NO mole fraction qualitative very good for Case NP, it (at least the part of the profile around the rapid NO rise) seems to be shifted downstream for approximately 2 mm. When corrected for this shift, the agreement between measurements and computations becomes almost quantitative. It is interesting to note that the computed rapid increase in Case NP (approximately 60 ppm) is somewhat larger than the experimental one (approximately 40 ppm). Here, it is worth to mention that the axial measured temperature and/or major species concentrations are not the first choice for accurate determination of the flame front position due to their relatively small gradient near the flame front. It is also worthwhile to point out that the NO mole fraction profile in Fig. 3.15 indicates a steeper gradient close to flame front than the temperature profile does.

The excellent agreement between computations and experiments engenders confidence in the predictive power of currently used chemical mechanism and encourages us to analyze NO formation from a mechanistic point of view. As it is observed earlier, the Fenimore NO formation is a dominant source of NO production in all three

flames. The rate-of-production analysis also reveals that the rate of chemical NO production along the centerline is positive only at the flame front location in both cases. From above, it follows that the buildup of the centerline NO concentration before the flame front has a non-chemical character and is a result of (radial) diffusion. Calculations show that there are considerable concentrations of the intermediate nitrogen bound species (such as HCN, HNCO and  $\text{NH}_3$ ) upstream of the flame front, see Fig. 3.15b, as a result of (radial) diffusion. It is interesting to note that the centerline flame front NO formation mainly comes from the conversion of these diffused species to NO, rather than those formed by the  $\text{CH} + \text{N}_2$  reaction, which, as the calculation shows, is below approximately 10 ppm in both cases. The gradual NO reduction downstream of the flame front is due to the mixing with the coflow.

Additionally we have performed the flame calculation for Case NP using the GRI-Mech 2.11 chemical mechanism, which, as was noticed in some works concerned with diffusion flames (cf. [Smooke et al., 1996]), predicts reasonably well the NO formation. Additional computations showed, however, that the GRI-Mech 2.11 is unsuccessful in reproducing both the axial flame temperature and NO mole fraction profiles accurately.

### 3.6.3 Radial profiles

Figure 3.16 shows radial distribution of the NO mole fraction computed and measured for Case NP and P. To illustrate the development of NO formation progressively downstream, the radial profiles are shown at axial positions of 4.5, 12 and 20 mm for Case NP (Figs. 3.16a-c) and 3.5, 7.5 and 15.5 mm for Case P (Figs. 3.16d-f). The development of NO profiles for both cases reflects "wishbone-shape" and mirrors the changes observed in the corresponding temperature profiles in the previous section. Turning at first to Case NP, we see that at 4.5 mm above the fuel tube exit (Fig. 3.16a), the NO mole fraction peaks to the level of approximately 35 ppm at 5 mm (outer radius of the fuel tube). We note that this location corresponds to the location of maximum heat release. The NO concentration decreases rapidly in the inner and outer sides of the jet suggesting mixing of the NO formed in the flame front with the fuel-rich and fuel-lean mixtures, respectively. At 12 mm above the fuel tube exit, the NO mole fraction reaches the level of approximately 75 ppm at a radial distance. The centerline NO mole fraction is on the level of approximately 35 ppm. We note that the peak NO mole fraction at this axial distance is at the level of the maximum centerline NO concentration, see Fig. 3.15b. At higher axial distances, the peak NO concentration does not change significantly, while its location shifts gradually to the fuel-rich side (not-shown). At 20 mm heights, the NO radial profile becomes a bell-shaped form with the flat top stretching over approximately 5 mm distance, see Fig. 3.16c. The radial NO profiles for Case P demonstrate a similar development of the structure, with two worth-mentioning differences. Namely, first, the maximum peak NO concentration is on the order of approximately 100 ppm and, second, the bell-shaped form is attained at an axial distance of approximately 16 mm.

Figures 3.16a and d also shows filtered computed NO mole fraction with the width of 1.5 mm (solid lines) which is plotted together with the unfiltered numerical

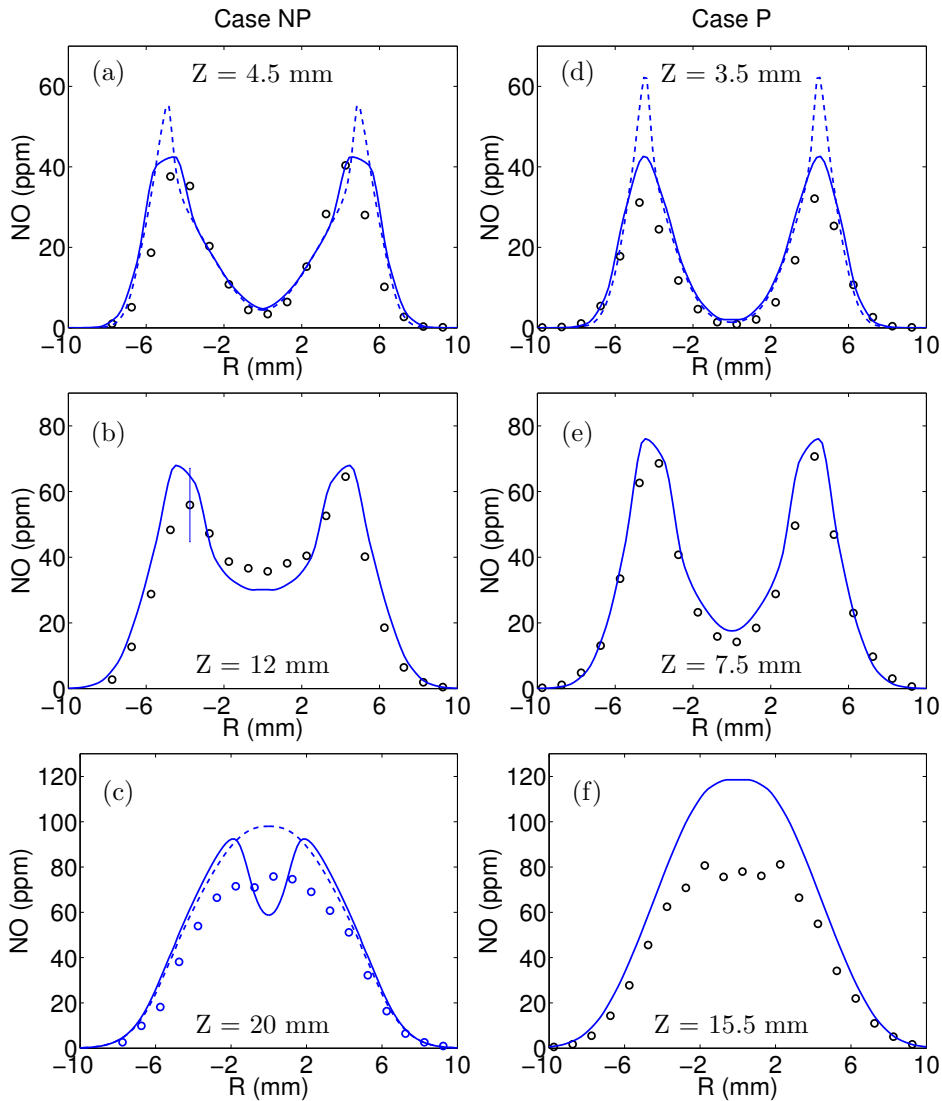


**Figure 3.16:** Comparison of (circles) measured and (lines) computed radial NO mole fractions at different axial distances for (a-c) Case NP and (d-f) Case P.

profile (dashed lines). The filtering was performed to yield a representative comparison of predictions and measurements considering the fact that the measurements were made with a resolution of approximately 1.5 mm. The effect of the filtering leads to a smoothing of the sharp NO peaks in such a way that the maximum NO concentration is reduced by approximately 20%. The broadening of the NO radial structure with axial distance diminishes the difference between the filtered and unfiltered profiles. The comparison of the experimental and filtered computational

profiles reveals a very good agreement. The agreement between the measured and computed profiles for Case NP is quantitative at 4.5 mm. At 12 mm, it is quantitative at the location of the NO peaks and at the outer sides of the jet, however, at the inner side of the jet, it is slightly underpredicted. We note that the divergence in shapes of the measured and computed profiles at 20 mm is due to small difference in the positions of the measured and computed centerline peak NO, see Fig. 3.15b. Figure 3.16c also includes the computations at 22 mm (dashed line). There is very good quantitative and qualitative agreement between this computed profile and the experimental distribution; the flat top experimental NO concentration is overpredicted by approximately 20%, which is the uncertainty in the NO measurements. Turning to the measured and computed profiles in Case P (Figs. 3.15d-f), we see an excellent agreement between them. The small quantitative difference between the experimental and computed profiles at 15.5 mm (Fig. 3.16f) is again due to the small difference in the positions of the measured and computed centerline peak NO (see Fig. 3.15b).

Here, we would like to note that the NO profiles shown in the Figs. 3.15c and f can be used for indication of the total NO formed in the flames studied. At these distances, as computations reveal, there are no CH radicals left (required for initiation of the Fenimore NO production) at any significant level and all intermediate nitrogen bound species are converted to (mainly) NO. Figures 3.15 and 3.16 show that the measured NO mole fractions at these distances are systematically lower than the predictions, although the difference is within the measurement uncertainty meaning that the currently used NO mechanism predicts adequately the total NO formed in the flames. Furthermore, it is interesting to mention that the maximum measured NO mole fraction is systematically lower than the predictions at downstream distances for both cases considered, but is very good matched or even underpredicted at the upstream distances (with the exception of the measurements made close to the burner outlet). Such a behavior might be caused by some underprediction in the burnout rate of the intermediate nitrogen bound species in and near the flame front. This suggestion is in accordance with one of the observations reported in [Sepman et al.2, 2011], where it was shown that at the temperatures relevant for the flames studied here, the HCN burnout is slightly underpredicted by the currently used NO formation mechanism.

We think that it is appropriate at this point of the discussion to illustrate the redistribution of nitrogen atoms over N-containing components. To do so, Fig. 3.17 presents the radial distribution of the total chemical production rates of most important N-containing species NO, HCN, NH<sub>3</sub>, N<sub>2</sub>, HNCO and NNH at the height of 8 mm for Case NP. To account for the presence of the two N-atoms in the N<sub>2</sub> and NNH compounds, the total N<sub>2</sub> and NNH rates are multiplied by a factor of 2. The positive value of the reaction rate means production while negative represents consumption. Rates at a radial distance sum up almost to zero. For convenience of the reader, the figure includes only the data for species whose absolute reaction rate is above the value of  $0.5 \times 10^{-4}$  mole.m<sup>-3</sup>.s<sup>-1</sup>. The vertical line marks the position of stoichiometric mixture fraction. First of all, we note that the total NO profile displays both positive and negative values situated almost inversely symmetrical with respect to the point where the NO production rate crosses the *R*-axis (at approxi-

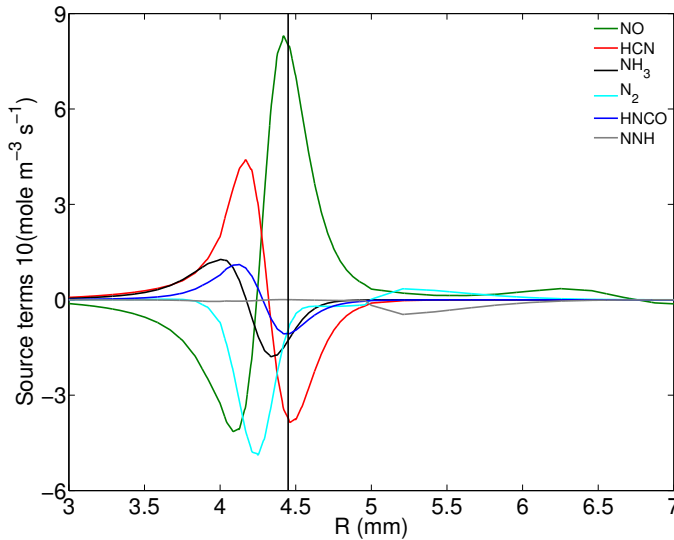


**Figure 3.17:** Radial distribution of the total chemical source terms of most important N-containing species at 8 mm height for Case NP. To account for the presence of the two N-atoms in the  $N_2$  and NNH compounds, the total  $N_2$  and NNH rates are multiplied by a factor of 2.

mately 4.2 mm). Being at the zero level in the region between 0 and 3 mm, the NO reaction rate decreases then rapidly and reaches the minimum at  $R$  approximately 4 mm (fuel rich conditions). Having reached the minimum, the NO profile increases fast to obtain the maximum value at the stoichiometric mixture fraction and then decreases relatively fast approaching the zero production level. The  $N_2$  reaction rate profile is almost identical to that of the  $CH + N_2$  reaction rate (not shown), with an exception of the fuel-lean region, where the total  $N_2$  rate is positive, we will return to this observation below. The profiles of the HCN,  $NH_3$  and HNCO production rates resemble closely the mirror image of the NO production curve about the  $R$ -axis. Their maximum are located near the position of the maximum NO consumption, while minimum near the position of the maximum NO production. From the figure, it is clear that the NO formation at practically all radial distances occurs mainly due to the oxidation of the N-containing intermediates (HCN,  $NH_3$ , HNCO). The contribution of the rate of the  $CH + N_2$  reaction to the rate of NO production gains importance near the location of the zero NO production. The figure also shows that the NO consumption is a result of the conversion of the NO molecules to the N-containing intermediates (similarly as described in [Dagaut et al., 2000]) rather than to  $N_2$ . The rate-of-production analysis shows that the reactions that initiate conversion of NO to these intermediates involve various hydrocarbon radicals, such as  $CH_2$ , HCCO, CH,  $CH_3$ . The N-containing product of the  $CH + N_2$  reaction (NCN) is also converted to these intermediates at such fuel-rich conditions. The actual conversion of N-containing species to  $N_2$  does occur only at the fuel-lean side

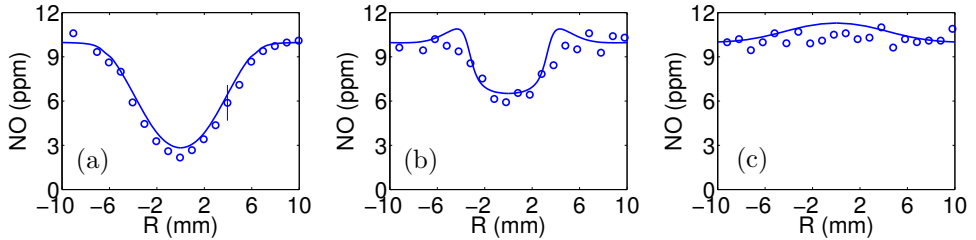


**Figure 3.18:** Comparison of (symbols) measured and (lines) computed radial profiles of NO mole fraction for Case M at (a)  $Z = 3$  mm, (b)  $Z = 12$  mm and (c)  $Z = 25$  mm.

via the NNH mechanism. However, the total rate of  $N_2$  production is quite small. The modest positive rate of NO formation in this region is due to  $NO_2$  conversion (not shown in the figure). The general features of the nitrogen atom flux are valid for most of the other axial positions and is also representative for Case P.

### 3.6.4 NO formation and consumption

Figure 3.18 compares the experimental and computational profiles of the NO mole fractions of Case M at axial positions of 3, 12 and 25 mm. We observe that at a height of 3 mm the measured NO mole fraction decreases gradually with radial distance, from approximately 10 ppm at the edges of the measurement domain (the coflow contains 10 ppm of NO, see Table 3.1) decreasing to approximately 1 ppm at the centerline. By moving downstream, this "hole" in the NO fraction in the region of the fuel flow decreases, until the profile is flat at 25 mm. Comparison with the computed profiles shows an excellent agreement. It is useful at this point to move the discussion on the NO formation to mixture fraction space where we can decouple the effects of mixing of NO present in the oxidizer stream from the contribution of the combustion of fuel. Figure 3.19 shows the experimental and computational results as a function of mixture fraction. The mixture fraction was computed using Bilger's formula [Bilger, 1988]. This formula was modified to account for the presence of C and H in the oxidizer. Also plotted is the curve that results from simple mixing of the hot coflow with the combustion products of the fuel jet,  $Y_{NO} = (1 - \zeta)Y_{NO,ox}W_M/W_{ox}$ , where  $\zeta$  is the mixture fraction,  $Y_{NO,ox}$  is NO fraction in the oxidizer (10 ppm) and  $W_M$  and  $W_{ox}$  are molecular weights of combustion products in the measuring position and oxidizer, respectively.

According to experimental data, no substantial NO is formed under these Mild conditions. The measurements cluster at lean and slightly fuel-rich conditions around the mixing curve and are just below it (the difference is of the order of experimental uncertainty) at the richer side. Computations, also tend to follow the mixing line and additionally allow us to distinguish fine details of NO production. First of all, computations display the effects of both the NO formation and NO consumption in Case M, see Fig. 3.19. The computational profiles at 3 and 25 mm heights are situated below (consumption) and above (formation) the mixing line,

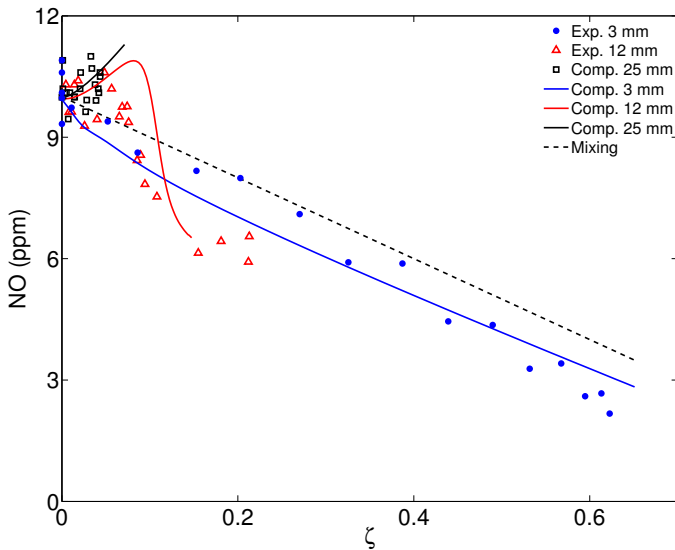


**Figure 3.19:** The (symbols) measured and (lines) computed NO mole fractions versus mixture fraction for Case M.

respectively. The profile at 12 mm displays the effect of NO formation from lean to slightly rich conditions, while further at rich side it demonstrates the effect of NO consumption. The NO formation (the profiles at heights of 12 mm and 25 mm), as was already discussed above, is the result of the Fenimore NO production. The rate-of-production analysis reveals that the consumption (the profiles at heights of 3 mm and 12 mm) is due to the conversion of the NO molecules to the N-containing intermediates rather than  $N_2$ . It is interesting to mention that the NO conversion is mechanistically different at the different flame locations. Close to the burner outlet, the NO is converted to  $NO_2$  (the concentration of NO and  $NO_2$  sums up to the corresponding NO mixing value at the height of 3 mm). Further downstream, the increase of hydrogen atom concentrations leads to conversion of  $NO_2$  back to NO through reaction  $NO_2 + H \leftrightarrow NO + OH$ . At heights above 3 mm, the NO conversion occurs to mainly HCN,  $NH_3$  and HNCO. We note that the major qualitative features of the redistribution of nitrogen atoms over N-containing components at these distances in Case M are quite similar to that shown in Fig. 3.17 for Case NP. At 25 mm, all formed N-containing intermediates are already converted back to NO.

The analysis of the experimental and computational data in the mixture fraction space indicates that the NO field is dominated by mixing of the NO formed in the coflow with the reaction products of the diluted fuel, with negligible NO formation from the fuel. At the given level of the NO seeding, the effects of the NO formation and consumption (conversion to other N-containing intermediates) display itself (as computations reveal) on the same order of magnitude scale. The small level of these effects, however, prevents their unambiguous experimental observation. In an attempt to shed a further light on the processes of the inter-conversion of the N-

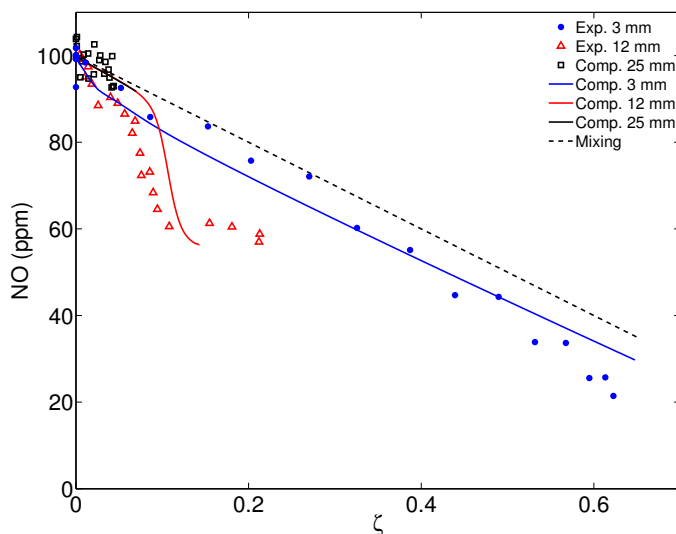


**Figure 3.20:** The (symbols) measured and (lines) computed NO mole fractions versus mixture fraction for Case M\_NO.

**Table 3.3:** Boundary conditions.

Case	Coflow							Fuel				$\zeta_{st}$	
	$V(\text{m/s})^a$	$T(\text{K})^b$	$X_{\text{O}_2}$	$X_{\text{N}_2}$	$X_{\text{H}_2\text{O}}$	$X_{\text{CO}_2}$	NO(ppm)	$V(\text{m/s})^a$	$T(\text{K})^b$	$X_{\text{CH}_4}$	$X_{\text{H}_2}$		$X_{\text{N}_2}$
Case M_NO	0.155	1530	0.036	0.732	0.145	0.087	100	0.058	1150	0.170	0	0.830	0.08917
Case M_H <sub>2</sub>	0.155	1530	0.036	0.732	0.145	0.087	10	0.058	1185	0.09	0.09	0.830	0.1228

<sup>a</sup> Mean exit velocities at standard condition ( $T = 273 \text{ K}$ ,  $P = 1013255 \text{ Pa}$ ).

<sup>b</sup> Mean temperatures at 3 mm above the exit plane.

containing species under the Mild conditions, a new case has been tested by addition of 100 ppm of NO mole fraction to the oxidizer coflow, Case M\_NO, see Table 3.3.

Figure 3.20 displays the NO measured and computed for Case M\_NO as a function of the mixture fraction. As can be seen from the figure, seeding of the larger NO amount reduces the scatter in the experimental data. The general behavior of the experimental data for Case M\_NO is similar to that of Case M, with the exception of the data at 12 mm. The comparison of the computed and measured NO mole fractions at 12 mm with the mixing line demonstrates a noticeable NO consumption at the fuel rich conditions, the difference is on the level approximately 30 % (in Case M approximately 20 %); the data at the fuel lean side are also systematically below the mixing line, although the difference is within the accuracy of the measurements. The computational data are in an excellent agreement with the measurements which support the observed differences in the behavior of the measured profiles at 12 mm. We note that the computed concentrations of NO and N-containing species like (HCN, NH<sub>3</sub> and HCNO) at the height of 12 mm height sum up to the corresponding NO mixing value.



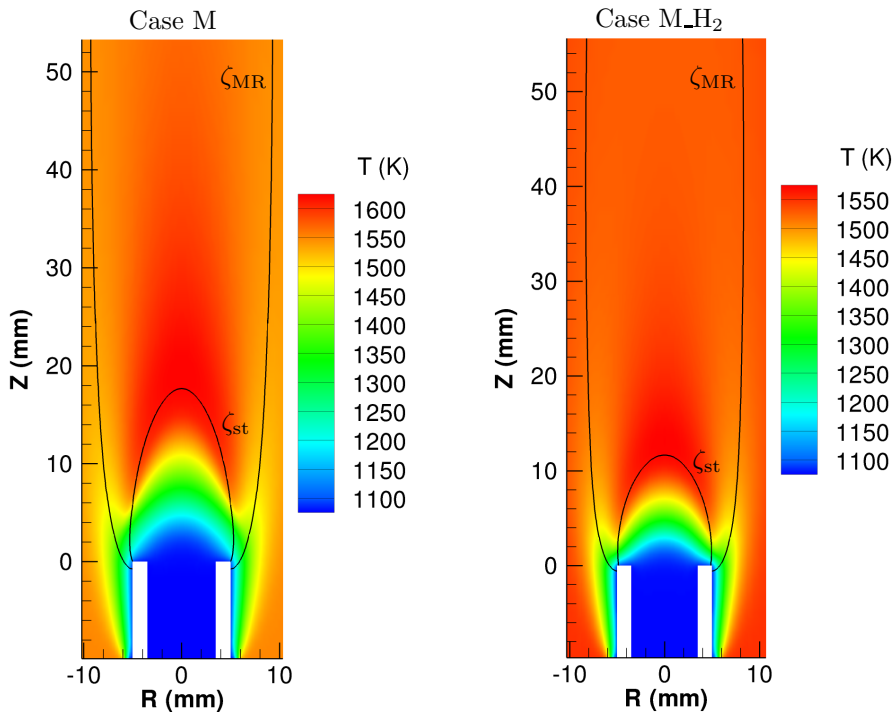


**Figure 3.21:** Two-dimensional false color plots of the computed temperature for Case M and M\_H<sub>2</sub>. The black lines show iso-contours of stoichiometric mixture fraction  $\zeta_{st}$  and most reactive mixture fraction  $\zeta_{MR}$ .

## 3.7 Addition of Hydrogen

### 3.7.1 General structure of flames

To illustrate effect of hydrogen addition on the overall flame structure, a new case, Case M\_H<sub>2</sub>, is studied which is shown in Table 3.3. Figure 3.21 presents two-dimensional false color plots of the computed distribution of temperature for flames with and without hydrogen addition. The figure includes the stoichiometric and most reactive mixture fraction iso-contours. First of all, we note that the hydrogen addition does not affect the general flame appearance significantly. Indeed the extent of high temperature zone of two flames is comparable and maximum temperatures are rather similar, being approximately 50 K higher in Case M. However, the addition does appreciably influence the position of the temperature rise with respect to the location of the burner outlet. The significant temperature rise of Case M is evident at a height of approximately 6 mm, while that of Case M\_H<sub>2</sub> is visible at a height of approximately 3 mm. Such a behavior indicates that the hydrogen addition promotes ignition. We also note that the hydrogen addition decreases sig-

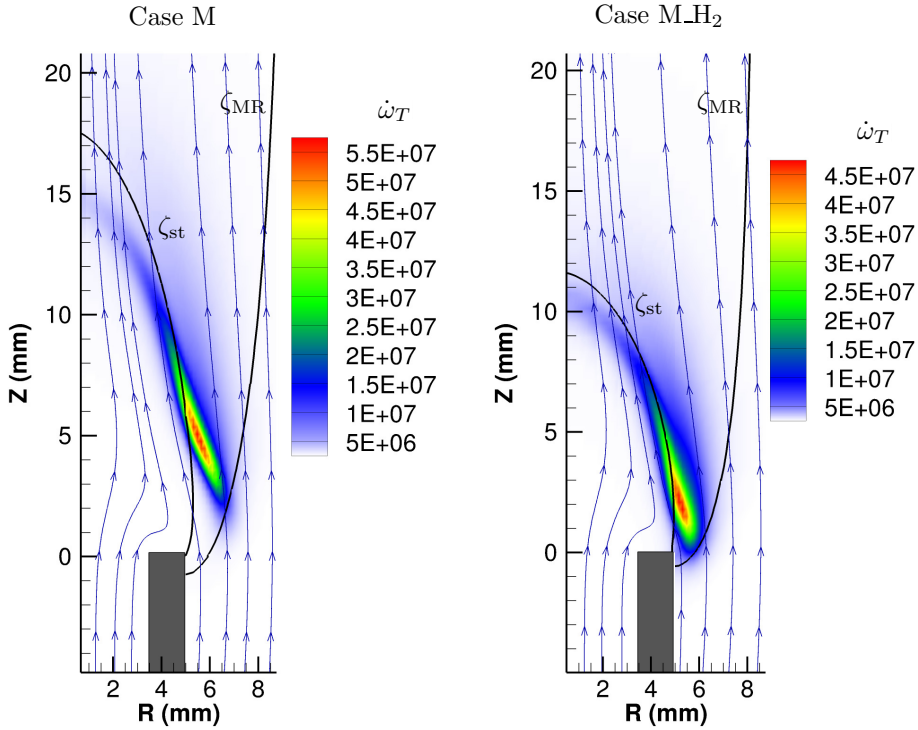


**Figure 3.22:** Two-dimensional false color plots of the computed heat release  $\dot{\omega}_T$  ( $W/m^3$ ) for Case M and M\_H<sub>2</sub>. The lines with arrows represent streamlines of the velocity field. The black lines show iso-contours of stoichiometric mixture fraction  $\zeta_{st}$  and most reactive mixture fraction  $\zeta_{MR}$ .

nificantly the axial location of the stoichiometric contour from approximately 18 mm to 12 mm at the centerline. The above comments are further illustrated by the simulated heat release rate distributions shown in Fig. 3.22 together with streamlines and the iso-contours. As can be seen from Figs. 3.21 and 3.22, the location of maximum temperature at every height corresponds to the position of the maximum heat release. Figure 3.22 also shows that in both cases, the combustion starts at a lean mixture fraction, proceeds further downstream towards and beyond the stoichiometric mixture fraction. We further note that the both heat release profiles are notably different from those of coflow diffusion edge flames. This is due to the fact that the flame temperature in the studied cases is not large enough to support an edge flame that can propagate upstream. Therefore, it can be concluded that stabilization mechanism of these cases is governed by autoignition.

The autoignition structure of Case M and M\_H<sub>2</sub> is further analyzed by plotting the computed distributions of the production rate of formaldehyde in Fig. 3.23. It is clear that for both flames CH<sub>2</sub>O is formed upstream of the maximum heat release location, immediately above the burner tip. The produced CH<sub>2</sub>O is then consumed

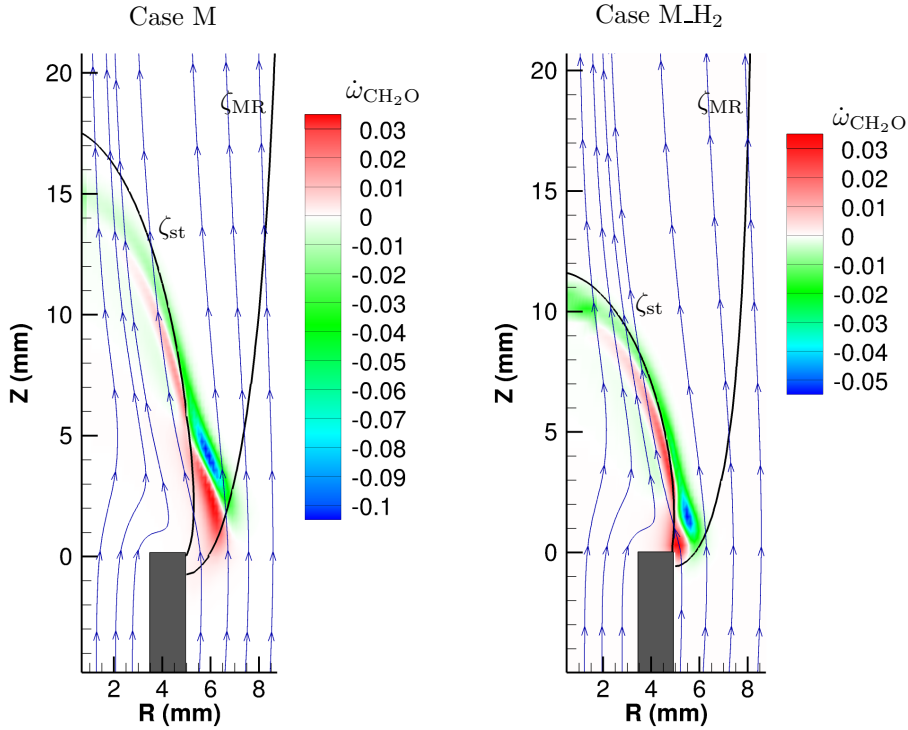


**Figure 3.23:** Two-dimensional false color plots of the computed formaldehyde  $\dot{\omega}_{CH_2O}$  ( $\text{kmol}/\text{m}^3\text{s}$ ) for Case M and M- $\text{H}_2$ . The lines with arrows represent streamlines of the velocity field. The black lines show iso-contours of stoichiometric mixture fraction  $\zeta_{st}$  and most reactive mixture fraction  $\zeta_{MR}$ .

at the maximum heat release location. We note that such a behavior is in a clear contrast with the trends that have been observed for the edge flames in the subsection 3.5.2, where  $\text{CH}_2\text{O}$  is formed downstream of the maximum heat release and it is diffused upwards towards the maximum heat release location where it is consumed. This again demonstrates the stabilization of these flames by autoignition. The location of the heat release and  $\text{CH}_2\text{O}$  production rate can be discussed in terms of most reactive mixture fraction  $\zeta_{MR}$ . This value has been obtained from the computations of a homogeneous reactor for various frozen mixtures of fuel and oxidizer in a 1D configuration for Case M and M- $\text{H}_2$ . It is observed that ignition starts from  $\zeta_{MR}$  similar to what has been reported for the autoignition structures [Abtahizadeh et al., 2012; Mastorakos, 2009; Sorrentino et al., 2013]. The  $\zeta_{MR}$  is located at the lean side due to the higher temperature and availability of a small amount of  $\text{O}_2$  at the coflow side.

Figures 3.21, 3.22 and 3.23 also display the increased diffusivity of the mixture due to hydrogen addition. Indeed, since the methane and hydrogen were mixed while keeping the total flow rate of the fuel constant, the global equivalence ratio

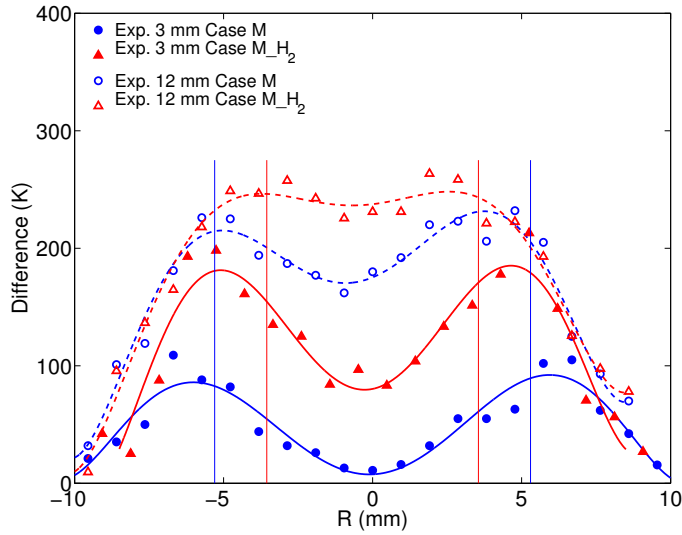


**Figure 3.24:** The differences between the radial temperature profiles at 3 and 12 mm with those measured when only  $N_2$  was flowing through the fuel tube. High-order polynomial trend lines are added to accentuate the trends in the experimental data. The vertical line marks the position of stoichiometric mixture fraction for each case.

has decreased by the hydrogen addition. However, the position of the stoichiometric mixture fraction contour near the burner outlet is practically not affected by the hydrogen addition.

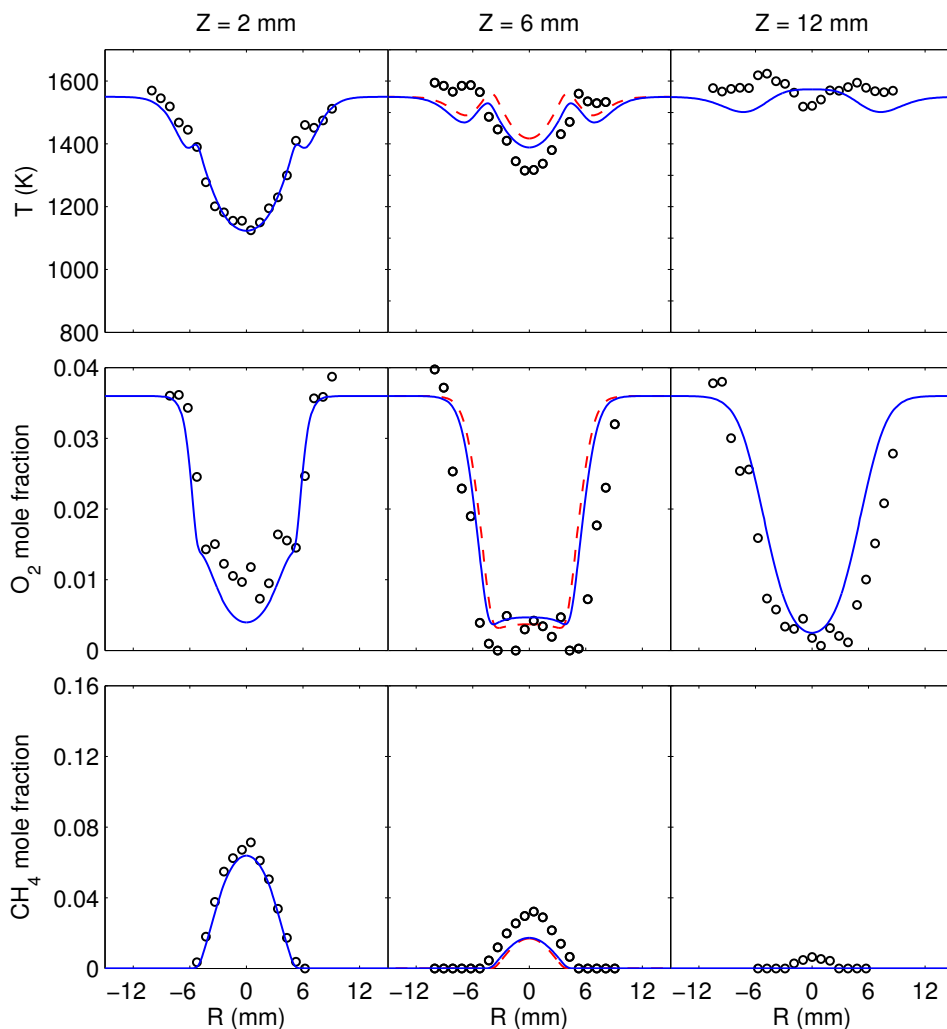
An important aspect of Case M- $H_2$  compared to Case M is the flame stability which is significantly improved by  $H_2$  enrichment. In fact, autoignition of these flames is initiated at low mixture fractions ( $< 0.13$ ) close to the coflow stream in localized regions of low scalar dissipation rate. Preferential diffusion of  $H_2$  leads to an increased presence of fuel at this most reactive mixture fraction [van Oijen, 2013] and eventually an increased chemical reactivity and stability of the flame. This observation corresponds very well with recent measurements of the turbulent Jet-in-Hot Coflow burner of TU Delft [Arteaga et al., 2013]. In these measurements, they added a range 5% - 25% hydrogen to the lifted Mild flames and they observed a significant improvement in stability together with a shorter lift-off height. Also the works of the Adelaide group [Medwell and Dally, 2012] confirm that the flame stabilization in Mild combustion is very similar for different fuels (NG,  $C_2H_4$  and LPG) with  $H_2$  enrichment. Such an improvement in the flame stability induced by the presence of hydrogen suggests a more flexible range of possible fuels for application in Mild combustors.

To supplement the computational findings about the effect of the  $H_2$  addition on the flame structure, the radial profiles of temperature is compared with measured values at 3 and 12 mm above the burner outlet for the two cases in Fig. 3.24. To illustrate the development of the flames, we plot the difference between the radial profiles measured in flames with those measured when only  $N_2$  was flowing

through the fuel tube. The situation when only  $N_2$  is present in the fuel tube corresponds to frozen (no chemical activity) mixing between coflow and fuel. The development in the profiles of the temperature difference for both flames reflect the “wishbone-shape” of radial temperature distributions in an “ordinary” diffusion flame, see Fig. 3.7, with the exception that the temperature rise in non-diluted coflow is approximately a factor of 9 higher than that shown in Fig. 3.24. The figure shows that at 3 mm height, the peak of the temperature difference in Case M is approximately 100 K, while that of Case M\_H<sub>2</sub> is approximately 200 K. The experimental data at 3 mm height show the presence of a noteworthy measured amount of  $O_2$  near the centerline in Case M, see Fig. 3.6, while for Case M\_H<sub>2</sub> the  $O_2$  mole fraction is close to zero (not shown), similar to the data at 2 mm (see Fig. 3.25). The analysis of the data measured in the vicinity of the burner outlet indicates that the hydrogen addition promotes the ignition. We would like also to mention that the radial profiles of the temperature difference for Case M measured at several downstream distances, (see Fig. 3.24 and [Sepman et al.2, 2013]) show the peak in the temperature difference on the level of 200 K. This value is similar to that of Case M\_H<sub>2</sub>. The figure also shows that the position of the maximum heat release shifts notably towards the burner outlet with the addition of hydrogen. We would like to note that some of the described above effects of the hydrogen addition on general flame structure such as reduction of the flame height and the shift of the reaction zone towards the burner exit were also reported in [Parente et al., 2008].

### 3.7.2 Radial and centerline profiles

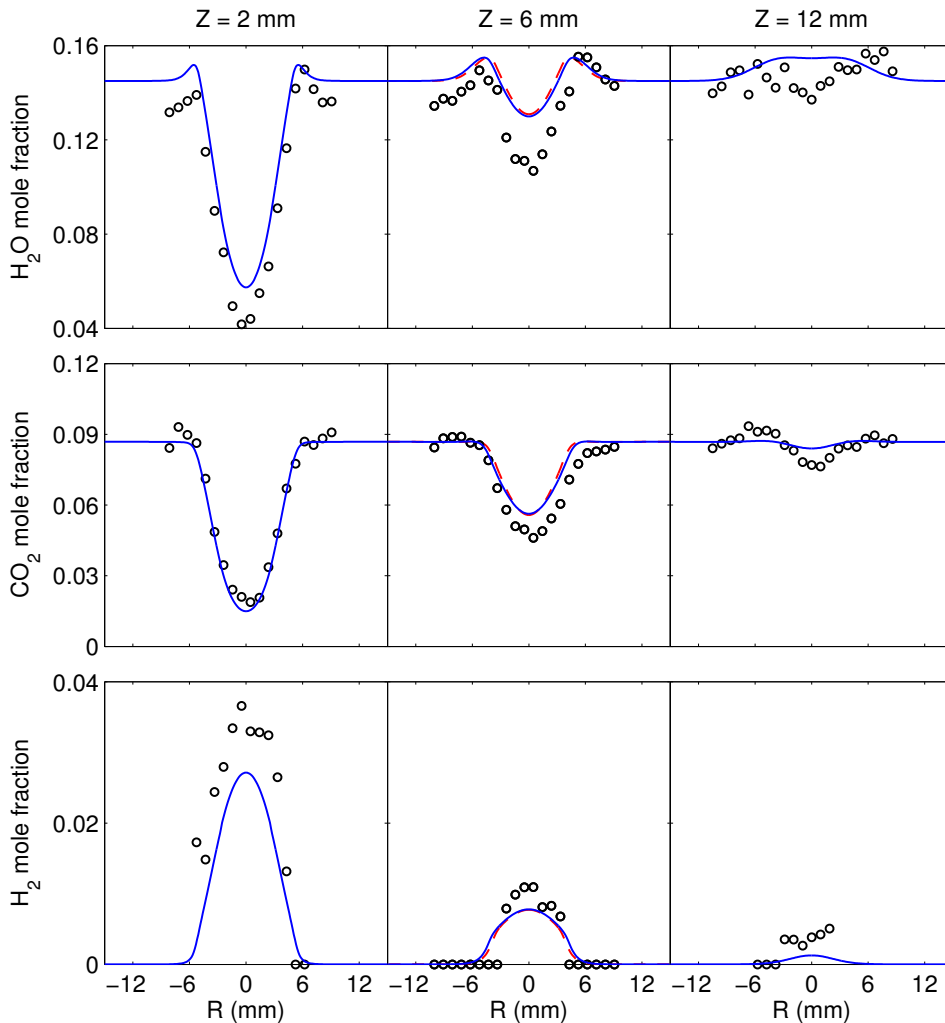
Figure 3.25 shows radial profiles of computed and measured temperature and major species mole fractions at the axial distances 2, 6 and 12 mm for Case M\_H<sub>2</sub>. To test the predictive power of the GRI-Mech 3.0 mechanism at the specific experimental conditions, computations have been contrasted against measurements. The progress of combustion in Case M\_H<sub>2</sub> is reflected in the development of temperature. However, details of the evolution are considerably masked by the large temperature difference between the coflow and fuel similar to the Mild flame without hydrogen addition (Case M). Development of major species for Case M\_H<sub>2</sub> is consistent with temperature changes. Computational and experimental temperatures agree quantitatively at the axial distance of 2 mm. We note that the little bump in the experimental temperature profile (marking apparently location of the combustion zone) at the radial distance of approximately 5 mm is well captured. At the axial distances of 6 and 12 mm, as the agreement is also good, computations predict the measured data within 120 K and generally better. The computations predict rather well  $H_2$  profiles and somewhat overpredict the  $CH_4$  consumption. The  $O_2$  profile is quantitatively predicted at the height of 2 mm. We noted already the presence of significant amount of  $O_2$  near the centerline. Further downstream, however, decrease of experimental  $O_2$  fraction at the edges of the measured domain occurs notably closer (approximately 1.5 mm) to the coflow side than that in computations. Such a behavior implies that the computational combustion zone is shifted closer to the fuel side in comparison with the experimental one. The overprediction of  $CO_2$  and  $H_2O$  profiles inside the domain of the fuel flow for some axial distances is consistent



**Figure 3.25:** Comparison of (circles) measured and (lines) computed radial profiles of temperature and major species of Case M<sub>H<sub>2</sub></sub> at three different heights and (dashed lines) with a reduced thermal boundary layer.

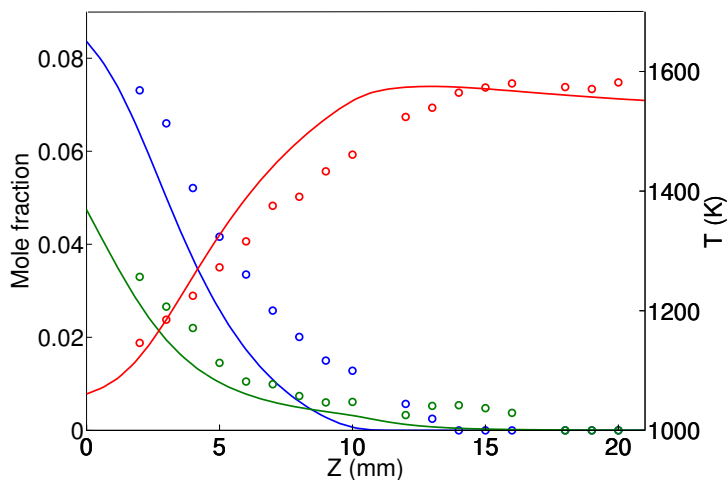
with this shift.

Figure 3.26 shows the computed and measured vertical profiles of T, CH<sub>4</sub> and H<sub>2</sub> mole fractions. The experimental temperature rapidly increases to the maximum temperature of approximately 1580 K, at the distance of approximately 15 mm above the burner outlet. The computations support the maximum measured temperature quantitatively, however, approach it faster and reach the maximum already at a distance of approximately 12 mm. In accordance with the observed difference in the behavior of the temperature profiles, the computations and mea-



**Figure 3.25:** Continued from the previous page.

measurements show similar discrepancy in the fuel profiles. While the experimental data demonstrate the non-negligible  $\text{CH}_4$  and  $\text{H}_2$  mole fractions at distances above 12 mm, the computations show that all fuel is consumed by a height of 12 mm. The rapid initial decrease in the vertical  $\text{CH}_4$  and  $\text{H}_2$  profiles is a result of the diffusion of fuel in radial directions towards the flame front. We would like to point out to an interesting feature related to behavior of the vertical  $\text{CH}_4$  and  $\text{H}_2$  profiles in the vicinity of the maximum heat release which is qualitatively well captured also by the computations. The  $\text{CH}_4$  concentration is consumed rapidly in the fuel-rich part of the flame front (see also Fig. 3.27), while most of the  $\text{H}_2$  concentration survives this region; the hydrogen burns out completely further downstream at the stoichio-



**Figure 3.26:** The (circles) experimental and (lines) computed vertical profiles of (red) temperature, (blue)  $\text{CH}_4$  and (green)  $\text{H}_2$  mole fractions for Case  $\text{M-H}_2$ .

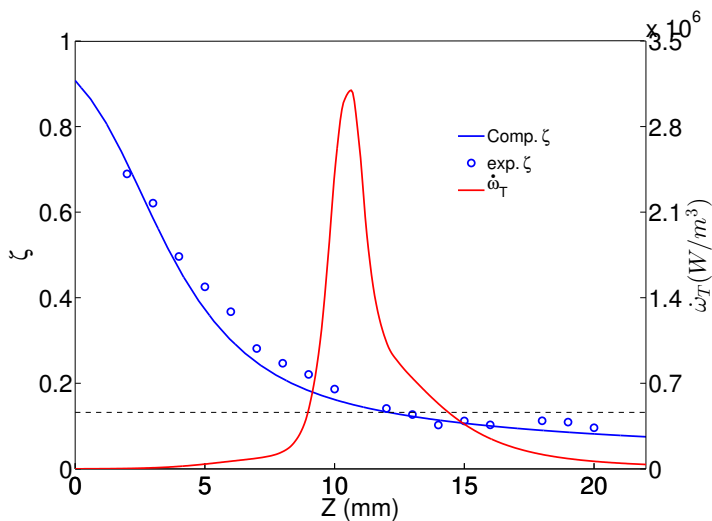


**Figure 3.27:** The vertical profiles of mixture fraction  $\zeta$  and heat release  $\dot{\omega}_T$  for Case  $\text{M-H}_2$  (symbols: measurements, lines: computations). The horizontal line marks the position of stoichiometric mixture fraction.

metric and fuel lean conditions. This behavior is perhaps not unexpected; the one dimensional flame computations of the  $\text{CH}_4/\text{H}_2$  blends demonstrate that a significant part of the hydrogen is not consumed at fuel-rich conditions. Figure 3.27 shows the vertical profiles of heat release and the mixture fractions. The mixture fraction is computed using Bilgers formula [Bilger, 1988]. The horizontal line in Fig. 3.27



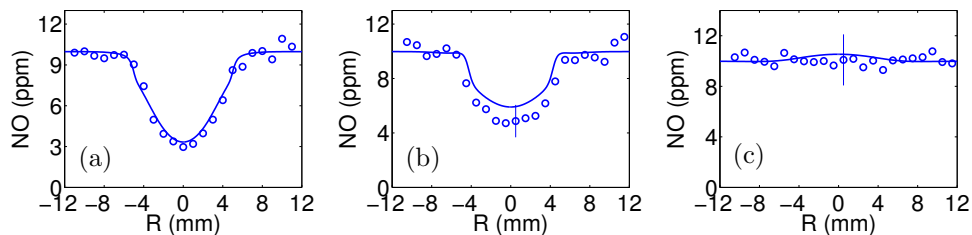


**Figure 3.28:** The (circles) measured and (lines) computed radial profiles of NO mole fractions for Case M<sub>H<sub>2</sub></sub> at (a)  $Z = 3$  mm, (b)  $Z = 6$  mm and (c)  $Z = 15$  mm.

marks the position of stoichiometric mixture fraction. Here, it is observed that the mixture fraction is predicted well, but the CH<sub>4</sub> and H<sub>2</sub> profiles are less accurately reproduced (Fig. 3.26).

Although computations of Case M<sub>H<sub>2</sub></sub> reproduce quite well the general trend of experimental data, there are some quantitative differences. Examination of experimental and computed profiles suggests that the computational flame burns faster than the experimental one. A possible reason for the differences might be the choice of boundary conditions. Namely, for Case M and M<sub>H<sub>2</sub></sub>, the thermal boundary layer between the fuel tube and the coflow was chosen in a way to reproduce the measured values of temperature for the non-reacting mixture (see Fig. 3.3). To do this, CH<sub>4</sub> has been completely removed and replaced by N<sub>2</sub>, keeping all other parameters of Case M the same, to avoid any possible heat release. The computed temperature corresponded very well with measured values at a height of 3 mm and 12 mm above the fuel tube exit and further modeling of Case M provided a very good match with the experimental data. For Case NP, P and M, however, we did not check the sensitivity of the numerical results to the chosen boundary conditions. In an attempt to analyze the sensitivity, computations have been performed with a considerably reduced thickness of thermal boundary layer. Figure 3.25 includes radial profiles of temperature and species concentrations computed using these new boundary conditions at a height of 6 mm. The figure shows that decreasing the boundary layer thickness does not affect significantly both the temperature and species distributions.

While we cannot exclude other possible reasons for the differences observed (for instance, uncertainties in kinetics and transport, or uncertainty in vertical position), it is believed that a further analysis of the physical/chemical reasons would hardly be justified and is beyond the scope of this study. Moreover, such an analysis would require additional experiments, perhaps, measurements of OH radical distribution might be beneficial for this purpose. Furthermore, there might not be a single reason to explain these differences.

### 3.7.3 NO formation and consumption

Figure 3.28 displays NO radial profiles computed and measured at axial positions of 3, 6 and 15 mm of Case M<sub>H<sub>2</sub></sub>. At axial distances of 3 and 6 mm, NO profiles show

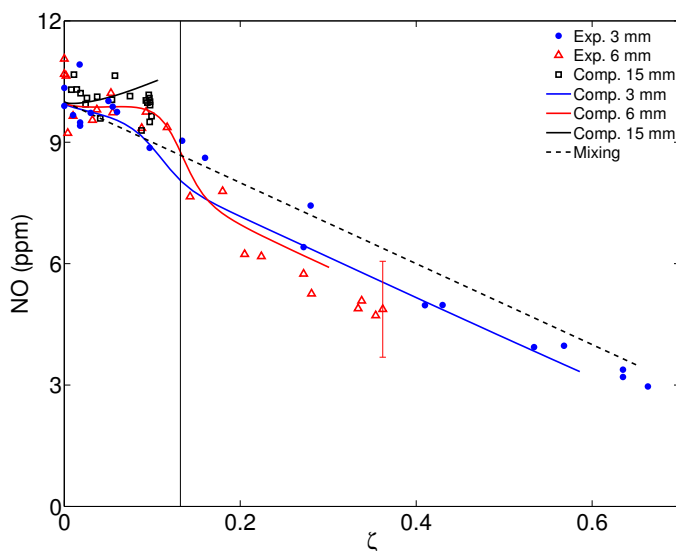


**Figure 3.29:** The (symbols) measured and (lines) computed NO mole fractions versus mixture fraction for Case M<sub>H<sub>2</sub></sub>. The vertical line marks the position of stoichiometric mixture fraction.

a minimum at the flame center, at 15 mm the profile becomes flat. Comparison with the computed profiles shows an excellent agreement. A similar trend of NO radial profile with downstream distance has been noticed in Case M. It was observed (by analyzing the experimental and computational data in mixture fraction space) that the NO field is dominated by mixing of the NO formed in the coflow with reaction products of the diluted fuel together with a negligible amount of NO formation in the fuel via the Fenimore mechanism. To check the effects of H<sub>2</sub> addition on the NO formation, the computational and experimental results are plotted as a function of mixture fraction for Case M<sub>H<sub>2</sub></sub> in Fig. 3.29. This figure also includes the mixing line indicating simple mixing of the hot coflow with the fuel jet. The measurements and computations at 3 and 15 mm cluster around the mixing curve demonstrating almost no NO formation or consumption. The comparison of NO fraction at 6 mm with the mixing line demonstrates a noticeable NO consumption at fuel rich conditions, the difference is on the level approximately 30%, clearly outside the measurement uncertainty of 20%. The computations support the measurements quantitatively, although they predict a somewhat smaller difference with the mixing line (approximately 20%) at fuel rich conditions. The rate-of-production analysis, similar to Case M, reveals that the consumption is mostly due to the conversion of NO molecules to the N-containing intermediates (HCN, NH<sub>3</sub> and HNCO). These intermediates are converted back to NO at downstream distances.

## 3.8 Conclusions

A numerical study has been carried out to investigate laminar coflow flames with a different degree of dilution and preheating from the “standard” condition to the Mild combustion regime. Computations performed using detailed chemistry GRI-Mech 3.0, mixture-averaged multi-component transport and optically-thin radiation model. At the first stage, structure and stabilization mechanism of coflow flames have been studied in their transition to the Mild combustion regime. An overall good qualitative and quantitative agreement was found between results of detailed computations and experiments for Case NP, Case P and at lower axial distances for Case M. However, the agreement for Case M at higher axial distances was quite fair. Possible reasons for discrepancies at these locations include slightly asymmetrical flow pattern of the experimental flame and uncertainties related to chemical mechanism and transport model in Mild condition. It was shown that the progressive preheating and dilution of the oxidizer and fuel results in a reduction of the temperature rise in the reaction zone, which becomes very small for Case M. Moreover, analysis of heat release and formaldehyde revealed that stabilization of Case NP and P occur by an edge flame in contrast to Case M which is stabilized by the autoignition. Autoignition of this case starts from a very lean mixture fraction (at most reactive mixture fraction) and further downstream it progresses towards stoichiometric and rich mixture fractions. Application of constant Schmidt numbers and neglecting radiative heat loss has been investigated for Case NP. Assuming constant Schmidt numbers yields worse predictions than the mixture-averaged model in the centerline of the coflow. Radiative losses are not important at lower axial distances; however their effect becomes increasingly important at higher axial distances. This happens due to increasing radiative losses of a parcel of burned gas traveling along the axial direction. Analysis of the computational and experimental data has also been performed in mixture fraction space. In Case NP and P, it turns out that these data are perfectly correlated at different heights and they are on top of a single line within the uncertainty of the measurements. However, in Case M, this correlation is perturbed at lower axial distances due to the incomplete combustion of the fuel/oxidizer mixture. Further analysis has been performed by comparison of the flame structure of Case M with the stationary and igniting flamelets. Results indicate ignition structure of the flame at lower axial distances which demonstrates stabilization of this flame by autoignition.

Analysis of NO for Case NP and P indicates a considerable amount of NO formation (on the level of 100 ppm), while the NO formation of Case M appears to be negligible (a few ppm). Computations of NO mole fractions are in an excellent agreement with measurements for all studied cases. The rate-of-production analysis reveals that the NO formation in all flames studied here is predominantly caused by the Fenimore mechanism. Analysis of computational results also indicates that the reaction reversed to the reaction  $\text{CH} + \text{N}_2 \rightarrow \text{NCN} + \text{H}$  returns a considerable fraction (approximately 35%) of NCN back to  $\text{N}_2$  in all studied flames. Analysis of Case M with a significant level of NO mole fraction present in the coflow shows the considerable reduction of the seeded NO at heights of 3 and 12 mm. It is revealed that the reduction is due to the conversion of NO molecules to N-containing

intermediates rather than  $N_2$ . Based on results, at height of 25 mm, all formed N-containing intermediates are already converted back to NO.

Fuel flexibility of Mild combustion has been investigated by addition of  $H_2$  to the fuel of Case M. The numerical data are in a reasonably good agreement with the measurements. Addition of hydrogen appreciably decreases the flame height (approximately 25%) and promotes ignition, however only modestly affects maximum flame temperature and thickness of combustion zone. Stabilization mechanism of the Case M- $H_2$  is autoignition which is initiated at most reactive mixture fraction ( $\zeta_{MR} < 0.13$ ) very close to the coflow stream. Preferential diffusion of  $H_2$  leads to an increased presence of hydrogen at this location which significantly increases chemical reactivity and improves flame stability. Analysis of the NO fraction as a function of mixture fraction indicates that the NO distribution is dominated by mixing of the NO formed in the coflow with the reaction products of the diluted fuel, with negligible NO formation from the fuel. Computations and experiments show a considerable reduction of the seeded NO at a height of 6 mm. It is revealed that, similar to Case M, the reduction is due to the conversion of the NO molecules to the N-containing intermediates which are converted back to NO at downstream distances.



# LES of turbulent lifted flames with hydrogen addition using FGM-PDF model

Numerical modeling of Mild combustion in large scale flows requires sophisticated models which are able to predict complex autoignition events. In the laboratory scale Mild burners (JHC burners), these autoignition events are typically initiated at very small mixture fractions due to an intense dilution of oxidizer stream. In this region, turbulent structures in the fuel stream can hardly intrude the ignition events. This induces that influence of molecular diffusion on autoignition is comparable to that of turbulence transport (eddy viscosity). Addition of  $H_2$  to fuel makes molecular diffusion and preferential diffusion effects increasingly important.

This chapter reports on the numerical investigation of preferential diffusion effects in the lift-off height and stabilization mechanism of turbulent lifted  $CH_4/H_2$  flames in a hot and diluted environment. For this purpose, a novel numerical model is developed based on the FGM technique to account for preferential diffusion effects in autoignition. Such development is inevitable since investigations with detailed chemistry indicate that preferential diffusion affects strongly autoignition of the hydrogen enriched mixtures. IML-flamelets are introduced and analyzed to accommodate preferential diffusion effects in a flamelet database. In the next stage, the developed FGM approach is implemented in LES of the  $H_2$  enriched turbulent lifted jet flames. Computations reveal that the enrichment of fuel with hydrogen leads to a significant change in the lift-off height and stabilization mechanism of the

---

The content of this chapter has been extracted from the following papers:

S.E. Abtahizadeh, J.A. van Oijen, L.P.H. de Goey, *A novel flamelet-based reduced model to include preferential diffusion in autoigniting flames*, submitted to Proceedings of Combustion Institute (2013).

S.E. Abtahizadeh, J.A. van Oijen, L.P.H. de Goey, *Investigation of preferential diffusion effects in turbulent lifted  $CH_4/H_2$  flames using LES with a novel FGM-PDF model*, submitted to Proceedings of Combustion Institute (2013).

Minor adaptations have been performed to streamline the layout of the thesis.

lifted flames. Main features of these turbulent lifted flames such as the formation of ignition kernels and stabilization mechanisms are thoroughly analyzed and compared with the measurements of OH chemiluminescence.

## 4.1 Introduction

A number of experimental studies have been performed to study the Jet-in-Hot Coflow (JHC) burner as a model system for Mild combustion [Cabra et al., 2005; Dally et al., 2002; Oldenhof et al., 2010]. In most of these experiments, a turbulent lifted flame has been observed as a result of autoignition of a fuel jet in the hot environment of burned gas. The Delft Jet-in-Hot Coflow (DJHC) burner has been devised by Oldenhof et al. [2010] with some minor differences with the Adelaide burner [Dally et al., 2002]. They performed measurements of lifted methane flames for temperature and velocity using Coherent Anti-Stokes Raman Spectroscopy (CARS) and Laser Doppler Anemometry (LDA), respectively. It has been reported that the lifted flame is stabilized by autoignition in which ignition kernels form, grow and convect downstream.

Later on, these experiments were extended for the hydrogen enriched fuels by Arteaga et al. [2013]. In these experiments, the methane fuel has been enriched with various amounts of hydrogen ranging from 0% to 25% of fuel volume. Measurements of OH chemiluminescence revealed that addition of only a small amount of hydrogen to methane affects the flame's lift-off height and stabilization mechanism significantly. Some of these hydrogen enriched turbulent flames were lifted and others were attached to the burner. Prediction of autoignition in these flames might depend strongly on molecular diffusion modeling. However, the complex role of molecular and preferential diffusion on autoignition of such flames has not been investigated in previous studies.

Recent Direct Numerical Simulations (DNS) of autoigniting mixing layers of  $\text{CH}_4/\text{H}_2$  mixtures with detailed chemistry and transport models by van Oijen [2013] have shed some light to this issue on a smaller scale flow. It was shown that autoignition occurs at very small mixture fractions ( $< 0.02$ ), very close to the oxidizer side due to the intense dilution of the oxidizer. It was observed that in this condition, molecular diffusion becomes as important as turbulent mixing in autoignition. The presence of hydrogen enhances the role of molecular diffusion due to its high diffusivity. The simulations showed that  $\text{H}_2$  diffuses out of the fuel mixture into the hot oxidizer leading to a much faster ignition process governed by hydrogen chemistry.

Numerical modeling of  $\text{H}_2$  enriched Mild combustion in large scale reacting flows, as in the DJHC burner, requires reduced models for turbulence and chemistry. These models should be able to predict adequately complex autoignition events under large preferential diffusion effects. Successful reduction techniques to accommodate preferential diffusion are mainly based on flamelets [Peters, 1984], such as FGM (Flamelet Generated Manifold) [van Oijen and de Goey, 2000], FPV (Flamelet Progress Variable) [Ihme et al., 2005] and REDIM (Reaction-Diffusion Manifolds) [Bykov and Maas, 2007]. Inclusion of preferential diffusion in FGM has been studied by van Oijen and de Goey [2000] and later on by de Swart et al. [2010]

in the context of premixed flames. It has been shown that two controlling variables are needed to account for local variations in equivalence ratio and mass burning rate. Preferential diffusion in the context of non-premixed flames has been taken into account by [Pitsch et al. \[1998\]](#); [Pitsch \[2000\]](#). In their work, a set of flamelet equations was derived with extra terms to account for non-unity Lewis number transport. This model has been used in many studies of turbulent non-premixed flames. Flamelet-based models were also used to study autoignition in turbulent jet flames (e.g. [Bekdemir et al., 2013](#)), but the effect of preferential diffusion on autoignition was not investigated. To the author's knowledge, there is no previous study about the incorporation of preferential diffusion effects in a flamelet-based technique for autoigniting non-premixed flames.

An important issue in the numerical modeling of Mild combustion (as in the DJHC burner) is flame stabilization which is mainly governed by autoignition. Although there are many Reynolds-Averaged Navier-Stokes (RANS) studies in this field [[Coelho and Peters, 2001](#); [Kim et al., 2005](#); [Christo and Dally, 2005](#)], these unsteady ignition events are strongly intermittent for which Large Eddy Simulation (LES) is known to provide more accurate results. Among different approaches for LES of JHC burners, two of them have been widely and successfully used. They are either based on transported PDF methods with reduced chemistry [[Pope, 1985](#); [Haworth, 2010](#)] or based on flamelet-based reduction techniques such as FGM, FPV and FPI (Flame prolongation of ILDM) [[Gicquel et al., 2000](#)]. Accuracy of predictions by transported PDF methods depends strongly on the micro-mixing model. In spite of a higher accuracy of this approach compared to presumed PDF approaches, a large set of differential equations has to be solved for an accurate description of the probability of occurrences, which results in a very large computational time. Moreover, inclusion of preferential diffusion effects in the framework of transported PDF methods is an open research question.

Application of flamelet-based reduction techniques within LES has been reported by a number of studies for non-premixed flames assuming a unity Lewis number approximation for the combustion model [[Vreman et al., 2008](#); [Bekdemir et al., 2013](#); [Ihme and See, 2010, 2011](#)]. In the context of JHC burners, [Ihme and See \[2010\]](#) employed the Unsteady Flamelet Progress Variable (UFPV) model for LES of the Cabra burner [[Cabra et al., 2005](#)] with CH<sub>4</sub>/air fuel. It is believed that for methane base fuels, the application of unity Lewis numbers yields accurate results. They predicted turbulent lifted flames in a good agreement with measurements. In a later study, [Ihme and See \[2011\]](#) simulated the HM3 case of the Adelaide burner [[Dally et al., 2002](#)] with a similar methodology but with the addition of an extra conserved scalar to account for the third stream. Within their methodology, they used a mean scalar for temperature of the coflow and they found a good agreement with measurements of temperature, mixture fraction and concentrations of species. Due to a considerable amount of hydrogen in the HM3 case, the flame is almost attached to the burner with a structure similar to piloted flames, e.g. [[Barlow and Frank, 2003](#)]. For such flames, application of unity Lewis number may yield accurate results. However, for autoigniting lifted flames of CH<sub>4</sub>/H<sub>2</sub> mixtures, application of unity Lewis number in the combustion model might lead to inaccurate results.

In this chapter, first, a novel FGM-based model is developed to account for pref-



**Table 4.1:** Temperature and molar composition of the fuel stream for the different cases. The oxidizer stream has the same composition for all cases:  $T = 1437$  K,  $X_{\text{O}_2} = 0.0485$ ,  $X_{\text{H}_2\text{O}} = 0.1452$ ,  $X_{\text{CO}_2} = 0.0727$ ,  $X_{\text{N}_2} = 0.7336$ .  $\zeta_{st}$  is the stoichiometric mixture fraction.

Case	$T$ (K)	$X_{\text{H}_2}$	$X_{\text{CH}_4}$	$X_{\text{C}_2\text{H}_6}$	$X_{\text{N}_2}$	$\zeta_{st}$
D00H <sub>2</sub>	448	0.00	0.813	0.037	0.15	0.0178
D05H <sub>2</sub>	448	0.05	0.763	0.037	0.15	0.0179
D10H <sub>2</sub>	448	0.10	0.713	0.037	0.15	0.0180
D25H <sub>2</sub>	448	0.25	0.563	0.037	0.15	0.0183

erential diffusion effects in autoignition of CH<sub>4</sub>/H<sub>2</sub> mixtures. In subsection 4.2.1, the Igniting Mixing Layer flamelets (IML-flamelets) are introduced with the relevant governing equations. The IML-flamelets are analyzed and compared with the commonly used Igniting CounterFlow diffusion flamelets (ICF-flamelets) in terms of preferential diffusion effects in subsection 4.2.2. In subsection 4.2.3, the tabulation of the IML-flamelets is discussed. An appropriate set of transport equations for the controlling variables is derived to account for non-unity Lewis number transport in subsection 4.2.4. Finally, in subsection 4.2.5, the performance of the proposed FGM model is evaluated and validated by comparison with predictions of detailed chemistry.

Afterwards, a LES model based on the developed FGM-PDF is proposed to simulate turbulent lifted flames of the DJHC burner with the H<sub>2</sub> enriched fuels. The focus is on the prediction of autoignition in turbulent lifted flames under significant influence of preferential diffusion effects. Subsection 4.3.1 comprises a description of the LES model and numerical methodology. Computational results are presented in the following subsections in which LES of the lifted flames are conducted and compared with measurements to illustrate effect of molecular diffusion and preferential diffusion. Finally, the conclusions are drawn.

## 4.2 Development of FGM to preferential diffusion and autoignition

### 4.2.1 IML-flamelets

In this section, the goal is to develop a flamelet model that can predict the effect of preferential diffusion on autoignition of methane-hydrogen mixtures at the conditions in JHC experiments. In total, four cases are studied containing 0 to 25 percent of H<sub>2</sub>, which are summarized in Table 4.1. These cases correspond to the mass-flux averaged boundary conditions of the DJHC burner experiments [Arteaga et al., 2013]. In these experiments, the fuel and oxidizer streams are initially separated. Once the fuel is injected into the hot oxidizer stream, mixing starts, which is then followed by autoignition. Igniting Mixing Layer flamelets (IML-flamelets) are introduced here to model this process of mixing and autoignition such as in the DJHC burner. IML-flamelets are basically similar to the commonly used one-dimensional Igniting CounterFlow diffusion flamelets (ICF-flamelets) with a notable distinction

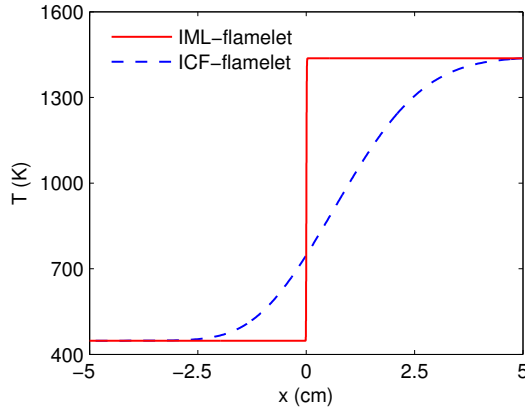


**Figure 4.1:** Comparison of the initial temperature profile ( $t = 0$  s) between ICF-flamelet and IML-flamelet.

in the initial condition and inflow momentum. In ICF-flamelets, it is a common practice [Ihme and See, 2010; Bekdemir et al., 2013] to generate an initial condition by assuming a steady-state molecular mixing field between the fuel and oxidizer stream with frozen chemistry ( $\dot{\omega} = 0$ ) as it is shown in Fig. 4.1. This situation implies that a steady-state mixing field is reached before any chemical reaction takes place. This assumption is only valid if the time scale of mixing is much shorter than the chemical time scales. However, such an assumption may lead to unrealistic predictions if molecular diffusion effects are comparable to the chemical source terms (for example in  $\text{H}_2$ -enriched methane mixtures). In this case, molecular diffusion has a large influence on autoignition time scales. This situation is extensively discussed in the next subsection.

In IML-flamelets, in contrast to ICF-flamelets, fuel and oxidizer streams are initially unmixed as it is shown in Fig. 4.1. In this situation, the thermo-chemical properties have a step-function profile in physical space. Their values are equal to the fuel boundary on one side of the domain ( $x < 0$  in Fig. 4.1) and equal to the oxidizer boundary at the other side ( $x > 0$  in Fig. 4.1). Due to the steep gradient of mixture fraction  $\zeta$  at the interface, the scalar dissipation rate  $\chi = 2D(\partial\zeta/\partial x)^2$  is very large at this point. During the molecular mixing process, the scalar dissipation rate (rapidly) decreases and chemical reactions may start at any time during the mixing process. In IML-flamelets, the gradient of mixture fraction is not enforced by an inflow momentum (i.e. an applied strain). However, it is governed purely by molecular diffusion. In the absence of an applied strain, the species mass fractions and temperature approach chemical equilibrium for  $t \rightarrow \infty$ .

The configuration of IML-flamelets resembles practical non-premixed systems in which mixing of the fuel and the oxidizer initiates after their injection from the nozzle exit at very large scalar dissipation rates. In these systems, chemical equilibrium can be reached at a sufficiently large distance from the burner where scalar dissipation rates approach zero.

The mathematical formulation of IML-flamelets is described by the following set of one-dimensional transport equations:

$$\frac{\partial \rho}{\partial t} + \frac{\partial \rho u}{\partial x} = 0 \quad (4.1)$$

$$\frac{\partial(\rho Y_i)}{\partial t} + \frac{\partial(\rho u Y_i)}{\partial x} = \frac{\partial}{\partial x} \left( \frac{\lambda}{Le_i c_p} \frac{\partial Y_i}{\partial x} \right) + \dot{\omega}_i \quad (4.2)$$

$$\frac{\partial(\rho h)}{\partial t} + \frac{\partial(\rho u h)}{\partial x} - \frac{\partial}{\partial x} \left( \frac{\lambda}{c_p} \frac{\partial h}{\partial x} \right) = \frac{\partial}{\partial x} \left[ \frac{\lambda}{c_p} \sum_{i=1}^{N_{sp}} \left( \frac{1}{Le_i} - 1 \right) h_i \frac{\partial Y_i}{\partial x} \right] \quad (4.3)$$

with initial conditions for  $Y_i(x, t)$ ,  $h(x, t)$  and  $u(x, t)$  as:

$$Y_i(x, 0) = \begin{cases} Y_{i, fu} & \text{if } x < 0 \\ Y_{i, ox} & \text{if } x \geq 0 \end{cases}, \quad h(x, 0) = \begin{cases} h_{fu} & \text{if } x < 0 \\ h_{ox} & \text{if } x \geq 0 \end{cases}, \quad u(x, 0) = 0 \quad (4.4)$$

where  $\rho$ ,  $\lambda$  and  $c_p$  refer to mixture density, thermal conductivity and specific heat at constant pressure, respectively.  $Le_i$ ,  $t$  and  $N_{sp}$  refer to the Lewis number of species  $i$ , time and total number of species present in the chemical scheme, respectively.  $Y_i$ ,  $\dot{\omega}_i$  refer to mass fraction and chemical source term of species  $i$ , respectively. The set of governing equations for the IML-flamelets is solved by the CHEM1D code which is developed at the Eindhoven University of Technology [Somers, 1994].

## 4.2.2 Analysis of preferential diffusion effects

In this subsection, the effect of preferential diffusion on autoignition is investigated for the case with the highest  $H_2$  fraction (D25 $H_2$ ) by using different flamelet types. Figure 4.2 shows the temporal evolution of temperature in physical space for both types of flamelets by using detailed chemistry GRI-Mech 3.0 [Smith et al., 2000] but different diffusion models. In this figure, temperature profiles are shown incrementally in time in which each time level is plotted with a different color. The initial profile is a step-function for the IML-flamelets (Fig. 4.2a and b) while it is a mixed field for the ICF-flamelets (Fig. 4.2c and d). Comparison of the flamelets using unity Lewis numbers ( $Le_i = 1$ ) with those using constant non-unity Lewis numbers ( $Le_i = c_i$ ) reveals that preferential diffusion affects strongly the evolution of temperature for both types of flamelets.

A quantitative comparison of the autoignition time scales between the ICF-flamelets and IML-flamelets is shown in Fig. 4.3.  $\Delta T$  represents the maximum temperature rise across mixture fraction  $\zeta$  space at each time level:

$$\Delta T(t) = \max_{\zeta} (T(\zeta, t) - T(\zeta, 0)). \quad (4.5)$$

The evolution of  $\Delta T$  is shown in Fig. 4.3 for IML-flamelets which are computed by using transport models  $Le_i = 1$  and  $Le_i = c_i$ . It is observed that the autoignition time scale of the IML-flamelets decreases significantly by inclusion of preferential diffusion effects.

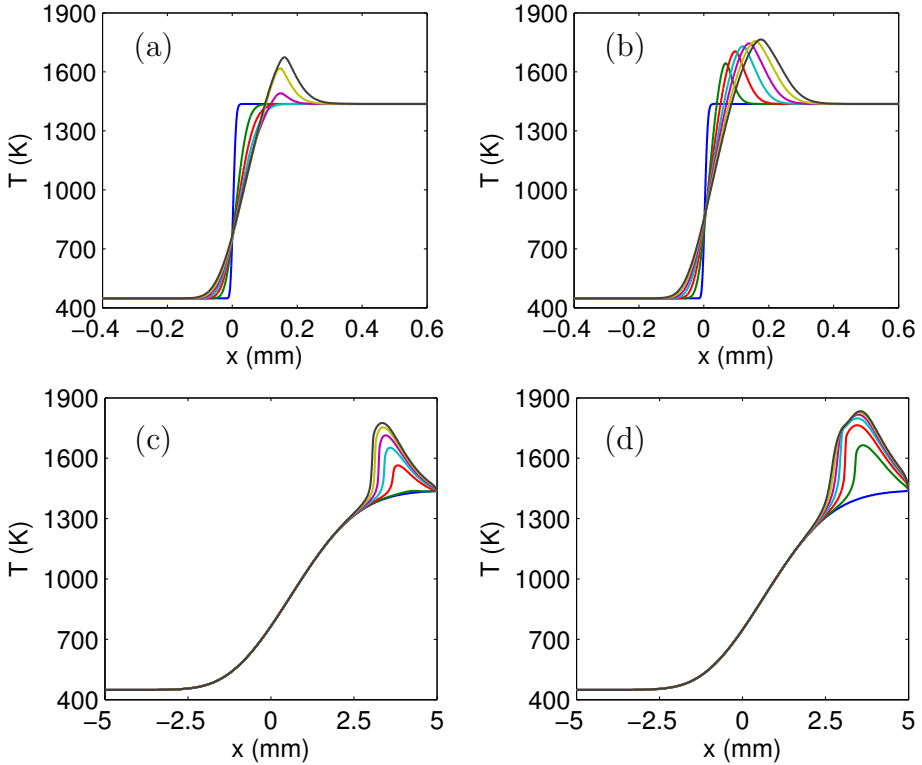


**Figure 4.2:** Evolution of temperature for (a) IML-flamelets with  $Le_i = 1$ , (b) IML-flamelets with  $Le_i = c_i$ , (c) ICF-flamelets with  $Le_i = 1$  and (d) ICF-flamelets with  $Le_i = c_i$ . Flamelets are plotted at  $t = 0, 0.5, 1, \dots, 3$  ms.

In ICF-flamelets, it is possible to use different transport models for the initial profile ( $t = 0$  s) and its time evolution ( $t > 0$  s). This means that  $Le_i = c_i$  transport can be used to generate the initial condition (IC: $Le_i = c_i$ ) while  $Le_i = 1$  is used to compute the evolution from such an initial condition and vice versa. Assuming unity Lewis numbers for the computation of the initial condition leads to linear profiles of  $Y_i$  in mixture fraction space, which were used in some previous studies (e.g. [Domingo et al., 2008]). Figure 4.3b shows that the ignition delay of the ICF-flamelets depends solely on the assumed transport model for initial conditions regardless of the transport model used to compute the flamelets. When  $Le_i = c_i$  transport is used to generate the initial condition (IC: $Le_i = c_i$ ) for the ICF-flamelets, using both transport models in the actual simulation results in the same autoignition time scale. The same trend can be observed when unity Lewis numbers are used to compute the initial condition (IC: $Le_i = 1$ ).

From these results, it can be concluded that preferential diffusion is mainly important in the pre-ignition phase in which the reactants are mixed. However, once ignition starts after this phase, the chemical source terms become much larger

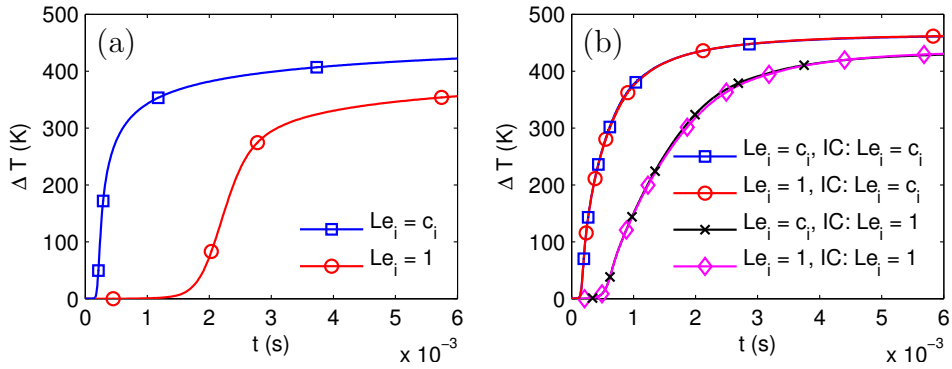


**Figure 4.3:** Temperature rise  $\Delta T$  computed using detailed chemistry and different transport models for (a) IML-flamelets and (b) ICF-flamelets. In figure (b), different transport models have been used to compute the Initial Condition (IC) for the ICF-flamelets.

than diffusion terms, which minimize the effect of molecular diffusion.

Figure 4.3 also shows that autoignition is delayed for both type of flamelets by assuming unity Lewis numbers. Due to the absence of preferential diffusion, the hydrogen cannot diffuse out of the fuel stream into the hot oxidizer as explained in [van Oijen, 2013]. The ignition delay for the IML-flamelet is longer than for the ICF-flamelet, because the scalar dissipation, which has a delaying effect, is much larger in the IML-flamelet.

The IML-flamelet using  $Le_i = c_i$  shows a very similar autoignition time scale compared to ICF-flamelets with an initial condition based on non-unity Lewis numbers (IC: $Le_i = c_i$ ). In both cases, preferential diffusion of hydrogen leads to a very reactive mixture with short chemical time scales. In this case, the large chemical source terms make the influence of the scalar dissipation rate on autoignition negligible. In order for molecular transport and preferential diffusion to influence autoignition time scales, chemical source terms should be sufficiently small.

To support this explanation, a situation is considered in which the chemical source terms are slightly decreased. Figure 4.4 shows  $\Delta T$  for both flamelet types in which the oxidizer temperature has been decreased by 200 K. It is observed that at this lower temperature, the ignition delay is longer for both flamelets and indeed the effect is stronger for the IML-flamelet because of the higher scalar dissipation rate in this flamelet type. It can be concluded that IML-flamelets provide an appropriate flamelet configuration to incorporate unsteady molecular mixing and to capture the influence of preferential diffusion on autoignition.

### 4.2.3 Tabulation of IML-flamelets

In this subsection, a methodology is developed to predict autoignition of hydrogen containing fuels using the FGM framework. In this framework, a reacting flow problem is solved using only a small set of partial differential equations instead of the full set of equations for all species. IML-flamelets are tabulated to generate a

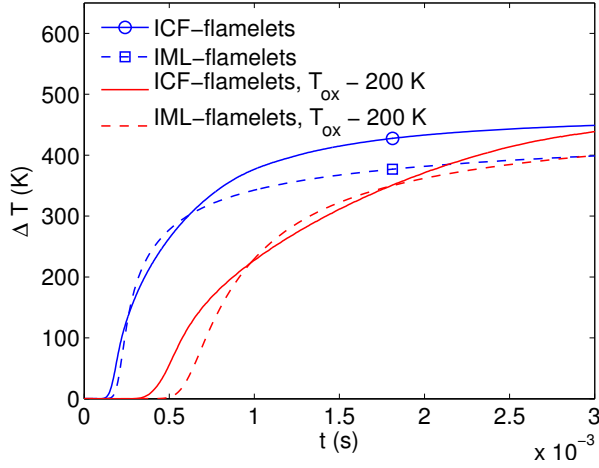


**Figure 4.4:** Comparison of the temperature rise  $\Delta T$  of flamelets using detailed chemistry and  $Le_i = c_i$  transport at the reference and reduced oxidizer temperatures.

flamelet database which, as discussed in the previous subsections, take adequately into account preferential diffusion effects during molecular mixing and consequently autoignition. The most accurate approach to include these effects is to adopt four controlling variables, which include the independent mass fractions of the chemical elements  $z_C$ ,  $z_H$ ,  $z_O$ , and enthalpy  $h$ . In this study, we try to capture the changing local conditions of the elements by taking into account a minimum number of controlling variables to keep the computational cost low. For this purpose, IML-flamelets are stored in a flamelet database (or manifold) using two controlling variables, mixture fraction  $\zeta$  and a reaction progress  $\mathcal{Y}$  to account for mixing and reaction, respectively. These controlling variables are defined in such a way that they represent chemistry with a monotonic increasing reaction progress.

The mixture fraction  $\zeta$  is defined by a linear combination of elemental mass fractions using the weight factors following Bilger’s formulation [Bilger, 1988]. The mixture fraction is normalized in such a way to have its minimum and maximum value in the oxidizer ( $\zeta = 0$ ) and fuel ( $\zeta = 1$ ), respectively. Using these definitions,  $\zeta$  can be written as a linear combination of species mass fractions

$$\zeta = \sum_{i=1}^{N_{sp}} \beta_i Y_i. \quad (4.6)$$

The reaction progress, in general, has the form of:

$$\mathcal{Y} = \sum_{i=1}^{N_{sp}} \alpha_i Y_i \quad (4.7)$$

in which  $\alpha_i$  refers to the weight factors which are optimized to yield a smooth mapping of the variables with respect to the controlling variables. Here, the coef-

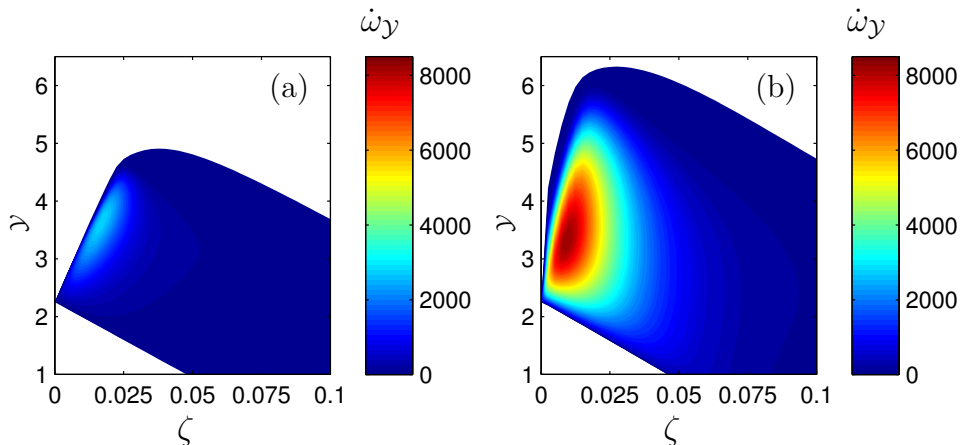


**Figure 4.5:** Chemical source term of reaction progress  $\dot{\omega}_Y$  as a function of mixture fraction  $\zeta$  and reaction progress  $\mathcal{Y}$ . The transport model used for generation of the manifold is (a)  $Le_i = 1$  and (b)  $Le_i = c_i$ .

ficients are chosen as  $\alpha_{O_2} = -0.5/W_{O_2}$ ,  $\alpha_{CH_4} = -0.5/W_{CH_4}$ ,  $\alpha_{CO_2} = -0.8/W_{CO_2}$ ,  $\alpha_{H_2O} = 1/W_{H_2O}$ ,  $\alpha_{C_2H_6} = -3/W_{C_2H_6}$ , in which  $W_i$  denotes the molar mass of species  $i$ .  $\alpha_i = 0$  for all other species. This combination yields a monotonic increasing value of the reaction progress with time for all  $\zeta$ . Note that this progress variable is not normalized and has non-zero values in the frozen mixing limit.

Figure 4.5 shows a contour plot of the source term of the reaction progress  $\dot{\omega}_Y$  in the manifold using IML-flamelets with  $Le_i = 1$  and  $Le_i = c_i$  transport. An interesting observation is that there is a significant influence of preferential diffusion on the distribution and magnitude of the source term. The manifold which is generated by  $Le_i = c_i$  has an approximately two times higher peak source term. This might lead to significant differences when these flamelet databases are used in flame simulations.

#### 4.2.4 Derivation of transport equations for the controlling variables

When a flamelet database is used in a flame simulation, transport equations for the controlling variables ( $\zeta$  and  $\mathcal{Y}$ ) have to be solved. All other thermo-chemical variables can be retrieved from the database. In order to derive a transport equation for the reaction progress, we consider the conservation equation for species assuming a Fick-like diffusion:

$$\frac{\partial \rho Y_i}{\partial t} + \nabla \cdot (\rho u Y_i) = -\nabla \cdot \left( \frac{\lambda}{Le_i c_p} \nabla Y_i \right) + \dot{\omega}_i. \quad (4.8)$$

By splitting the contribution of species diffusion into non-preferential diffusion and preferential diffusion parts, Eq. 4.8 reads:

$$\frac{\partial \rho Y_i}{\partial t} + \nabla \cdot (\rho u Y_i) + \nabla \cdot \left( \frac{\lambda}{c_p} \nabla Y_i \right) = -\nabla \cdot \left( \frac{\lambda}{c_p} \left( \frac{1}{Le_i} - 1 \right) \nabla Y_i \right) + \dot{\omega}_i. \quad (4.9)$$

A transport equation for  $\mathcal{Y}$  is obtained by taking a linear combination of Eq. 4.9 using Eq. 4.7:

$$\frac{\partial \rho \mathcal{Y}}{\partial t} + \nabla \cdot (\rho u \mathcal{Y}) - \nabla \cdot \left( \frac{\lambda}{c_p} \nabla \mathcal{Y} \right) = \nabla \cdot \left( \frac{\lambda}{c_p} \sum_{i=1}^{N_{sp}} \alpha_i \left( \frac{1}{Le_i} - 1 \right) \nabla Y_i \right) + \dot{\omega}_{\mathcal{Y}} \quad (4.10)$$

A similar transport equation for the mixture fraction is derived using Eqs. 4.9 and Eq. 4.6:

$$\frac{\partial \rho \zeta}{\partial t} + \nabla \cdot (\rho u \zeta) - \nabla \cdot \left( \frac{\lambda}{c_p} \nabla \zeta \right) = \nabla \cdot \left( \frac{\lambda}{c_p} \sum_{i=1}^{N_{sp}} \beta_i \left( \frac{1}{Le_i} - 1 \right) \nabla Y_i \right). \quad (4.11)$$

It is noted that Eq. 4.11 does not have a source term and the conservation equation for  $\zeta$  is only governed by convection, diffusion and accumulation.

Application of non-unity Lewis number transport leads to non-zero terms on the r.h.s. of Eqs. 4.10 and 4.11. These terms, which contain gradients of  $Y_i(\mathcal{Y}, \zeta)$ , are derived by using the chain rule:

$$\begin{aligned} \nabla \cdot \left( \frac{\lambda}{c_p} \sum_{i=1}^{N_{sp}} \gamma_i \left( \frac{1}{Le_i} - 1 \right) \nabla Y_i \right) = \\ \nabla \cdot \left\{ \frac{\lambda}{c_p} \sum_{i=1}^{N_{sp}} \gamma_i \left( \frac{1}{Le_i} - 1 \right) \left[ \left( \frac{\partial Y_i}{\partial \mathcal{Y}} \right)_{\zeta} \nabla \mathcal{Y} + \left( \frac{\partial Y_i}{\partial \zeta} \right)_{\mathcal{Y}} \nabla \zeta \right] \right\}, \end{aligned} \quad (4.12)$$

in which  $\gamma_i$  refers to the  $\alpha_i$  and  $\beta_i$  coefficients in Eqs. 4.10 and 4.11, respectively. Substitution of Eq. 4.12 in Eqs. 4.10 and 4.11 yields:

$$\frac{\partial \rho \zeta}{\partial t} + \nabla \cdot (\rho u \zeta) - \nabla \cdot \left( \frac{\lambda}{c_p} \nabla \zeta \right) = \nabla \cdot (\Lambda_{\zeta, \zeta} \nabla \zeta + \Lambda_{\zeta, \mathcal{Y}} \nabla \mathcal{Y}), \quad (4.13)$$

$$\frac{\partial \rho \mathcal{Y}}{\partial t} + \nabla \cdot (\rho u \mathcal{Y}) - \nabla \cdot \left( \frac{\lambda}{c_p} \nabla \mathcal{Y} \right) = \nabla \cdot (\Lambda_{\mathcal{Y}, \zeta} \nabla \zeta + \Lambda_{\mathcal{Y}, \mathcal{Y}} \nabla \mathcal{Y}) + \dot{\omega}_{\mathcal{Y}}. \quad (4.14)$$

Equations (4.13) and (4.14) are transport equations for  $\zeta$  and  $\mathcal{Y}$ . The r.h.s. of these equations contain preferential diffusion fluxes in which the following coefficients are introduced:

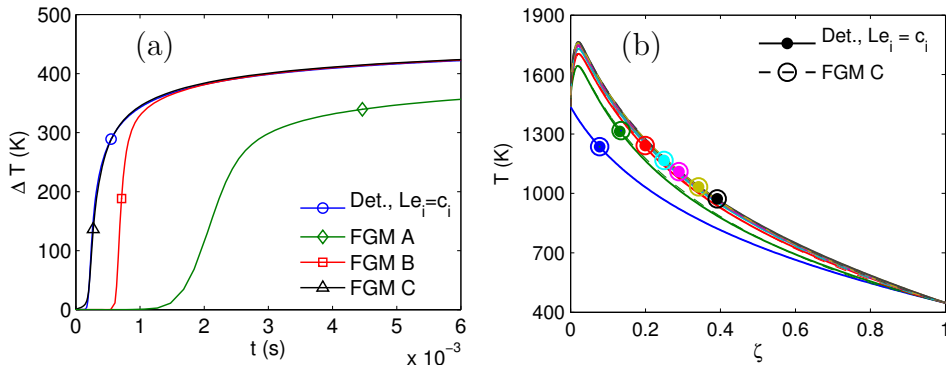
$$\Lambda_{\zeta, \zeta} = \frac{\lambda}{c_p} \sum_{i=1}^{N_{sp}} \beta_i \left( \frac{1}{Le_i} - 1 \right) \frac{\partial Y_i}{\partial \zeta} \Big|_{\mathcal{Y}}, \quad \Lambda_{\zeta, \mathcal{Y}} = \frac{\lambda}{c_p} \sum_{i=1}^{N_{sp}} \beta_i \left( \frac{1}{Le_i} - 1 \right) \frac{\partial Y_i}{\partial \mathcal{Y}} \Big|_{\zeta}, \quad (4.15)$$

$$\Lambda_{\mathcal{Y}, \zeta} = \frac{\lambda}{c_p} \sum_{i=1}^{N_{sp}} \alpha_i \left( \frac{1}{Le_i} - 1 \right) \frac{\partial Y_i}{\partial \zeta} \Big|_{\mathcal{Y}}, \quad \Lambda_{\mathcal{Y}, \mathcal{Y}} = \frac{\lambda}{c_p} \sum_{i=1}^{N_{sp}} \alpha_i \left( \frac{1}{Le_i} - 1 \right) \frac{\partial Y_i}{\partial \mathcal{Y}} \Big|_{\zeta}. \quad (4.16)$$



**Table 4.2:** FGM models using different transport models

Model	IML-flamelets	Transport equations
FGM A	$Le_i = 1$	$Le_i = 1$
FGM B	$Le_i = c_i$	$Le_i = 1$
FGM C	$Le_i = c_i$	$Le_i = c_i$

**Figure 4.6:** Comparison of (a) temperature rise  $\Delta T$  and (b) temperature evolution of IML-flamelets for Case D25H<sub>2</sub> with different models. In figure (b), lines with close circles and open circles refer to computations with detailed chemistry and FGM chemistry, respectively.

These diffusion fluxes incorporate preferential diffusion of each controlling variable due to a gradient of itself and the other controlling variable. The diffusion coefficients are calculated from the gradients of species mass fractions in the directions of  $\mathcal{Y}$  and  $\zeta$  in the manifold. The computed coefficients are stored in the manifold as a function of the controlling variables  $\mathcal{Y}$  and  $\zeta$ . They are retrieved from the table during solution of the transport equations.

### 4.2.5 Validation of the FGM model

In this subsection, the FGM model is used to perform simulations of igniting mixing layers and the results are compared with results of the full chemistry model. Three FGM implementations are considered which employ different transport models in the two stages of the FGM computation: 1) Creation of the IML-flamelet tables and 2) solving transport equations for the controlling variables. These models are summarized in Table 4.2. In FGM A, the IML-flamelets are generated using unity Lewis numbers ( $Le_i = 1$ ). FGM B and C have been constructed using a  $Le_i = c_i$  transport model. In model FGM C, the transport equations for the controlling variables (Eqs. 4.13 and 4.14) are solved in their full form including the preferential diffusion terms. Models FGM A and B do not consider these additional terms in the transport equations.

Figure 4.6a shows a comparison of the predicted temperature rise  $\Delta T$  for Case D25H<sub>2</sub> using detailed chemistry and the various FGM models. The results of the

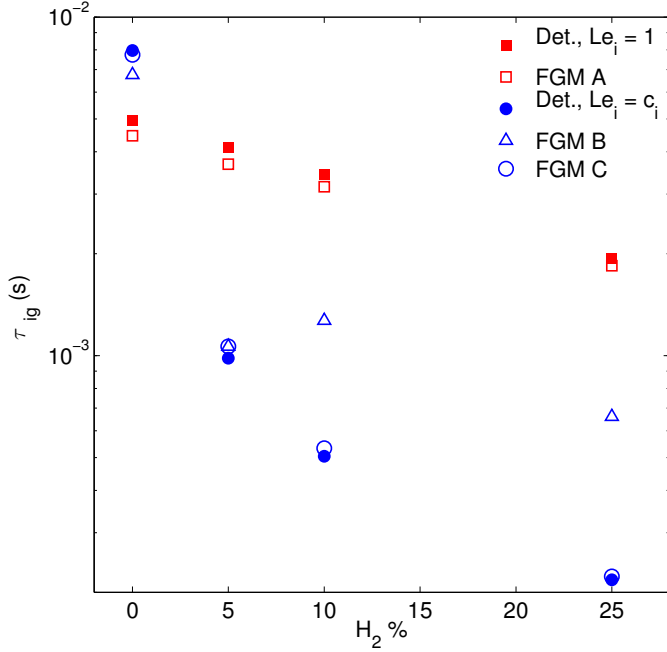


**Figure 4.7:** Computed ignition delay of IML-flamelets for Cases D00H<sub>2</sub>, D05H<sub>2</sub>, D10H<sub>2</sub> and D25H<sub>2</sub> using detailed chemistry with unity Lewis (Det.,  $Le_i = 1$ ), detailed chemistry with constant non-unity Lewis (Det.,  $Le_i = c_i$ ), FGM A, B and C models.

FGM C model, in which  $Le_i = c_i$  is used for both flamelets and transport equations, agree perfectly with the detailed chemistry solution. Such an agreement is also observed for the temporal evolution of temperature in mixture fraction space in Fig. 4.6b. The negligible differences are caused by interpolation errors in the manifold during tabulation of the IML-flamelets. When preferential diffusion effects are ignored in both stages of FGM calculation (FGM A), the ignition delay is almost 10 times longer than that in the detailed simulation. It is interesting to note that compared to FGM A, inclusion of preferential diffusion only in the manifold (FGM B) yields a considerable improvement in the predictions by a factor of four. This is caused by the much higher source terms in the manifold using  $Le_i = c_i$  with respect to the manifold using  $Le_i = 1$  (cf. Fig. 4.5).

A similar evaluation of the FGM models is performed for all four cases D00H<sub>2</sub>, D05H<sub>2</sub>, D10H<sub>2</sub> and D25H<sub>2</sub> in Fig. 4.7. In this evaluation, the ignition delay  $\tau_{ig}$  is defined as the time it takes to reach  $\Delta T = 50$  K, to quantify and compare predicted autoignition time scales. The choice of  $\Delta T = 50$  K is made considering the maximum temperature gradient  $dT/dt$  for all computations. It is observed that the FGM C model, compared to detailed chemistry (Det.,  $Le_i = c_i$ ), predicts perfectly the ignition delay for all cases. The FGM A model cannot reproduce these results, but it yields the same ignition delays as the detailed model with unity Lewis numbers. The

**Table 4.3:** Sensitivity of ignition delay to diffusion flux coefficients, Case D25H<sub>2</sub>.

Diff. Fluxes	$S_{\tau_{ig}}$
$\Lambda_{\zeta,\zeta}$	$2 \times 10^{-4}$
$\Lambda_{\zeta,\gamma}$	$1 \times 10^{-4}$
$\Lambda_{\gamma,\zeta}$	2.86
$\Lambda_{\gamma,\gamma}$	$3 \times 10^{-4}$

FGM B model, predicts ignition delays accurately up to 5% hydrogen addition but the agreement deteriorates with increasing hydrogen content in the fuel. However, the FGM B model improves the predictions significantly compared to the FGM A model.

Comparison of the computed ignition delay of different cases obtained by detailed chemistry in Fig. 4.7, reveals some interesting points. Including preferential diffusion in Case D00H<sub>2</sub> increases ignition delay in contrast to the other cases. This can be explained considering the fact that in Case D00H<sub>2</sub>, there is no hydrogen in the fuel mixture. The effect of hydrogen diffusing into the oxidizer stream is therefore absent. However, during the pre-ignition phase, hydrogen molecules and radicals are formed by chain branching reactions. Due to diffusion effects, these species are diffused away from the most reactive mixture fraction  $\zeta_{MR}$  [Mastorakos, 2009], leading to a decreased reactivity at this location and an increased ignition delay. When non-unity Lewis numbers are applied, the diffusivity of these species (in particular) is enlarged leading to a longer ignition delay. However, for the other cases, hydrogen is present in the fuel mixture. In these cases, the enhanced diffusion of molecular hydrogen from the fuel to  $\zeta_{MR}$  leads to a much higher reactivity and a shorter ignition delay. Therefore, the ignition delay decreases significantly from 0% H<sub>2</sub> to 5% H<sub>2</sub> in the presence of preferential diffusion.

It is interesting to analyze the influence of each of the four preferential diffusion terms in Eqs. 4.13 and 4.14 separately on the predicted autoignition time scales. For this purpose, a sensitivity parameter  $S_{\tau_{ig}}$  is defined as follows:

$$S_{\tau_{ig}} = \frac{\Lambda_{i,j}}{\tau_{ig}} \frac{\partial \tau_{ig}}{\partial \Lambda_{i,j}}. \quad (4.17)$$

To compute the  $S_{\tau_{ig}}$ , quantity of the each diffusion flux coefficient  $\Lambda_{i,j}$  in the manifold is multiplied by 0.5 and then, this manifold is used to compute ignition delays. The sensitivity of ignition delay to each of these diffusion flux coefficients is shown in Table 4.3 for Case D25H<sub>2</sub>. It is clear that ignition delay has the highest sensitivity to  $\Lambda_{\gamma,\zeta}$  while the sensitivity to the other coefficients is nearly zero. This implies that the diffusion of progress variable by a gradient of mixture fraction accounts for the main preferential diffusion effects.

## 4.3 LES of the hydrogen enriched turbulent lifted flames

### 4.3.1 LES formulation and numerical details

The LES formulation of the problem is obtained from the Navier-Stokes equations which are implicitly filtered with the filter width  $\Delta_F$  equal to the mesh size. By application of tabulated chemistry, a set of filtered governing equations is obtained for mass, momentum, mixture fraction and reaction progress [Vreman et al., 2008]:

$$\frac{\partial \bar{\rho}}{\partial t} + \frac{\partial \bar{\rho} \tilde{u}_j}{\partial x_j} = 0 \quad (4.18)$$

$$\frac{\partial(\bar{\rho} \tilde{u}_i)}{\partial t} + \frac{\partial(\bar{\rho} \tilde{u}_i \tilde{u}_j)}{\partial x_j} = \frac{\partial \bar{p}}{\partial x_i} + \frac{\partial}{\partial x_j} \left[ (\mu_L + \mu_T) \left( \frac{\partial \tilde{u}_i}{\partial x_j} + \frac{\partial \tilde{u}_j}{\partial x_i} - \frac{2}{3} \frac{\partial \tilde{u}_k}{\partial x_k} \epsilon_{ij} \right) \right] \quad (4.19)$$

$$\frac{\partial(\bar{\rho} \tilde{\zeta})}{\partial t} + \frac{\partial(\bar{\rho} \tilde{u}_j \tilde{\zeta})}{\partial x_j} = \frac{\partial}{\partial x_j} \left[ \left( \frac{\lambda}{c_p} + \frac{\mu_T}{Sc_T} \right) \frac{\partial \tilde{\zeta}}{\partial x_j} \right] \quad (4.20)$$

$$\frac{\partial(\bar{\rho} \tilde{\mathcal{Y}})}{\partial t} + \frac{\partial(\bar{\rho} \tilde{u}_j \tilde{\mathcal{Y}})}{\partial x_j} = \frac{\partial}{\partial x_j} \left[ \left( \frac{\lambda}{c_p} + \frac{\mu_T}{Sc_T} \right) \frac{\partial \tilde{\mathcal{Y}}}{\partial x_j} \right] + \tilde{\omega}_\mathcal{Y} \quad (4.21)$$

Filtered quantities are specified with an over-line  $\bar{\phi}$  while density-weighted filtered quantities are specified with a tilde  $\tilde{\phi} = \overline{\rho \phi} / \bar{\rho}$ . Solution of the velocity components,  $\tilde{\zeta}$  and  $\tilde{\mathcal{Y}}$  requires values of  $\bar{\rho}$ ,  $\tilde{\omega}_\mathcal{Y}$  and  $c_p$  that are retrieved from the FGM table. It has to be mentioned that additional terms associated with non-unity Lewis numbers are neglected from this formulation since, as it was shown in the previous section, their influence on autoignition time scales is not considerable for the studied cases.  $\mu_L$  and  $\lambda$  are calculated based on simplified formulations following Smooke [1991]:

$$\mu_L / c_p = 1.67 \times 10^{-8} (T/298)^{0.51} \quad (\text{kg}^2 \text{J}^{-1} \text{m}^{-1} \text{s}^{-1}), \quad (4.22)$$

$$\lambda / c_p = 2.58 \times 10^{-5} (T/298)^{0.69} \quad (\text{kgm}^{-1} \text{s}^{-1}). \quad (4.23)$$

The eddy-viscosity  $\mu_T$  is calculated using a model proposed by Vreman et al. [2009] to close nonlinear terms in equations for  $u$ ,  $\zeta$  and  $\mathcal{Y}$ . In this model,  $\mu_T$  is determined by an eddy-viscosity/eddy-diffusivity closure approach in which the eddy-diffusivity  $\mu_T / Sc_T$  is obtained using a fixed turbulent Schmidt number,  $Sc_T = 0.4$ .

Detailed chemistry is modeled by using FGM A and FGM B models which have been extensively discussed in the previous section. The turbulence/chemistry interaction is modeled using a presumed  $\beta$ -PDF method to statistically determine thermo-chemical variables. This model has been successfully used in the previous studies [Vreman et al., 2008; Ramaekers et al., 2012]. In this method, a non-resolved filtered quantity is obtained by  $\bar{\phi} = \int \int \phi(\zeta, c) P(\zeta, c) d\zeta dc$  in which  $P(\zeta, c)$  refers to the joint-PDF.  $c$  refers to the reaction progress  $\mathcal{Y}$  which is normalized between 0 and 1 at unburned and burned mixture, respectively. Complex PDF-closure techniques involve the solution of a large set of transport equations for the probability of possible realizations of the joint-PDF which requires a very large computational time. In this study, due to the high resolution of the grid (approximately 7.5 million cells)

and in order to keep the computational cost low, it is assumed that  $\zeta$  and  $c$  are statistically independent so that the joint PDF can be written by a multiplication of its two marginal PDFs:  $P(\zeta, c) = P(\zeta)P(c)$ . These marginal PDF's are then modeled by a presumed  $\beta$ -PDF that is fully described by its first two moments:  $P(\zeta) = P(\tilde{\zeta}; \tilde{\zeta}, \widetilde{\zeta'^2})$  and  $P(c) = P(\tilde{c}; \tilde{c}, \widetilde{c'^2})$ . This implies that the two-dimensional FGM table is extended with two additional dimensions to accommodate variances of  $\zeta$  and  $c$ . The grid resolution of the PDF-integrated tables is  $(101 \times 11 \times 101 \times 11)$  in the directions of  $(\tilde{\zeta} \times \widetilde{\zeta'^2} \times \tilde{c} \times \widetilde{c'^2})$ . Variances are quadratically clustered near zero where the sensitivity of thermo-chemical variables to changes of variances is significantly larger than at high variances. To determine  $\widetilde{c'^2}$  and  $\widetilde{\zeta'^2}$  during turbulent flame computations, an algebraic gradient model is used, similar to the viscous sub-grid model:

$$\widetilde{\phi'^2} = \alpha \Delta x^2 \left( \frac{\partial \tilde{\phi}}{\partial x_j} \right)^2. \quad (4.24)$$

The value of  $\alpha$  is 1/12 based on the Taylor-expansion of the gradient term in Eq. 4.24. Although the chosen sub-grid models are not the most accurate available model in the literature, it doesn't have a large influence on the predictions due to the present grid resolution which is significantly higher than similar studies [Thme and See, 2011].

The LES model is applied to the DJHC-I case of the DJHC burner, which has been fully described in [Oldenhof et al., 2010; Arteaga et al., 2013]. In this burner, the fuel jet is ignited in the hot coflow of burned gas at low levels of oxygen. The injection of the fuel jet takes place through a fuel pipe ( $D = 4.5$  mm) with a peak velocity of 32 m/s resulting in a jet exit Reynolds number of approximately 4500. The hot coflow stream enters the domain with a bulk velocity of 3 m/s through an annulus of 82.8 mm diameter. The coflow stream is the combustion products of a ring of premixed flames on the secondary burner which are mixed and cooled with the injected ambient air on both sides of the secondary burner. Because of this cooling mechanism, the coflow stream has a non-uniform profile of temperature. In this study, a mass-flux averaged value for temperature and composition of the coflow is used to avoid the need for an extra scalar in our combustion model which is discussed in subsection 4.3.3.

The computational domain is a Cartesian grid of size  $43 \times 43 \times 250$  mm with the largest dimension in the streamwise direction. The grid resolution is chosen as fine as our computational resources allow, in order to minimize numerical and modeling errors. There are approximately 7.5 million grid cells that are distributed non-equidistantly, stretching from the fuel injection point in all three directions. The minimum cell width is 0.375 mm which is less than the laser probe size that has been used to obtain the experimental data. Velocity components,  $\zeta$  and  $\mathcal{Y}$  have homogeneous Neumann boundary conditions at the side planes in both  $x$  and  $y$  direction and at the outflow-plane in  $z$ -direction. For pressure, a Dirichlet ( $p = p_0$ ) boundary condition is applied at the side planes in  $x$  and  $y$  direction while a Neumann boundary condition is applied at the inflow and outflow plane. To account for the intermittency in the inflow velocity of the fuel and oxidizer, a turbulent profile is prescribed using a filtered random noise generator. In this generator, random numbers are applied to each velocity component at the inflow plane at every time-

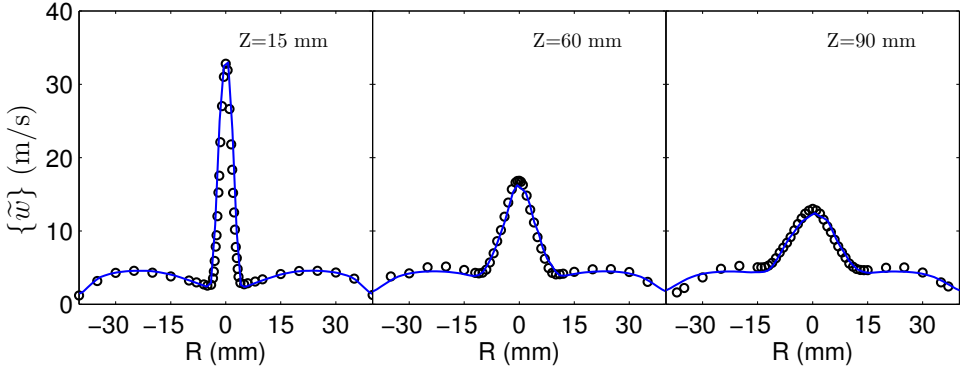


**Figure 4.8:** Radial profiles of (lines) computed and (circles) measured [Oldenhof et al., 2010] mean streamwise velocity at heights  $Z = 15, 60$  and  $90$  for Case D00H<sub>2</sub>.

step. All the velocity components are then spatially filtered using a box-filter with size  $\Delta_F = D/4$  and subsequently with a temporal filter of  $\Delta_T = \Delta t/4$ .

Computations are conducted using an in-house LES solver for which details can be found in [Vreman et al., 2008]. Briefly, the numerical implementation to solve the mathematical model adopts a variable density approach, similar to low-Mach number methods, which involves the solution of a Poisson's equation for the pressure. A standard finite-volume method is used with second order central differencing on a staggered Cartesian mesh. Temporal discretization is based on a third-order Adams-Bashforth for the convective terms and a forward Euler for the viscous terms and source terms. This hybrid time-stepping method provides more stability than pure Adams-Bashforth scheme or pure forward Euler. A constant timestep of  $\Delta t = 0.4 \mu s$  is used for all simulations in order to keep the CFL-number sufficiently low. The scalar equations for  $\zeta$  and  $\mathcal{Y}$  are discretized using third order Van Leer's MUSCLE scheme, which is Total Variation Diminishing (TVD), for convective terms while the viscous terms are discretized using second order central differencing. The code adopts a multi-grid implementation to solve the Poisson's equation. Parallelization has been performed using a combined MPI and OpenMP protocols on a multi-block platform.

### 4.3.2 Flow field statistics

Comparison of predicted mean streamwise velocity  $\{\tilde{w}\}$  with measurements at several heights is shown in Fig. 4.8. The mean values are calculated based on ensemble averaging of density-weighted velocity. It is observed that  $\{\tilde{w}\}$  of fuel jet in the middle of the domain, is significantly larger than  $\{\tilde{w}\}$  of coflow which creates velocity fluctuations and turbulence in the shear layer between these two streams. The computed RMS values of velocity components,  $\{\widetilde{w'^2}\}^{1/2}$  and  $\{\widetilde{u'^2}\}^{1/2}$ , on the centerline is compared with measurements in Fig. 4.9. The RMS values which indicates

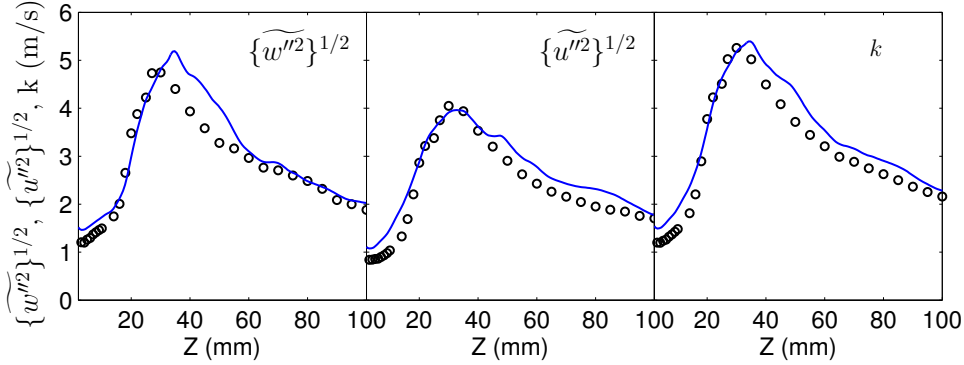


**Figure 4.9:** Centerline profiles of (lines) computed and (circles) measured [Oldenhof et al., 2010] RMS of streamwise velocity, RMS of spanwise velocity and turbulence kinetic energy ( $k = 1/2(\{\widetilde{w''^2}\}^{1/2} + 2\{\widetilde{u''^2}\}^{1/2})$ ) for Case D00H<sub>2</sub>.

standard deviation is calculated from

$$\{\widetilde{w''^2}\}^{1/2} = \left[ \sum_{i=1}^n \frac{\widetilde{w}_i^2}{n} - \left( \sum_{i=1}^n \frac{\widetilde{w}_i}{n} \right)^2 \right]^{1/2} \quad (4.25)$$

$i$  and  $n$  refer to the number of instant and total number of instants, respectively. It is observed that at a height of approximately 30 mm, the RMS values of velocity and the resulted turbulence kinetic energy reach their maximum value. The turbulence kinetic energy and RMS values decay at higher heights.

For both mean and RMS quantities, there is a good agreement between the computations and measurements. It is clear that application of the random noise generator reproduces successfully the inflow turbulence of the experiments. It has to be mentioned that such an accurate prediction of the flow field is an essential step prior to any combustion modeling effort. The grid resolution is evaluated at the location where the turbulence kinetic energy has the highest value (approximately at  $Z = 30$  mm) and a wide range of scales is available in the flow field. Temporal analysis of the velocity signal at this location yields a power spectrum which is plotted in Fig. 4.10. It is observed that the inertial sub-range of the spectrum corresponds to the theoretical slope of  $-5/3$  which is a criterion for the fine resolution of the numerical grid.

### 4.3.3 Influence of preferential diffusion on the lift-off height

Figure 4.11 shows instantaneous snapshots of the filtered OH mass fraction  $\widetilde{Y}_{OH}$  which is obtained from the LES of Case D00H<sub>2</sub> with FGM B model. It is observed that at  $t = 96$  ms, a  $\widetilde{Y}_{OH}$  kernel is formed at approximately  $Z = 200$  mm. Subsequently, this kernel grows and convects downstream at  $t = 100$  ms and  $t = 104$  ms. This mechanism, which is repeated in subsequent times, governs stabilization

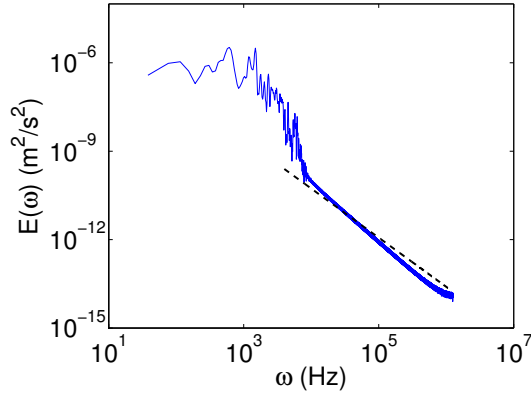


**Figure 4.10:** Computed power spectrum using temporal velocity signal on the centerline at  $Z = 30$  for Case D00H<sub>2</sub>. Dashed line represents the theoretical  $-5/3$  law.

of the flame. At far downstream location, these kernels further grow and ignite the surrounding mixture. It is apparent that this flame is stabilized by autoignition in which ignition kernels are formed, grow and convect downstream corresponding to experimental observations by Oldenhof et al. [2010]. These ignition events are formed at the lean side ( $\zeta < \zeta_{st}=0.0178$ ) very close to the oxidizer stream where molecular diffusion is comparable with turbulence transport (eddy viscosity).

Such a stabilization mechanism is further clarified by plotting 3D iso-surfaces of  $\tilde{\zeta}_{st} = 0.0178$  and  $\tilde{\mathcal{Y}} = 2.9$  in Fig. 4.12. At these values of  $\tilde{\zeta}$  and  $\tilde{\mathcal{Y}}$ , source term of  $\tilde{\mathcal{Y}}$  approaches to its maximum value (cf. Fig. 4.5) which is an indication of autoignition. Considering this, in Fig. 4.12, autoignition initiates from small spots at an axial distance from the jet exit. Afterwards, these spots grow and ignite the downstream mixture.

In order to investigate the influence of hydrogen addition on such a flame structure, snapshots of  $\tilde{Y}_{OH}$  are plotted for Case D10H<sub>2</sub> in Fig. 4.13. In this case, OH forms right after the jet exit which indicates a totally different structure than the one observed for Case D00H<sub>2</sub>. The structure of Case D10H<sub>2</sub> corresponds to experimental observations of OH chemiluminescence by Arteaga et al. [2013]. This structure resembles an edge flame structure which is stabilized by a flame propagation mechanism, in clear contrast with the autoignition structure of Case D00H<sub>2</sub>. Further analysis of the flame stabilization of the studied cases is discussed in the following subsection.

Figure 4.14 shows the time-averaged  $\{\tilde{Y}_{OH}\}$  distributions obtained from the statistics of approximately 10 through flow times of the fuel jet. These plots are shown for all studied cases using FGM A and FGM B models. Computations with FGM A result in approximately the same lift-off height for cases D00H<sub>2</sub>, D05H<sub>2</sub> and D10H<sub>2</sub>. However, computations with FGM B indicate a significant change of the lift-off height among these cases especially between cases D00H<sub>2</sub> and D05H<sub>2</sub>. For Case D25H<sub>2</sub>, FGM B yields an attached flame to the jet exit. These observations demonstrate that preferential diffusion has a strong influence on the stabilization



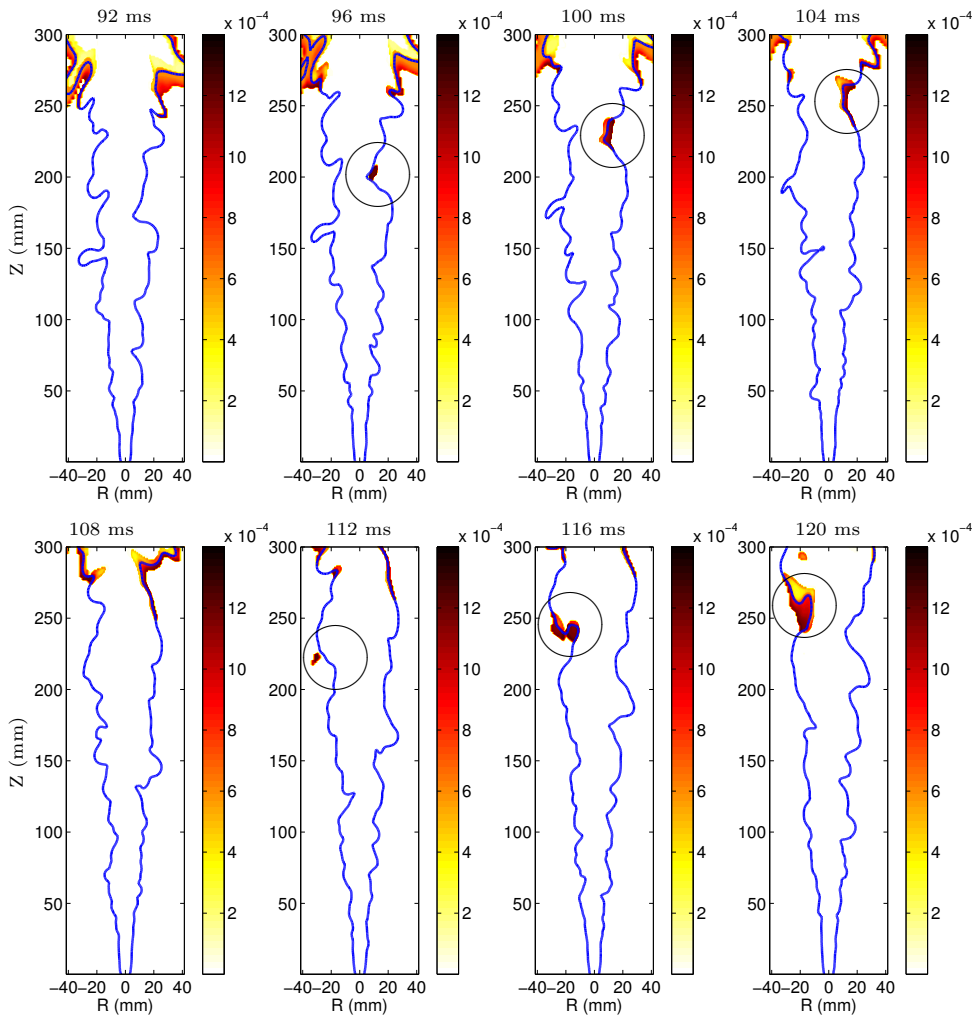


**Figure 4.11:** Computed instantaneous snapshots of  $\tilde{Y}_{OH}$  using FGM B model for Case D00H<sub>2</sub>. Blue lines indicate stoichiometric mixture fraction  $\zeta_{st}$ .

height and mechanism of the studied flames.

The time-averaged plots in Fig. 4.14 are compared with the measurements represented by red lines. These lines show the measured 50% probability of OH chemiluminescence (more details can be found in [Arteaga et al., 2013]). Comparison of the  $\{\tilde{Y}_{OH}\}$  plots with the red lines demonstrates that, except for Case D00H<sub>2</sub>, formation of OH is captured very well with the FGM B model. However, FGM A yields considerably higher lifted flames compared to the measurements. This demonstrates that inclusion of preferential diffusion in the combustion model is essential for hydrogen-enriched cases. In cases D10H<sub>2</sub> and D25H<sub>2</sub>, formation of OH is captured at

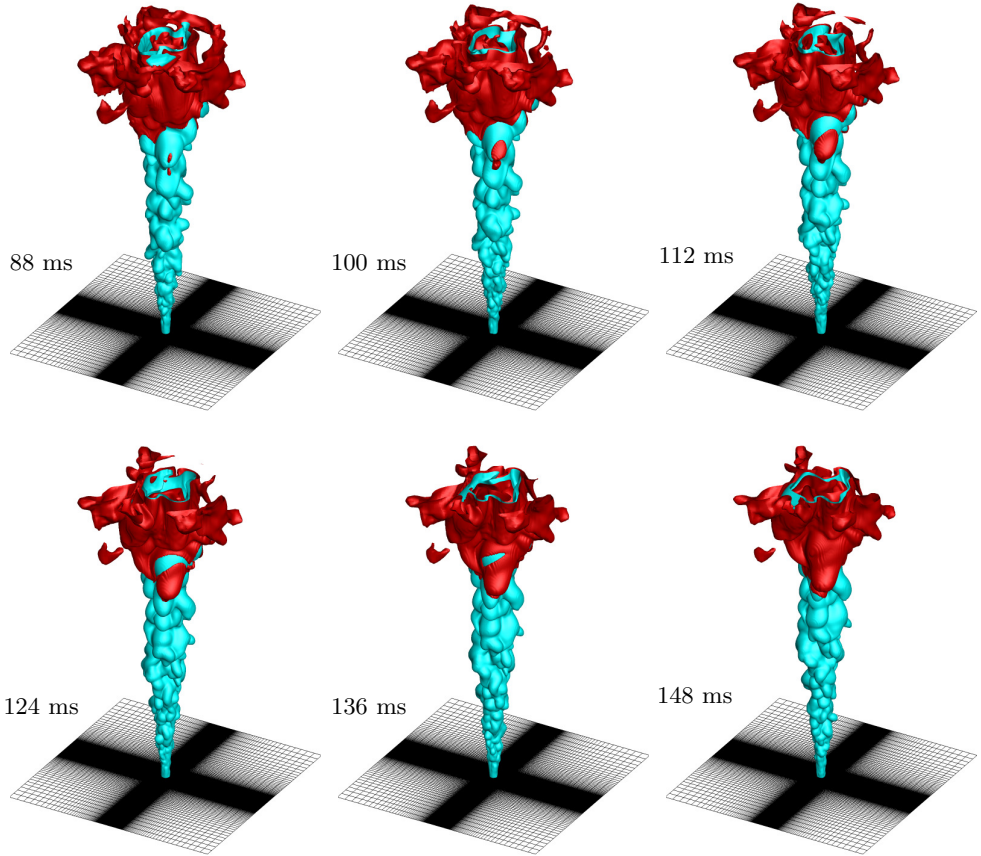


**Figure 4.12:** Computed instantaneous iso-surfaces of  $\tilde{\zeta}_{st} = 0.0178$  (blue) and  $\tilde{Y} = 2.9$  (red) using FGM B model for Case D00H<sub>2</sub>.

somewhat smaller heights than the red lines. This can be explained considering the fact that our computation does not take into account heat loss effects leading to a uniform distribution of the inflow temperature at the coflow side. Such a uniform distribution results in a higher temperature, compared to measurements, at close vicinity of the jet exit. This condition for the cases with small lift-off heights (cases D10H<sub>2</sub> and D25H<sub>2</sub>) leads to a faster ignition and consequently lower lift-off heights. The heat loss can be added to our combustion model by inclusion of at least one extra scalar. However, inclusion of an extra scalar adds its related uncertainties and computational cost due to an increased size of the FGM table and an additional transport equation. Such an extension is usually accomplished at the expense of using a FGM table with lower resolution and a numerical grid which is coarser. This scalar is not included in our model to keep the resolution of FGM table and the numerical grid as high as possible within the availability of our computational

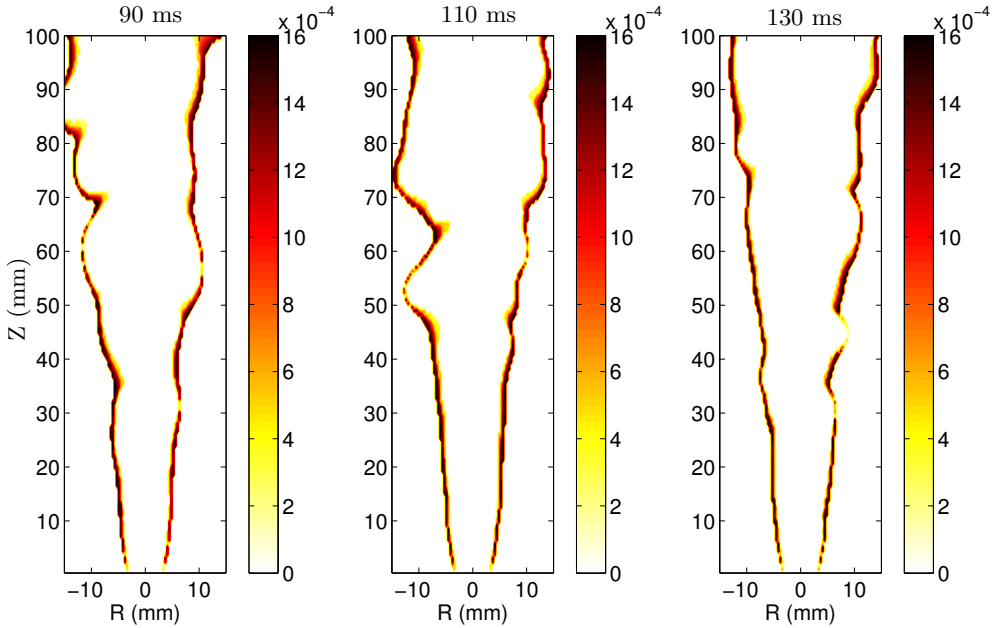


**Figure 4.13:** Computed instantaneous snapshots of  $\tilde{Y}_{OH}$  using FGM B model for Case D10H<sub>2</sub>.

resources in order to focus on preferential diffusion effects. The extension of our model to heat loss effects remains as a future study.

It is interesting to compare lift-off heights of these turbulent flames with the ignition delays of IML-flamelets that were shown in Fig. 4.7. It is clear that the lift-off heights follow a very similar trend to the ignition delays. In particular, for Case D00H<sub>2</sub>, the ignition delay computed using FGM B model is larger than that of FGM A model. This trend corresponds very well with the higher lift-off height of the computed flame (Case D00H<sub>2</sub>) using FGM B model compared to the one using FGM A model. Accordingly, the significant change of ignition delay between Case D00H<sub>2</sub> and D05H<sub>2</sub> by application of FGM B model complies very well with the predicted lift-off heights of these cases by using this FGM model. These observations indicate that these turbulent flames behave very similar to laminar flames. This can be explained considering that, as mentioned earlier, ignition of these flames is initiated at very small mixture fractions ( $\zeta < \zeta_{st}=0.0178$ ) very close to the oxidizer side. In this region, turbulent structures in the fuel stream can hardly intrude the ignition kernels at the most reactive mixture fraction  $\zeta_{MR}$  which induces that molecular diffusion is comparable with turbulence transport. Another reason is related to the Reynolds number of these cases which is not very large ( $Re = 4500$ ) compared to highly turbulent flows.

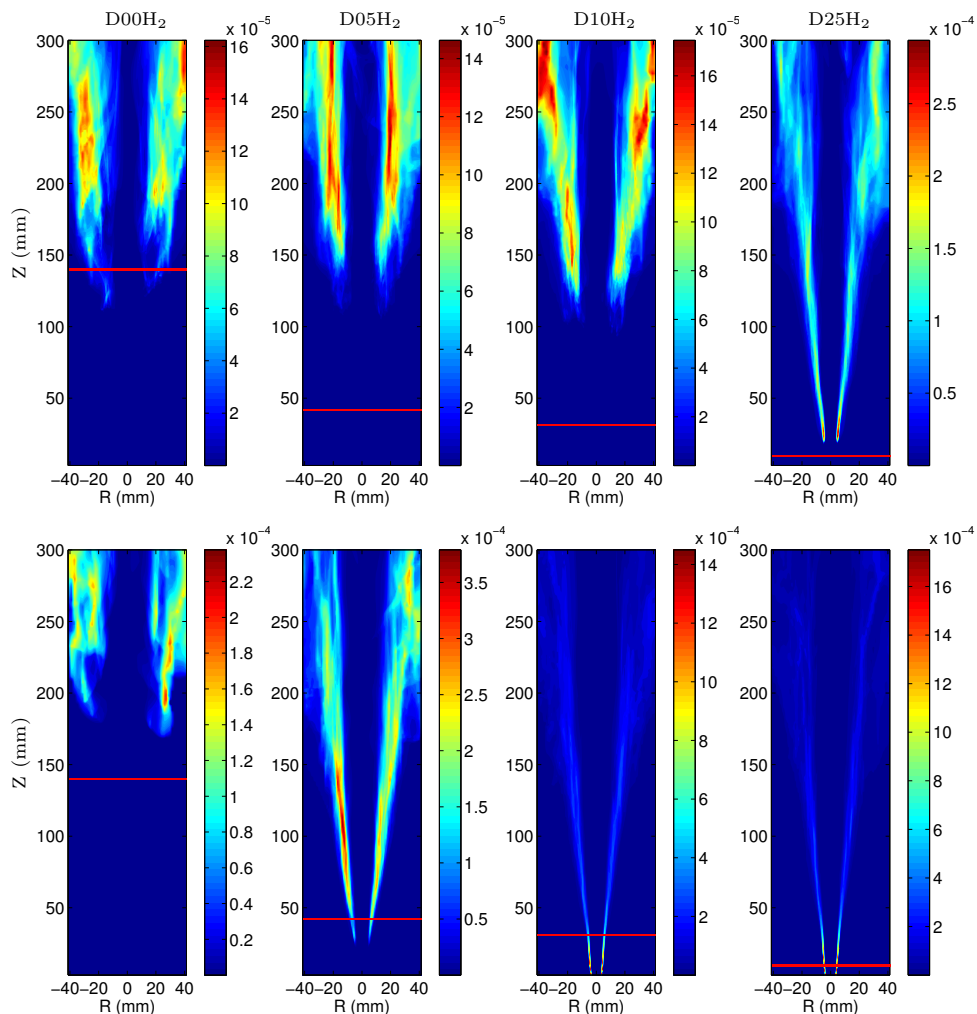


**Figure 4.14:**  $\{\tilde{Y}_{OH}\}$  for all cases (from left to right D00H<sub>2</sub>, D05H<sub>2</sub>, D10H<sub>2</sub> and D25H<sub>2</sub>). Computations with (top) FGM A model and (bottom) FGM B model. Red lines correspond to 50% probability of OH chemiluminescence by measurements [Arteaga et al., 2013].

#### 4.3.4 Stabilization mechanism of lifted flames

In the previous subsection, based on instantaneous  $\tilde{Y}_{OH}$  distributions, a clear formation of ignition kernels has been observed for Case D00H<sub>2</sub> and for D05H<sub>2</sub> (not shown). However, the stabilization mechanism of Case D10H<sub>2</sub> and D25H<sub>2</sub> in which the fuel jet immediately burns after injection into the domain, is not completely clear. This motivates us to further investigate the stabilization mechanism of the flames by turning off the autoignition chemistry in our combustion model (setting  $\tilde{\omega}_y = 0$  at the beginning of reaction progress  $\tilde{c} = 0$ ) and restarting the simulations

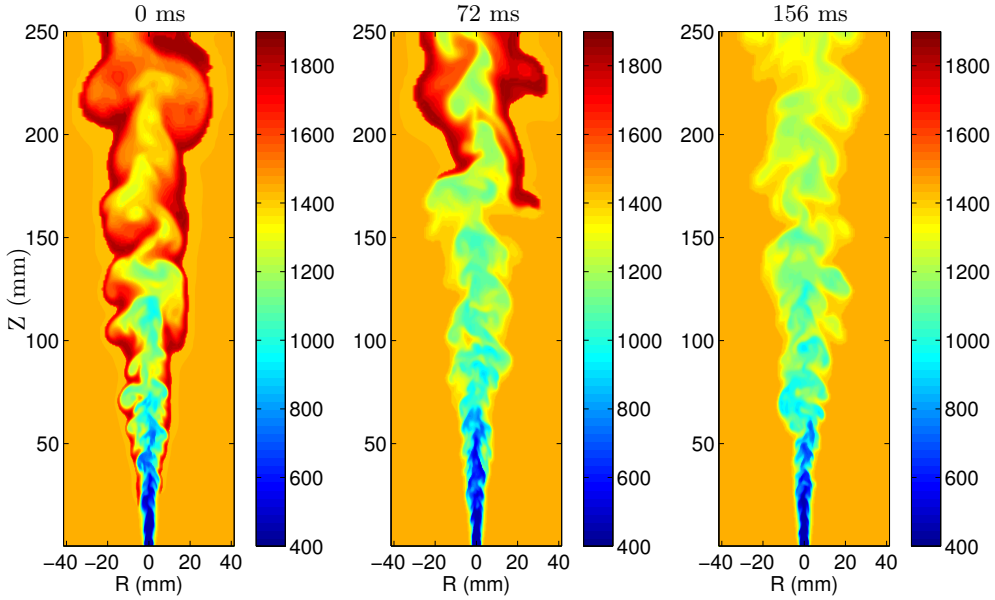


**Figure 4.15:** Computed instantaneous distributions of  $\tilde{T}$  using FGM B model without ignition chemistry for Case D05H<sub>2</sub>.

from an already burning state. In this case, ignition kernels cannot form and the flame is stabilized only if there is a propagating flame structure. Cases D00H<sub>2</sub> and D05H<sub>2</sub> are blown off as it is shown for Case D05H<sub>2</sub> in Fig. 4.15. However, the two other cases (D10H<sub>2</sub> and D25H<sub>2</sub>) remained burning as before. This observation demonstrates that autoignition is the main stabilization mechanism of Case D00H<sub>2</sub> and D05H<sub>2</sub>, while the two other cases are stabilized by flame propagation.

## 4.4 Conclusions

In the first section, a numerical study has been carried out to develop a flamelet-based technique to incorporate preferential diffusion effects in autoigniting flames. Such a development was found unavoidable because investigations with detailed chemistry revealed that preferential diffusion affects strongly the autoignition time scales of H<sub>2</sub>-enriched mixtures. IML-flamelets were proposed as an adequate flamelet configuration in order to include preferential diffusion effects in molecular mixing and autoignition of the flamelets. IML-flamelets with different transport models were tabulated using mixture fraction and reaction progress. Transport equations for these controlling variables have been derived with extra terms in order to take into account preferential diffusion. Predictions of autoignition time scales by FGM C model, which includes preferential diffusion effects in the flamelet database and transport equations, agree very well with detailed chemistry for all studied cases. A

sensitivity study revealed that diffusion of the progress variable caused by a gradient of mixture fraction, is the most important preferential diffusion term in the transport equations for the controlling variables. Simplified implementations of the FGM model were investigated. It was found that ignoring the preferential diffusion terms in the transport equations (FGM B model) leads to significant deviations for cases with high  $H_2$  levels. However, for small amounts of hydrogen (5% or less), a good agreement was found with detailed simulations and significant improvement was observed compared to the case in which preferential diffusion effects were ignored in both the transport equations and in the table generation (FGM A model). Finally, it can be concluded that the developed FGM methodology predicts accurately preferential diffusion effects in autoigniting flames and that it is a promising method to be used in simulations of lifted flames on, for instance, the DJHC burner.

Afterwards, LES of the turbulent lifted flames has been performed using FGM A and FGM B models. A four dimensional flamelet database ( $\tilde{\zeta} \times \tilde{\zeta}^{1/2} \times \tilde{c} \times \tilde{c}^{1/2}$ ) has been generated for each studied case in which variances computed with  $\beta$ -PDF approximation. The DJHC burner has been chosen as a test case in which the fuel has been enriched with various amounts of hydrogen. Comparison of the mixing field between computations and experiments indicates a good agreement. It is found that the influence of preferential diffusion on the stabilization height of the 0% $H_2$  case is not significant. In this case, both FGM A and FGM B models yield a reasonable prediction of the lift-off height compared to measurements. However, preferential diffusion affects strongly lift-off height of hydrogen enriched cases, especially the 5% $H_2$  case compared to the 0% $H_2$  case. This trend is not captured using the FGM A model, which yields approximately the same lift-off height for 0% $H_2$ , 5% $H_2$  and 10% $H_2$  cases. Comparison of all studied cases with the measured OH chemiluminescence demonstrates the necessity of inclusion of preferential diffusion in the combustion model (FGM B) for hydrogen containing cases (5% $H_2$ , 10% $H_2$  and 25% $H_2$ ). Further analysis of computational results reveal that the 0% $H_2$  and 5% $H_2$  cases are stabilized by autoignition in which there are distinct formation of ignition kernels which they grow and convect downstream afterwards. On the other hand, 10% $H_2$  and 25% $H_2$  cases are stabilized by a propagation mechanism without ignition kernels. These observations are in a good agreement with the measured instantaneous snapshots of OH chemiluminescence. Therefore, it can be concluded that hydrogen enrichment leads to a significant change in the lift-off height and stabilization mechanism of the turbulent lifted flames. There is an underprediction of lift-off heights for the 10% $H_2$  and 25% $H_2$  cases using the FGM B model which can be explained due to application of a mass-flux averaged value for the temperature of the coflow. As a future study, predictions can be further improved by addition of at least one extra scalar to the proposed model in order to take into account heat loss effects.



# Conclusions and outlook

## 5.1 Conclusions

In this thesis, numerical investigations have been carried out to understand underlying physics of Mild combustion and to develop models for simulations of Mild burners. In spite of the great potential of this combustion regime to decrease NO formation and to increase thermal efficiency, its application is mainly limited to laboratory scale burners due to several issues. Conditions of low temperature levels and low oxygen concentrations of this combustion regime lead to slow reaction rates. This raises many issues on flame stabilization, autoignition and structure of the reaction zone near the jet exit. A fundamental understanding of the underlying processes helps us to resolve these issues and to adopt this combustion technology in industrial applications.

One of the issues is the flame structure and autoignition of Mild combustion for different cases in which burned gas is entrained into fuel and/or oxidizer stream(s). To investigate this, one-dimensional counterflow diffusion flames are chosen because of their relatively simple configuration which permits conduction of a large number of computations using detailed schemes at a reduced computational cost. Several attractive characteristics of Mild combustion are observed for all cases, for instance, low peak temperatures of the reaction zone and accordingly low  $\text{NO}_x$  formation. Analysis of NO formation reveals that in Mild combustion, NO is mainly formed via the Fenimore mechanism (prompt NO), in contrast to the Zeldovich mechanism (thermal NO) which is the main route of NO formation in most combustion systems. Increasing of the burned gas entrainment leads to a decrease in ignition delay for all cases due to an increased temperature of the reactants. Increasing strain rate delays autoignition for all investigated cases. At sufficiently high degree of preheating and dilution, the shortest ignition delay is found for the case in which the burned gas is entrained into both fuel and oxidizer streams.

Moving toward a more realistic configuration, 2D axisymmetric laminar coflow diffusion flames are studied to investigate local flame front characteristics and stabilization mechanism of these flames. These flames make it possible to perform detailed and accurate computations and experiments due to their relatively simple geometry, steadiness and optical accessibility. Several coflow flames have been studied in their transition from the “standard” condition to Mild combustion regime by increasing preheating and dilution of reactants. Computations are performed us-



ing detailed chemistry GRI-Mech 3.0, a mixture-averaged multicomponent transport and an optically thin approximation for radiative heat losses. The computational model predicts perfectly experiments. This demonstrates the capability of GRI-Mech 3.0 scheme for simulations of Mild combustion. Simplification of the computational model by assuming constant Schmidt numbers yields worse predictions on the center-line of the coflow. Radiative losses appear to be insignificant at lower axial distances; however, their effect becomes increasingly important at higher axial distances.

Analysis of the computational results reveals that the stabilization mechanism of the “standard” laminar coflow flames occurs by an edge flame while the Mild flame stabilizes by autoignition. Analysis of NO formation reveals that the Fenimore mechanism is the major route of NO formation in the Mild flame. These observations correspond with the conclusions of the 1D counterflow flames. A reduction of the seeded NO is observed for the Mild flame at some axial distances. It is revealed that the reduction is due to the conversion of the NO molecules to the N-containing intermediates. These intermediates are converted back to NO at downstream distances. Fuel flexibility of the Mild flame to alternative fuels such as syn-gas has been evaluated by the enrichment of the fuel stream with hydrogen. Addition of hydrogen decreases the Mild flame’s lift-off height while the stabilization mechanism and NO formation are not considerably changed.

In turbulent situations, a novel numerical model has been proposed in order to simulate turbulent lifted flames of  $\text{CH}_4/\text{H}_2$  mixtures in a hot and diluted environment. These lifted flames have been experimentally investigated in the Delft Jet-in-Hot Coflow (DJHC) burner for 0%, 5%, 10% and 25% of  $\text{H}_2$  in the methane base fuel. The Flamelet Generated Manifolds (FGM) technique has been adopted and extended for autoignition of hydrogen enriched mixtures. First analysis with detailed chemistry reveals that preferential diffusion has a strong influence on autoignition time scales. Igniting Mixing Layer flamelets (IML-flamelets) were proposed as a suitable flamelet configuration to capture preferential diffusion effects on autoignition and to create a flamelet database. Transport equations for controlling variables have been derived in order to take into account preferential diffusion effects. It was observed that predictions using FGM C model, which includes preferential diffusion effects in the flamelet database and transport equations, agree very well with detailed chemistry for all studied cases. Simplified implementations of the FGM C model have also been investigated. It was found that ignoring the preferential diffusion terms in the transport equations (FGM B model) leads to significant deviations for cases with high  $\text{H}_2$  levels. However, for small amounts of hydrogen (5% or less), a good agreement was found with detailed simulations. A significant improvement was observed by using FGM B model compared to the case in which preferential diffusion effects were ignored in both the transport equations and in the table generation (FGM A model).

LES of the turbulent lifted flames has been performed for all hydrogen enriched cases (0%, 5%, 10% and 25% of  $\text{H}_2$ ) using FGM A and FGM B models. Predictions of the mixing field indicate a good agreement with measurements of velocity. It appeared that for the 0% $\text{H}_2$  case, preferential diffusion effects are not significant yielding a reasonable prediction of the lift-off height by using both FGM models. However, preferential diffusion affects strongly lift-off height of hydrogen enriched

cases, especially the 5% $H_2$  case compared to the 0% $H_2$  case yielding much improved predictions by using FGM B model compared to FGM A model. This demonstrates the necessity of inclusion of preferential diffusion in the combustion model (FGM B) for hydrogen containing cases. Analysis of computational results reveals that 0% $H_2$  and 5% $H_2$  cases are stabilized by autoignition in which there is a distinct formation of ignition kernels, which form, grow and convect downstream. On the other hand, 10% $H_2$  and 25% $H_2$  cases are stabilized by flame propagation without ignition kernels. Therefore, it can be concluded that hydrogen enrichment leads to a significant change in the lift-off height and stabilization mechanism of the turbulent lifted flames. These observations are in a good agreement with the measured instantaneous snapshots of OH chemiluminescence.

## 5.2 Discussions and future recommendations

In turbulent non-premixed combustion systems, mixing occurs by molecular diffusion and turbulence transport. The conventional turbulent non-premixed devices are mainly designed in such a way that chemistry occurs much faster than mixing. Therefore, the rate of mixing is the determining rate of the flame stabilization, for which they are often called mixing-controlled. In the mixing-controlled systems, turbulence transport is much larger than molecular diffusion and therefore the whole combustion process is controlled by turbulence transport. However, according to the conclusions of this thesis, the turbulent lifted flames share very similar characteristics with the laminar coflow diffusion flames. In both flames, the molecular transport and preferential diffusion play an important role in the lift-off heights. This behavior is somewhat different than what has been observed for the conventional non-premixed systems and can be explained by several reasons. First, at slow reaction rates of Mild combustion, the mixing and chemistry occurs at comparable time scales which increases importance of reaction kinetics and consequently molecular diffusion on the flame structure. Second, because of an intense dilution of the coflow stream of the lifted flames, most reactive mixture fraction  $\zeta_{MR}$  is shifted very close to the oxidizer stream due to the lack of available oxygen for oxidation. This location, in which ignition kernels are formed, can be hardly perturbed by turbulent structures in the fuel stream which enhances the importance of molecular diffusion. Third, the Reynolds numbers of the studied turbulent flames are not very high ( $Re=4500$ ) which causes that these flames inherit laminar flame characteristics. Finally, the effect of molecular diffusion becomes more apparent by application of hydrogen containing fuels, which introduces a substantial preferential diffusion effects.

Several developments can be made in the proposed model in order to be applied for a wider range of applications. In this study, the influence of the sub-grid scale models kept in the minimum level due to the application of highly refined meshes. However, decreasing mesh resolution might yield worse predictions due to a larger influence of sub-grid scale modeling. In this case, more complex models are required for an improved accuracy. For instance, variances of controlling variables in the LES can be computed by solving a set of transport equations instead of assuming a gradient approximation model. Computations of variances in the flamelet database

using a  $\beta$ -PDF approximation can be substituted with the transported PDF approach which might yield an improved shape of PDF at the expense of an increased computational cost.

In addition to the modeling efforts, there remain several physical investigations that can consolidate our understanding of Mild combustion in turbulent situations. In this study, a uniform scalar has been assumed for the inflow temperature and oxygen concentration of the coflow in order to focus on preferential diffusion effects as much as computational resources allow. Addition of at least one extra controlling variable in the model can take such non-homogeneous boundary conditions into account. This becomes particularly interesting considering that in the experiments of the DJHC burner, it has been observed that increasing Reynolds numbers (up to 8800) leads to a decreased lift-off height. This observation has been explained due to the non-homogeneous distribution of temperature and species at the inflow boundary. Computations of these cases help us to understand complex underlying processes of this observation.

In our simulations of the lifted flames, entrainment of ambient air into the coflow stream is neglected which can affect predictions of the reaction zone at large axial distances. Inclusion of this effect can be particularly important, if the purpose of study is to investigate formation of pollutants such as  $\text{NO}_x$  or soot. This can be implemented in our numerical model by introducing an additional controlling variable to account for the third stream (ambient air).

In this study, the effect of  $\text{H}_2$  addition to the methane base fuel was studied to evaluate flexibility of Mild combustion to alternative fuels such as syn-gas. However, other alternative fuels such as bio-gas contain a considerable amounts of  $\text{CO}_2$  which has been experimentally investigated in the DJHC burner. Computations of this case can be performed by application of the proposed model. For an increased accuracy, the non-homogeneous boundary condition and the third stream can be implemented in the model using additional dimensions in the FGM methodology.

In real furnaces, conditions might be quite different from those in the JHC burners. For instance, Reynolds numbers might be larger which can increase turbulence intensities. Furthermore, entrainment of burned gas into the fuel stream, as it was discussed in chapter 2, shifts most reactive mixture fraction toward the fuel stream. In this condition, turbulent structures have a larger impact on ignition events resulting in an increased role of turbulence transport with respect to molecular diffusion. In the future research, experimental and numerical investigations of these conditions are indispensable in order to move toward more practical situations.

# References

- [Abtahizadeh et al., 2012] E. Abtahizadeh, J. van Oijen, P. de Goey, *Combust. Flame*, 159 (2012) 2155-2165. *Cited on pages 30, 31, 47, 51, and 64.*
- [Abtahizadeh et al., 2013] E. Abtahizadeh, A.V. Sepman, J. van Oijen, A.V. Mokhov, P. de Goey, H.B. Levinsky, *Combust. Flame*, 160 (2013) 2359-2374. *Cited on page 32.*
- [Arteaga et al., 2013] L.D.A. Arteaga, M.J. Tummers, D.J.E.M. Roekaerts, *Effect of hydrogen on the stabilization mechanism of natural gas jet-in-hot-coflow flames*, Proceedings of the 6th European Combustion Meeting, Sweden, 2013, P1-16. *Cited on pages 6, 65, 76, 78, 90, 93, 94, and 97.*
- [Ayoub et al., 2012] M. Ayoub, C. Rottier, S. Carpentier, C. Villermaux, A.M. Boukhalfa, D. Honore, *Int. J. Hydrogen Energy* 37 (2012) 6912-21. *Cited on page 31.*
- [Barlow and Frank, 2003] R.S. Barlow, J. Frank, *Piloted CH<sub>4</sub>/air flames C, D, E and Frelease 2.0*. Technical report, Sandia National Laboratories (2003). *Cited on page 77.*
- [Bekdemir et al., 2013] C. Bekdemir, L.M.T. Somers, L.P.H. de Goey, J. Tillou, C. Angelberger, *Proc. Combust. Inst.*, 34 (2013) 3067-3074. *Cited on pages 7, 77, and 79.*
- [Bennett et al., 2000] B.A.V. Bennett, C.S. McEnally, L.D. Pfefferle, M.D. Smooke, *Combust. Flame* 123 (4) (2000) 522-546. *Cited on page 30.*
- [Bilger, 1988] R.W. Bilger, *Proc. Combust. Inst.* 22 (1988) 475-488. *Cited on pages 13, 45, 50, 59, 69, and 83.*
- [Bongers, 2005] H. Bongers, *Analysis of flamelet-based methods to reduce chemical kinetics in flame computations*, PhD thesis, Eindhoven University of Technology, Eindhoven, The Netherlands, 2005. *Cited on page 6.*
- [Bowman et al., 1995] C.T. Bowman, R.K. Hanson, D.F. Davidson, W.C. Gardiner, V. Lissianski, G.P. Smith, D.M. Golden, M. Frenklach, M. Goldenberg, *GRI-Mech 2.11*. [Available at <http://www.me.berkeley.edu/gri-mech/>] (1995). *Cited on page 14.*

- [Buckmaster, 2002] J. Buckmaster, *Prog. Energy Combust. Sci.* 28 (2002) 435-475. *Cited on page 46.*
- [Bykov and Maas, 2007] V. Bykov, U. Maas, *Proc. Combust. Inst.*, 31 (2007) 465-472. *Cited on page 76.*
- [Cabra et al., 2002] R. Cabra, T. Myhrvold, J.Y. Chen, R.W. Dibble, A.N. Karpetis, R.S. Barlow, *Proc. Combust. Inst.* 29 (2002) 1881-1888. *Cited on page 26.*
- [Cabra et al., 2005] R. Cabra, J.Y. Chen, R.W. Dibble, A.N. Karpetis, R.S. Barlow, *Combust. Flame* 143 (2005) 491-506. *Cited on pages 6, 26, 76, and 77.*
- [Carbonell et al., 2009] D. Carbonell, C. Perez-Segarra, P. Coelho, A. Oliva, *Combust. Flame* 156 (2009) 334-347. *Cited on page 30.*
- [Cavaliere and Joannon, 2004] A. Cavaliere, M. de Joannon, *Prog. Energy Combust. Sci.* 30 (2004) 329-366. *Cited on pages 3 and 4.*
- [Charest and Groth, 2010] M.R.J. Charest, C.P.T. Groth, and Ö.L. Gülder, *Combust. Theory Modelling*, 14 (2010) 793-825. *Cited on page 34.*
- [Choi and Katsuki, 2002] G. Choi, M. Katsuki, *Proc. Combust. Inst.* 29 (2002) 1165-1171. *Cited on pages 11, 26, 30, and 46.*
- [Christo and Dally, 2005] F.C. Christo, B.B. Dally, *Combust. Flame* 142 (2005) 117-29. *Cited on pages 7, 30, and 77.*
- [Claramunt et al., 2006] K. Claramunt, R. Consul, D. Carbonell, C.D. Perez-Segarra, *Combust. Flame* 145 (2006) 845-862. *Cited on page 30.*
- [Coelho and Peters, 2001] P.J. Coelho, N. Peters, *Combust. Flame*, 124 (2001) 503-518. *Cited on pages 7 and 77.*
- [Coirier, 1994] W.J. Coirier, PhD thesis, University of Michigan, 1994. *Cited on page 34.*
- [Consul et al., 2008] R. Consul, A. Oliva, C.D. Perez-Segarra, D. Carbonell, L. de Goeij, *Combust. Flame* 153 (2008) 71-83. *Cited on page 30.*
- [Dagaut et al., 2000] P. Dagaut, J. Luche, M. Cathonnet, *Proc. Combust. Inst.* 28 (2000) 2459-2465. *Cited on page 58.*
- [Dally et al., 2002] B.B. Dally, A.N. Karpetis, R.S. Barlow, *Proc. Combust. Inst.* 29 (2002) 1147-54. *Cited on pages 6, 10, 30, 31, 76, and 77.*
- [Dally et al., 2004] B.B. Dally, E. Riesmeier, N. Peters, *Combust. and Flame*, 137 (2004) 418-431. *Cited on page 11.*
- [de Swart et al., 2010] J.A.M. de Swart, R.J.M. Bastiaans, J.A. van Oijen, L.P.H. de Goeij, R.S. Cant, *Flow, Turb. Combust.*, 85 (2010), 473-511. *Cited on pages 7 and 76.*

- [Delhaye et al., 2009] S. Delhaye, L.M.T Somers, J.A. van Oijen, L.P.H. de Goey, Proc. Combust. Inst., 32 (2009) 1051-1058. *Cited on page 7.*
- [Dixon-Lewis, 1968] Dixon-Lewis, Proc. Roy Soc. A., 307 (1968) 111-135. *Cited on page 13.*
- [Domingo et al., 2008] P. Domingo, L. Vervisch, D. Veynante, Combust. Flame 152 (2008) 415-432. *Cited on page 81.*
- [EIA, 2013] Energy Information Administration, International Energy Outlook 2013, <http://www.eia.gov/forecasts/ieo/>. *Cited on pages 1 and 2.*
- [Frassoldati et al., 2010] A. Frassoldati, P. Sharma, A. Cuoci, T. Faravelli, E. Ranzi, Appl. Therm. Eng. 30 (2010) 376-383. *Cited on page 30.*
- [Galletti et al., 2009] C. Galletti, A. Parente, M. Derudi, R. Rota, L. Tognotti, Int. J. Hydrogen Energy 34 (2009) 8339-51. *Cited on page 31.*
- [Gao and Groth, 2010] X. Gao and C.P.T. Groth, J. Comput. Phys., 229 (2010) 3250-3275. *Cited on page 34.*
- [Gao et al., 2011] X. Gao, S.A. Northrup, and C.P.T. Groth, Prog. Comput. Fluid Dyn., 11 (2011) 76-95. *Cited on page 34.*
- [Gicquel et al., 2000] O. Gicquel, N. Darabiha, D. Thevenin, Proc. Combust. Inst., 28 (2000) 1901-1908. *Cited on page 77.*
- [Glassman, 1987] I. Glassman, *Combustion*, 2nd ed. Academic press (1987). *Cited on page 20.*
- [Goodwin, 2003] D.G. Goodwin, Chemical Vapor Deposition XVI and EUROCVI 14 (2003) 155-162. *Cited on page 34.*
- [Gordon et al., 2008] R. L. Gordon, A. R. Masri, E. Mastorakos, Combust. and Flame 155 (2008) 181-195. *Cited on page 47.*
- [Groth and Northrup, 2005] C.P.T. Groth and S.A. Northrup, AIAA, (Jun. 2005), 2005-5333. *Cited on page 34.*
- [Hernández-Pérez et al., 2011] F.E. Hernández-Pérez, F.T.C. Yuen, C.P.T. Groth, and Ö.L. Gülder, Proc. Combust. Inst., 33 (2011) 1365-1371. *Cited on page 34.*
- [Haworth., 2010] D.C. Haworth, Prog. Energ Combust. Sci., 36 (2010) 168-259. *Cited on page 77.*
- [Ihme et al., 2005] M. Ihme, C. M. Cha, H. Pitsch, Proc Combust Inst 30 (2005) 793-800. *Cited on page 76.*
- [Ihme and See, 2010] M. Ihme, Y.C. See, Combust. Flame, 157 (2010) 1850-1862. *Cited on pages 77 and 79.*

- [Ihme and See, 2011] M. Ihme, Y.C. See, Proc. Combust. Inst. 33 (2011) 1309-17. *Cited on pages 30, 77, and 90.*
- [Joannon et al., 2007] M. de Joannon, A. Matarazzo, P. Sabia, A. Cavaliere, Proc. Combust. Inst., 31 (2007) 3409-3416. *Cited on pages 15 and 25.*
- [Joannon et al., 2009] M. de Joannon, P. Sabia, G. Sorrentino, A. Cavaliere, Proc. Combust. Inst., 32 (2009) 3147-3154. *Cited on pages 15 and 25.*
- [Joannon et al., 2012] M. de Joannon, G. Sorrentino, A. Cavaliere, Combust. Flame 159 (2012) 1832-1839. *Cited on pages 22 and 30.*
- [Konnov and Dyakov, 2009] A.A. Konnov, I.V. Dyakov, Proc. Combust. Inst., 32 (2009) 319-326. *Cited on page 14.*
- [Kim et al., 2005] S.H. Kim, K.Y. Huh, B.B. Dally, Proc. Combust. Inst., 30 (2005) 751-757. *Cited on pages 7 and 77.*
- [Lee and Choi, 2009] K.W. Lee, D.H. Choi, Int. J. Heat Mass Transfer 52 (2009) 1412-1420. *Cited on page 31.*
- [Liu et al., 2006] F. Liu, H. Guo, G.J. Smallwood, Combust. and Flame 144 (2006) 605-618. *Cited on page 45.*
- [Maas and Pope, 1992] U. Maas, S.B. Pope, Combust. Flame, 88 (1992) 239-264. *Cited on page 6.*
- [Mancini et al., 2003] M. Mancini, R. Weber, U. Bollettini, Proc. Combust. Inst. 29 (2003) 1155-1163. *Cited on page 31.*
- [Mastorakos, 2009] E. Mastorakos, Prog. Energy Combust. Sci. 35 (2009) 57-97. *Cited on pages 21, 26, 47, 52, 64, and 88.*
- [Mathur et al., 1967] S. Mathur, P.K. Tondon and S.C. Saxena, Molecular Physics, 12 (1967) 569-579. *Cited on page 34.*
- [McEnally et al., 2000] C.S. McEnally, L.D. Pfefferle, A.M. Schaffer, M.B. Long, R.K. Mohammed, M.D. Smooke, M.B. Colket, Proc. Combust. Inst. 28 (2000) 2063-2070. *Cited on page 30.*
- [Medwell et al., 2007] P.R. Medwell, P.A.M Kalt, B.B. Dally, Combust. Flame 148 (2007) 48-61. *Cited on pages 30 and 65.*
- [Medwell and Dally, 2012] P.R. Medwell, B.B. Dally, Combust. Flame 159 (2012) 3138-45. *Cited on pages 30 and 65.*
- [Moskaleva and Lin, 2000] L. V. Moskaleva, M.C. Lin, Proc. Combust. Inst. 28 (2000) 2393-2401. *Cited on page 34.*
- [Northrup and Groth, 2005] S.A. Northrup and C.P.T. Groth, AIAA, (Jan. 2005), 2005-0547. *Cited on page 34.*

- [Oldenhof et al., 2010] E. Oldenhof, M.J. Tummers, E.H. van Veen, D.J.E.M. Roekaerts, *Combust. Flame* 157 (2010) 1167-1178. *Cited on pages 11, 30, 76, 90, 91, 92, and 93.*
- [Parente et al., 2008] A. Parente, C. Galletti, L. Tognotti, *Int. J. Hydrogen Energy* 33 (2008) 7553-64. *Cited on pages 31 and 66.*
- [Peters, 1984] N. Peters, *Prog. Energy and Combust. Sci.*, 10 (1984) 319-339. *Cited on pages 11, 52, and 76.*
- [Peters, 2000] N. Peters, *Turbulent combustion*, Cambridge university press (2000). *Cited on pages 17 and 20.*
- [Pitsch et al., 1998] H. Pitsch, M. Chen, N. Peters, *Proc. Combust. Inst.* 27 (1998) 1057-64. *Cited on page 77.*
- [Pitsch, 2000] H. Pitsch, *Combust. Flame* 123 (2000) 358-374. *Cited on page 77.*
- [Pope, 1985] S.B. Pope, *Prog. Energy Combust. Sci.*, 19 (1985) 119-192. *Cited on page 77.*
- [Qin et al., 2000] Z.W. Qin, V.V. Lissianski, H.X. Yang, W.C. Gardiner, S.G. Davis, H. Wang, *Proc. Combust. Inst.* 28 (2000) 1663-1669. *Cited on page 53.*
- [Ramaekers et al., 2012] W.J.S. Ramaekers, J.A. van Oijen, L.P.H. de Goey, *Combust. Theor. Model.*, 16 (2012) 943-975. *Cited on page 89.*
- [Roe, 1981] P.L. Roe. *J. Comput. Phys.*, 43 (1981) 357-372. *Cited on page 34.*
- [Sabia et al., 2007] P. Sabia, M. de Joannon, S. Fierro, A. Tregrossi, A. Cavaliere, *Experimental Thermal and Fluid Science* 31 (2007) 46975. *Cited on page 31.*
- [Sepman et al., 2011] A.V. Sepman, A.V. Mokhov, H.B. Levinsky, *Int. J. Hydrogen Energy* 36 (2011) 4474-4481. *Cited on pages 34 and 53.*
- [Sepman et al.2, 2011] A.V. Sepman, A.V. Mokhov, H.B. Levinsky, *Int. J. Hydrogen Energy* 36 (2011) 13831-13837. *Cited on page 57.*
- [Sepman et al., 2013] A.V. Sepman, S.E. Abtahizadeh, A.V. Mokhov, J.A. van Oijen, H.B. Levinsky, L.P.H. de Goey, *Combust Flame*; 160 (2013) 1364-1372. *Cited on page 32.*
- [Sepman et al.2, 2013] A.V. Sepman, A.V. Mokhov, H.B. Levinsky, *Fuel* 103 (2013) 705-710. *Cited on pages 30, 31, 32, 35, 37, 49, and 66.*
- [Smith et al., 2000] G.P. Smith, D.M. Golden, M. Frenklach, N. W. Moriarty, B. Eiteneer, M. Goldenberg, C.T. Bowman, R.K. Hanson, S. Song, W.C. Gardiner, V.V. Lissianski, and Z. Qin, *GRI-Mech 3.0*, available at <[http://www.me.berkeley.edu/gri\\_mech/](http://www.me.berkeley.edu/gri_mech/)>. *Cited on pages 14, 31, 34, and 80.*



- [Smooke, 1991] M. D. Smooke, *Reduced Kinetic Mechanisms and Asymptotic Approximations for Methane-Air Flames*, Lecture Notes in Physics, Springer, Berlin, 1991, vol. 384. *Cited on page 89.*
- [Smooke et al., 1996] M.D. Smooke, A. Ern, M.A. Tanoff, B.A. Valdati, R.K. Mohammed, D.F. Marran, M.B. Long, *Proc. Combust. Inst.* 26 (1996) 2161-70. *Cited on pages 30, 45, 46, and 55.*
- [Somers, 1994] L.M.T. Somers, *The simulation of flat flames with detailed and reduced chemical models*, PhD thesis, Eindhoven University of Technology, Eindhoven, The Netherlands, 1994. *Cited on pages 13 and 80.*
- [Sorrentino et al., 2013] G. Sorrentino, D. Scarpa, A. Cavaliere, *Proc. Comb. Inst.* 34 (2013) 3239-3247. *Cited on pages 47 and 64.*
- [Soufiani and Taine, 1997] A. Soufiani and J. Taine, *Int. J. Heat Mass Trans.*, 40 (1997) 987-991. *Cited on page 35.*
- [Toro et al., 2005] V.V. Toro, A. Mokhov, H.B. Levinsky, M.D. Smooke, *Proc. Combust. Inst.* 30 (2005) 485-492. *Cited on pages 30, 45, and 46.*
- [Tsuji et al., 2003] H. Tsuji, A. Gupta, T. Hasegawa, M. Katsuki, K. Kishimoto, M. Morita, *High Temperature Air Combustion*, CRS Press, New York, (2003). *Cited on page 4.*
- [van Leer et al., 1989] B. van Leer, C.H. Tai and K.G. Powell, *AIAA* 89 (1989) 1933-CP. *Cited on page 35.*
- [van Oijen and de Goey, 2000] J.A. van Oijen, L.P.H. de Goey, *Combust. Sci. and Tech.*, 161 (2000) 113-137. *Cited on pages 6, 11, 52, and 76.*
- [van Oijen and de Goey, 2002] J.A. van Oijen, L.P.H. de Goey, *Combust. Theor. Model.*, 6 (2002) 463-478. *Cited on page 6.*
- [van Oijen and de Goey, 2004] J.A. van Oijen, L.P.H. de Goey, *Combust. Theor. Model.*, 8 (2004) 141-163. *Cited on page 6.*
- [van Oijen, 2013] J.A. van Oijen, *Proc. Combust. Inst.* 34 (2013) 1163-71. *Cited on pages 65, 76, and 82.*
- [Venkatakrishnan, 1993] V. Venkatakrishnan, *AIAA* (Jan. 1993) 93-0880. *Cited on page 34.*
- [Verissimo et al., 2011] A.S. Verissimo, A.M.A. Rocha, M. Costa, *Energy Fuels* 25 (2011) 2469-80. *Cited on page 31.*
- [Vreman et al., 2008] A.W. Vreman, B.A. Albrecht, J.A. Van Oijen, L.P.H. de Goey, R.J.M. Bastiaans, *Combust. Flame*, 153 (2008) 394-416. *Cited on pages 6, 77, 89, and 91.*
- [Vreman et al., 2009] A.W. Vreman, R.J.M. Bastiaans, B.J. Geurts, *Flow, Turb. Combust.* 82 (2009) 233-248. *Cited on page 89.*

- 
- [Weber et al., 1999] R. Weber, A.L. Verlaan, S. Orsino, N. Lallemand, J. Inst. Energy 72 (1999) 7783. *Cited on page 4.*
- [Weiss and Smith, 1995] J.M. Weiss, W.A. Smith, AIAA, 33(11) (1995) 2050-2057. *Cited on page 34.*
- [Wilke, 1950] C.R. Wilke, J. Chem. Phys. 18 (1950) 517-519. *Cited on page 34.*
- [Wünning and Wünning, 1997] J.A. Wunning, J.G. Wunning, Prog. Energy Combust. Sci. 23 (1997) 81-94. *Cited on pages 2, 3, 4, and 10.*
- [Zhu and Lin, 2005] R.S. Zhu, M.C. Lin, Int. J. Chem. Kinet. 37 (2005) 593-598. *Cited on page 34.*
- [Zhu and Lin, 2007] R.S. Zhu, M.C. Lin, J. Phys. Chem. A 111 (2007) 6766-6771. *Cited on page 34.*
- [Zhu et al., 2009] R.S. Zhu, H.M.T. Nguyen, M.C. Lin, J. Phys. Chem. A 113 (2009) 298-304. *Cited on page 34.*



# Acknowledgements

This project would have not been realized without the support of many people. The success of any project depends largely on encouragement and guidelines of many others.

Initially, my profound gratitude goes to my PhD supervisor, Jeroen van Oijen, whose supports and advices contributed significantly to the realization of my PhD research. Jeroen, during our regular meetings, you shared very valuable opinions and bright ideas. After each meeting, I felt motivated and inspired. I really enjoyed our nice discussions about physics of combustion. I will never forget your enthusiastic and friendly character.

I also take this opportunity to express my deep regards to my professor, Philip de Goey, who gave me a unique opportunity to boost my personal development and scientific experience. Philip, I highly appreciate your brilliant ideas about my topic during our monthly meetings. I also really enjoyed and learned your leadership skills over the combustion group in TU/e.

Rob Bastiaans, it is my pleasure to collaborate with you during my post-doctoral research. Marjan Dijk, thank you for your help in daily matters. Francisco, thanks for your indispensable help and support in my project. Alexey Sepman, I gratefully appreciate your considerable contribution to our project.

This research was supported by the Dutch Technology Foundation STW, which is part of the Netherlands Organization for Scientific Research (NWO) and partly funded by the Ministry of Economic Affairs (project number: 10414). I gratefully acknowledge STW. Specifically, I would like to thank Leo Korstanje for organizing our progress meetings in STW. I also want to thank the committee members of my PhD defense, prof. Cavaliere, prof. Levinsky, prof. Roekaerts, prof. Kuipers and prof. Geers. Thank you for your time, effort and feedback. I am especially grateful to prof. Cavaliere for his interest in my work and his helpful feedbacks to improve its quality.

I owe a large debt of gratitude to my parents, friends and colleagues who have enabled me to prosper. I would like to specifically mention Sudipto, Thiago, Nico, Atieh, Saeid Zandi, Amin, Reza, Saman, Ulas, Sridhar, Mayuri, Giel, Liselotte, Naseh, Alessio, Andrea, Maartin and Ugur for always been there at any hard time. I enjoyed every moment of working and hanging out with you.

My warmest and biggest thank goes to my beloved wife, Farimah Pouyandeh. Farimah, it is very hard to thank you in words. Although we had some tough times

during the writing of my PhD thesis due to the unlucky accident you had, those days fortunately seem to be over. Although I was tired and exhausted sometimes, you always made me smile and happy again. Thanks for all your nice emotions that make our life happy and hearty.

I seriously regret any unintentional omission in this acknowledgement.

January 2014

Ebrahim Abtahizadeh

# Curriculum Vitae

Ebrahim Abtahizadeh was born on 13 June 1982 in Tabriz, Iran.

- 2010 - 2014 PhD, Mechanical Engineering  
Eindhoven University of Technology, Eindhoven, the Netherlands  
Mechanical Engineering Department  
PhD Dissertation: *Numerical study of Mild combustion from laminar flames to Large Eddy Simulation of turbulent flames with Flamelet Generated Manifolds*
- 2004 - 2006 MSc, Mechanical Engineering (Energy Conversion)  
Amirkabir University of Technology, Tehran, Iran  
Mechanical Engineering Department  
MSc Thesis: *Development of reduced chemical mechanisms based on sensitivity analysis and QSSA approximation for CFD simulations of a lean premixed (LP) gas turbine combustor*
- 2000 - 2004 BSc, Mechanical Engineering (Thermal-Fluids)  
Tabriz University, Tabriz, Iran  
Mechanical Engineering Department  
BSc Project: *Study of different methods of designing Bi-Fuel (gasoline-CNG) internal combustion engines to avoid power loss during CNG operation*

## Publications from his PhD research

- [1] S.E. Abtahizadeh, J.A. van Oijen, L.P.H. de Goey, *Numerical study of Mild combustion with entrainment of burned gas into oxidizer and/or fuel streams*, Combustion and Flame 159 (2012) 2155-2165.
- [2] S.E. Abtahizadeh, A. Sepman, J.A. van Oijen, A. Mokhov, L.P.H. de Goey, H. Levinsky, *Numerical and experimental investigations on the influence of preheating and dilution on transition of laminar coflow diffusion flames to Mild combustion regime*, Combustion and Flame, 160 (2013) 2359-2374.

- [3] A. Sepman, S.E. Abtahizadeh, A. Mokhov, J.A. van Oijen, H. Levinsky, L.P.H. de Goey, *Numerical and experimental studies of the NO formation in laminar coflow diffusion flames on their transition to Mild combustion regime*, Combustion and Flame 160 (2013) 1364-1372.
- [4] A. Sepman, S.E. Abtahizadeh, A. Mokhov, J.A. van Oijen, H. Levinsky, L.P.H. de Goey, *Experimental and numerical studies of the effects of hydrogen addition on the structure of a laminar methane-nitrogen Jet in Hot Coflow under Mild Conditions*, International Journal of Hydrogen Energy, 38 (2013), 13802-13811.
- [5] S.E. Abtahizadeh, J.A. van Oijen, L.P.H. de Goey, *A novel flamelet-based reduced model to include preferential diffusion in autoigniting flames*, submitted to Proceedings of Combustion Institute (2013).
- [6] S.E. Abtahizadeh, J.A. van Oijen, L.P.H. de Goey, *Investigation of preferential diffusion effects in turbulent lifted CH<sub>4</sub>/H<sub>2</sub> flames using LES with a novel FGM-PDF model*, submitted to Proceedings of Combustion Institute (2013).

## Conference contributions

Only paper and oral contributions are listed.

- [1] S.E. Abtahizadeh, J.A. van Oijen, L.P.H. de Goey, *Investigation of preferential diffusion effects for LES of a hydrogen-enriched jet-in-hot coflow flame using the FGM tabulation technique*. 24th International Colloquium on the Dynamics of Explosions and Reactive Systems (ICDERS2013), 28 July - 2 August, 2013, Taipei, Taiwan.
- [2] S.E. Abtahizadeh, J.A. van Oijen, L.P.H. de Goey, *Numerical study of a jet-in-hot-coflow burner with hydrogen-addition using the Flamelet Generated Manifolds technique*. Bulletin of the 65th American Physical Society -Division of Fluid Dynamics (APS-DFD 2012), 18 - 20 November 2012, San Diego, CA, USA.
- [3] A. Sepman, S.E. Abtahizadeh, A. Mokhov, J.A. van Oijen, H. Levinsky, L.P.H. de Goey, *The effects of fuel and/or oxidizer composition on the structure of a laminar fuel jet in hot coflow under Mild conditions*, The 8th US National Combustion Meeting, 19-22 May, 2013, Salt Lake City, UT, USA.
- [4] S.E. Abtahizadeh, J.A. van Oijen, L.P.H. de Goey, *Numerical study of igniting counterflow diffusion flames with diluted and preheated air and/or fuel streams for Mild combustion*, Book of Abstracts of the 13th International Conference on Numerical Combustion (ICNC 2011), 27 - 29 April 2011, Corfu, Greece.
- [5] S.E. Abtahizadeh, J.A. van Oijen, L.P.H. de Goey, *Numerical investigation of main characteristics of Mild combustion flames with different diluted boundaries*, Proceedings of the 5th European Combustion Meeting (ECM 2011), 28 June - 1 July 2011, Cardiff, UK.